INFORMATION TO USERS

.

A

Multifractal

CO Study

of NGC 7129

Submitted in Partial Fulfillment of the Requirements for the degree of Master of Science May 1, 1998

...skolczi

The author has granted a non-exclusive licence allowing the National Library of Canada to reproduce, loan, distribute or sell copies of this thesis in microform, paper or electronic formats.

The author retains ownership of the copyright in this thesis. Neither the thesis nor substantial extracts from it may be printed or otherwise reproduced without the author's permission.

L'auteur a accordé une licence non exclusive permettant à la Bibliothèque nationale du Canada de reproduire, prêter, distribuer ou vendre des copies de cette thèse sous la forme de microfiche/film, de reproduction sur papier ou sur format électronique.
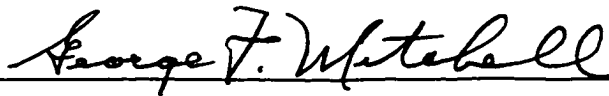
L'auteur conserve la propriété du droit d'auteur qui protège cette thèse. Ni la thèse ni des extraits substantiels de celle-ci ne doivent être imprimés ou autrement reproduits sans son autorisation.

0-612-33849-5
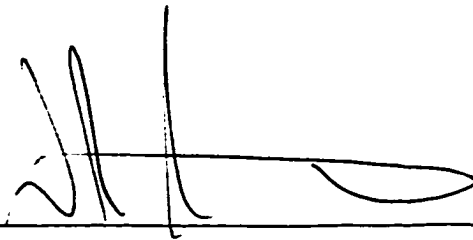
Canada

Certificate of Examination

Department of Astronomy and Physics
Saint Mary's University

Dr. George Mitchell (supervisor)
Professor of Astronomy and Physics
Saint Mary's University

Dr. David Guenther
Associate Professor of Astronomy and Physics
Saint Mary's University

Dr. David Clarke
Associate Professor of Astronomy and Physics
Saint Mary's University

TABLE OF CONTENTS

List of Figures

List of Tables

vi

ACKNOWLEDGEMENTS

A Multitransition CO Study of NGC 7129

Beverly Miskolczi
May 1, 1998

ABSTRACT

New observations of the molecular cloud NGC 7129, in several emission lines of CO, allows an assessment of the effects of recent and ongoing star formation. The CO data is supplemented with limited HCO^+ $J = 3 \rightarrow 2$ data. The cloud contains a very young star cluster with associated reflection nebulae, surrounded by a sharply-bounded molecular cavity. The CO maps, which are the first high resolution maps covering a significant portion of NGC 7129, reveal much new structure in the molecular ridge, such as gas clumps, and direct evidence for compression of the ridge by the young stars along the eastern border of the cavity. Evidence is presented that supports the idea that triggered star formation has taken place in NGC 7129, and suggests that it is likely to continue.

There is an energetic molecular outflow centred on or near the Be star $LkH\alpha$ 234, and a bipolar outflow to the south of this star which is associated with a far-infrared source. Additionally, there is high velocity blueshifted gas to the southwest of $LkH\alpha$ 234 and the molecular cavity. The new ^{12}CO $J = 3 \rightarrow 2$, ^{13}CO $J = 3 \rightarrow 2$, and ^{12}CO $J = 2 \rightarrow 1$ data permit a re-evaluation of the energetics and structure of the high velocity gas in the region. Optical depths, excitation temperatures, and column densities are calculated for each velocity channel at all positions in the redshifted outflow associated with $LkH\alpha$ 234. The column density channel maps show complex structure in the flow, including clumps and regions where the flow is interacting with ambient gas. An estimate of the energetics of the high velocity blueshifted gas is made for the first time. It is found that the blueshifted gas is the blue lobe of the outflow associated with $LkH\alpha$ 234, and consists of an extended molecular clump which has a swept back shape. The first high resolution maps of the FIRS bipolar outflow are presented, and show that the two lobes are similar in size and structure. An estimate is made of the energetics of the outflow.

1 INTRODUCTION

1.1 Star Formation and Young Stellar Objects

Star formation may take place by the contraction and collapse of a gas clump in the absence of external influence (spontaneous star formation (SSF)). Alternatively, star formation may take place due to an external, triggering event. Triggered star formation (TSF) is characterized by the induced formation of stars where they would otherwise be unlikely to occur such as in diffuse clouds (strong TSF), by the increase in the rate of star formation over the expected rate from SSF for a region (moderate TSF), or by the propagation of star formation through the bulk motion of the gas from one region to another with SSF rates of formation (weak TSF) (Elmegreen 1992). In general, the cause of triggered star formation is a high pressure event such as a supernova shock, an H II region, or a stellar wind (Elmegreen 1992). Regardless of the method of formation, with the onset of collapse the formation of a young stellar object (YSO) occurs. The YSO accretes matter through an accretion disk until the infall of matter is terminated, possibly through the formation of stellar winds (Shu *et al.* 1987). The YSO becomes fully convective and, on the HR-diagram, it descends on a convective pre-main sequence track. The YSO then develops a radiative interior and follows a radiative track down to the main sequence (Shu *et al.* 1987). It should be noted that in order to place a pre-main sequence object on the HR-diagram it must be optically visible (Bachiller 1996). With this in mind, the youngest objects on the HR-diagram are the T Tauri stars and their high-mass counterparts, the Herbig Ae/Be stars (Strom *et al.* 1975). Both T Tauri and Herbig Ae/Be stars are believed to already be on radiative tracks (Strom *et al.* 1975). A classification system for embedded YSOs has recently been developed (Lada 1991; Barsony 1995). One distinguishing property of the youngest class of YSO is a molecular outflow.

Spontaneous star formation occurs in cold clouds ($\approx$10-20 K) that are stabilized by magnetic fields, turbulence, or rotation (Shu *et al.* 1987). In this scenario the cold cloud begins with a low gravitational binding energy (Elmegreen 1992). Processes that reduce the energy of the system, such as ambipolar diffusion in the case of magnetic fields (Shu *et al.* 1987) or the dissipation of turbulence, increase the gravitational binding energy through the virial theorem until collapse occurs. It is possible, however, for a stabilized cold cloud to accrete matter and collapse because of the increase of mass without the loss of energy (Elmegreen 1992).

Three mechanisms for triggerin star formation have been identified (Elmegreen 1998). Star formation can occur through the compression of pre-existing globules or clumps in a cloud (1), through the accumulation of gas into a dense ridge or shell which then collapses gravitationally into dense cores (2), or through cloud collisions (3). The high pressures involved lead to an increase in density, at least on a small scale, which increases the local rate of energy dissipation and allows clumps (pre-existing or not) to become more gravitationally bound and hence, more likely to collapse (Elmegreen 1992). Star formation occurs on three scales based on the relative sizes of the triggered and triggering region: small, intermediate, and large (Elmegreen 1998). Small scale triggering involves mechanisms (1) and (2), and leads to the formation of individual, or binary stars. The triggering sources are young H II regions or stellar winds, and possibly supernova shocks. The Eagle Nebula (M16), made famous by the Hubble Space Telescope image, is an example of the triggering of pre-existing globules by a young H II region (Hester *et al.* 1996). The region about BD +40° 4124 is an example of TSF through the production of a cavity, observed as bright rims, by stellar winds (Hillenbrand *et al.* 1995). Intermediate scale triggering is through mechanism (2), and produces star clusters. The triggering sources are expanded H II regions, winds from OB associations, and supernova shocks. Examples of intermediate scale TSF are the Orion OB 1 association (Blaauw 1991), and the Cepheus OB 3 association (Sargent 1979). Large scale triggering occurs by methods (2) and (3), and produces star clusters and associations as well as new molecular clouds. The triggering sources are winds from old OB associations and supernova shocks. Examples include NGC 1333 (Warin *et al.* 1996) and Mon R2 (Xie & Goldsmith 1994).

A classification system for young stellar objects has been developed which is based on their infrared spectral energy distributions (SEDs). As the material around the YSO is dispersed, the SED evolves in a predictable manner (Lada 1991). The four classes of YSOs are defined by particular SEDs which are described in full in Bachiller (1996). The evolutionary phase of a YSO in a given class will be briefly described here. A Class 0 source is a YSO in its' main accretion phase and has an associated molecular outflow. A Class I source is in its' late accretion phase, but is still surrounded by a dusty envelope. Class II sources are optically visible, so they may be placed on the HR-diagram, and have an optically thick disk of material. T Tauri stars and their corresponding high-mass counterparts, Herbig Ae/Be stars, are believed to belong to this class. The last class, Class III, is composed of sources that are visible and have optically thin disks.

It is now accepted that every young stellar object passes through a period of mass loss in the form of a bipolar molecular outflow which is usually bipolar (Lada 1985; Bachiller 1996). As mentioned above, the sources of the outflows are most likely Class 0 YSOs. More than 160 molecular outflows have been discovered (Fukui *et al.* 1993; Bachiller 1996). Representative outflows are L1551 which is considered the prototypical outflow, HH 34 which is a low mass outflow, and Mon R2 which is a high mass outflow (Bachiller 1996). Sizes of outflows vary from less than 0.5 pc to 4-5 pc (Bachiller 1996). Outflows have kinetic energies that range from 10^{42} to 10^{47} ergs (Fukui *et al.* 1993).

A given outflow may contain five emission components: neutral atomic gas, ionized gas, high-excitation molecular H_2 gas, "standard high velocity" (SHV) dense molecular gas (ie. CO), and the "extremely high velocity" (EHV) dense molecular gas. A brief description is given here based on Bachiller (1996). The neutral atomic component may belong to the winds actually driving the molecular outflow but observations have yet to provide any detailed information on this gas component. The ionized gas is traced by Herbig-Haro (HH) jets and radio jets. The high-excitation molecular H_2 emission is due to shocks, and is detected primarily in HH objects (Lada 1985). The most massive component of an outflow is the SHV outflow since it consists of ambient material that is swept up by the underlying wind. "Standard velocities" for these outflows are considered to be less than 40 km s^{-1} with respect to the ambient

cloud velocity (Bachiller 1996). The temperatures and densities of molecular clouds are favourable for the excitation of the rotational transitions of molecules such as CO (Genzel 1991). Although the abundances of molecules such as CO are much lower than that of molecular hydrogen, the excitation conditions in molecular clouds make emission from molecules like CO an ideal method to probe molecular outflows. Recently, the "extremely high velocity" component of molecular outflows has been recognized, where "extremely high" refers to velocities greater than 40 km s^{-1} with respect to the ambient cloud velocity (Bachiller 1996). The EHV outflow is a highly collimated jet-like structure in the dense molecular component along the axis of the outflow, and is surrounded by the extended lobes of the SHV outflow. An example of an EHV outflow is NGC 2264G (Fich & Lada 1997).

1.2 Previous Observations of NGC 7129

NGC 7129 is a reflection nebula (Hubble 1922) with an associated cluster of stars (Pease 1917)

at a distance of 1 kpc (Racine 1968). The four brightest stars in the cluster are LkHα 234, BD +65 1638,

BD +65 1637, and SVS 13. Both LkHα 234 and BD +65 1637 are Herbig Be emission stars

(Herbig 1960). Strom et al. (1972) have shown that LkHα 234 is a B5-7e pre-main sequence star a

few x 10^5 years old and that BD +65 1637 is a B2-3e main sequence star. LkHα 234 has recently been

classified as a Class II young stellar object (Weintraub et al. 1994). Racine (1968) classified BD +65 1638

as a star of type B3. NGC 7129 has been imaged in the K' band (2.11 μm) by Hodapp (1994). This image

is shown in Figure 1 with the brightest stars labelled. Also shown in the figure are other astrophysical

objects of interest which will be discussed below. A comparison of this infrared image with an optical

image (see, for example, Mitchell & Matthews (1994)) shows that all objects seen in the optical are seen

in the infrared. A schematic of the region, including the new data presented in this thesis, is presented in

Figure 27.

Carbon monoxide (CO) observations have shown a number of interesting features in the molecular

gas associated with NGC 7129 (Loren et al. 1973; Loren 1977; Bechis et al. 1978; Edwards & Snell 1983;

Sandell & Liseau 1985; Bertout 1987; Mitchell & Matthews 1994). Early observations detected a

^{12}CO J = 1 → 0 emission peak associated with LkHα 234 (Loren et al. 1973; Loren 1977;

Bechis et al. 1978). A ^{13}CO J = 1 → 0 column density peak south of LkHα 234 was found to be coincident

with a newly detected 100 μm far-infrared source (FIRS) (Bechis et al. 1978). The only other far-infrared

source found in this region was LkHα 234. The observations of Bechis et al. (1978) provided the first

evidence of a molecular ridge to the immediate west of LkHα 234 and arcing along the eastern and

southern boundaries of the detected CO emission.
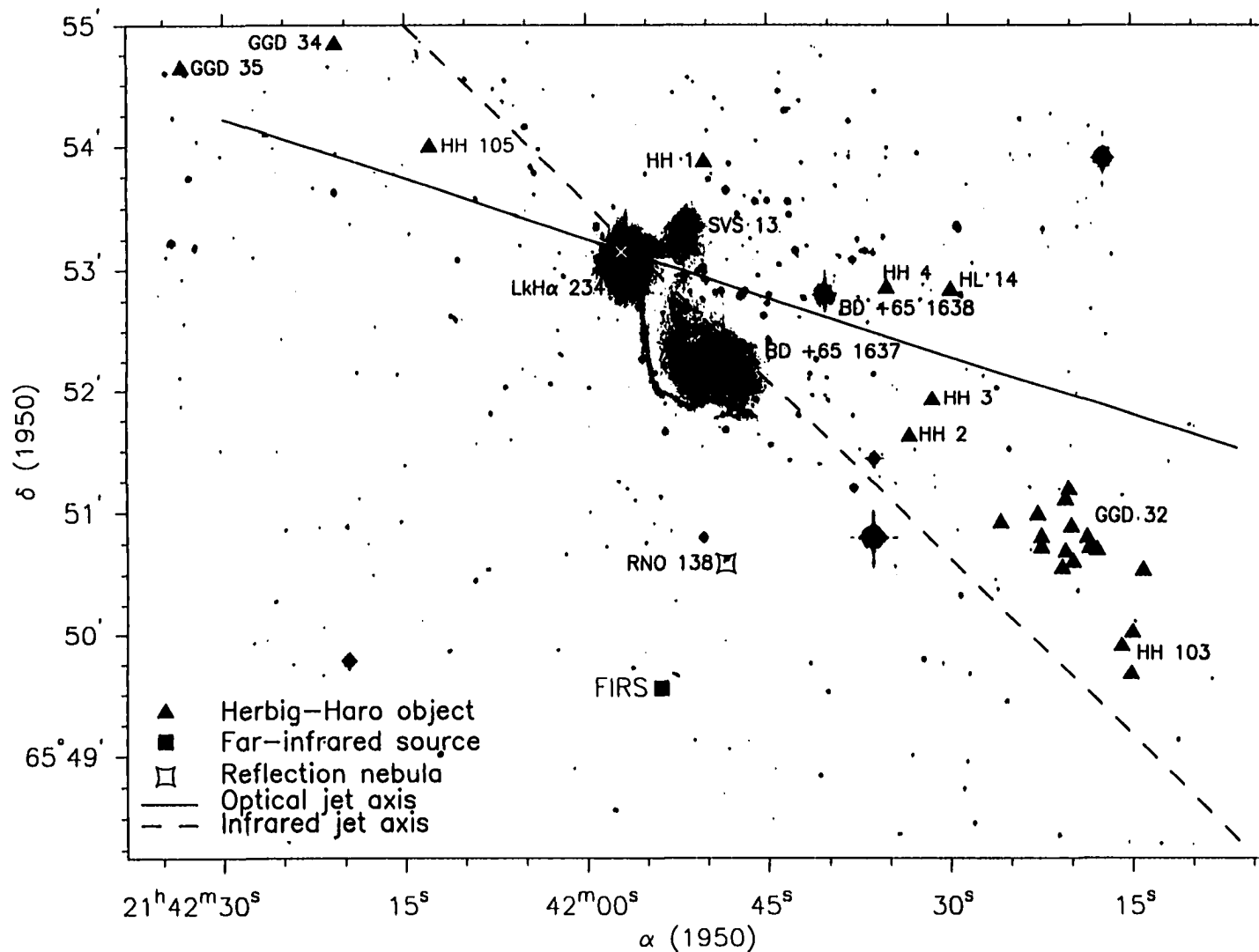
Figure 1. NGC 7129 Seen in the Infrared. The K' image is from Hodapp (1994). The four brightest stars in the cluster are labelled, and the optical position of LkHα 234 is marked by a cross. All other symbols are as indicated in the legend. The jets are observed to the southwest of LkHα 234. The greyscale was chosen to enhance the filamentary feature to the south of LkHα 234.

Later observations indicated the presence of redshifted molecular gas at positions about LkHα 234 and to the northeast (Edwards & Snell 1983; Sandell & Liseau 1985; Bertout 1987). A molecular cavity to the southwest of LkHα 234 and the molecular ridge was mapped by Bertout (1987). High velocity blueshifted gas was found to the southwest of the cavity and spatially coincident, in the sense of a projection, with the Herbig-Haro (HH) objects GGD 32 and HH 103 (Edwards & Snell 1983; Bertout 1987). A bipolar outflow associated with the FIRS was also detected (Edwards & Snell 1983; Sandell & Liseau 1985; Bertout 1987). The FIRS has tentatively been identified as an intermediate-mass Class 0 young stellar object, which is consistent with the presence of an outflow (Eiroa et al. 1998).

The most recent observations (at $15''$ resolution) by Mitchell & Matthews (1994) revealed details not previously seen. It was shown that there was a warm CO clump (T = 63 K) to the northeast of LkHα 234 (Peak 1) within the molecular ridge. The outflow was observed to be well collimated and a CO "hotspot" was found to be coincident with the position of the Herbig-Haro object HH 105. At the most highly redshifted velocities faint emission from the collimated outflow was still present, but the most intense emission was from a narrow jet-like structure within $\approx 20''$ of LkHα 234, an "inner jet", at a different position angle than the larger collimated outflow.

NGC 7129 has been observed in molecular transitions of molecules other than CO. Loren (1977) detected HCN, CS, SO, HCO$^+$, and H_2CO emission peaks associated with LkHα 234. The (1,1) transition of NH_3 has been observed to exist in two discrete cloudlets in the region (Torelles et al. 1983; Güsten & Marcaide 1986). There is a cloudlet associated with LkHα 234 and SVS 13 (peak emission to the north of both stars) which is in general coincident with the CO outflow (Güsten & Marcaide 1986). The gas traces the molecular ridge seen in CO, and follows the filament observed in the optical and infrared (see Figure 3 of Güsten & Marcaide (1986)). Güsten & Marcaide (1986) also detected an ammonia cloudlet associated with the FIRS. They did not detect any emission associated with GGD 32 and HH 103. Observations of LkHα 234 in CS J = 2 → 1 were made by Wilking et al. (1986). A CS cloudlet approximately $10'' \times 17''$ in size centred $4''$ east of LkHα 234 was discovered. The region has been mapped in the SO $J_N = 3_2 \rightarrow 2_1$ transition by Chernin et al. (1994). They found that the SO emission primarily

overlaps that of the ^{12}CO J = 1 → 0 emission mapped by Edwards & Snell (1983). No peak was coincident with LkHα 234, but a broad peak was detected to the northeast of the star oriented in a southeast/northwest direction and extending ≈3'. A SO peak was detected to the southwest of the FIRS at an offset of approximately (-0.5', -3.5') from LkHα 234.

A number of searches for HH objects in NGC 7129 have been conducted (the results have been shown in Figure 1). Spatially, the HH objects are divided into a group to the southwest of LkHα 234, and a group to the northeast. The brightest HH object is HH 103 (Strom *et al.* 1974; Cohen & Fuller 1985; Hartigan & Lada 1985), and is located to the southwest of LkHα 234. Proper motion studies indicate that HH 103 is moving in roughly a westerly direction (Ray *et al.* 1990). High resolution optical and Hα observations have found that HH 103 is composed of three patches of emission (Eiroa *et al.* 1992). Radial velocity studies of Hα emission (Strom *et al.* 1974; Magakian *et al.* 1994) indicate that the emission for all three features extends over the approximate velocity interval -160 to +30 km s^{-1} (V_{LSR} = -10 km s^{-1} for the ambient cloud), and that the southern and central patches are double-peaked whereas the northern patch is single-peaked.

Another southwestern HH object is GGD 32 (Gyulbudaghian *et al.* 1978; Cohen & Fuller 1985; Hartigan & Lada 1985). There is an arc of Hα emission which seems to link GGD 32 to HH 103 (Eiroa *et al.* 1992). Again, proper motion studies have shown that this object is moving in a westerly direction generally, although not all parts of GGD 32 seem to be moving in the same direction (Ray *et al.* 1990). Like HH 103, GGD 32 appears to be a complex rather than a single extended feature with at least 14 components (Eiroa *et al.* 1992). The proper motions referred to above seem to support this idea, as well as radial velocity data. Radial velocity measurements of Hα emission by Magakian *et al.* (1994) show that there may be two subgroups within GGD 32: one with lower velocity single-peaked (e.g. -35 km s^{-1}) emission, and the other with more highly blueshifted, double-peaked emission (e.g. peaks at -85 and -10 km s^{-1}). With only a few exceptions the Hα emission for all objects extends over a velocity range of -135 to +30 km s^{-1}.

Four other HH objects to the west of LkHα 234 have been discovered in NGC 7129 by Miranda *et al.* (1993). The first one, NGC 7129/HH 1, is one of only a few HH objects within the region of interest that is north of LkHα 234 and SVS 13. Two of the nebulosities, NGC 7129/HH 2 and NGC 7129/HH 3, lie to the southwest of LkHα 234 and BD +65 1637. NGC 7129/HH 4 is situated to the east of BD +65 1638. In the same survey another possible outflow, HL 14, was detected due east of BD +65 1638.

In a search for jet-like HH objects Ray *et al.* (1990) discovered an optical [SII] jet associated with LkHα 234 at a position angle of 252°. The jet, designated HH 167 (Shultz *et al.* 1995), contains eight emission knots extending =40″ from LkHα 234, and has a kink approximately at the mid-point. A spur-like feature at a position angle of =220° was also detected. Near-infrared imaging of molecular hydrogen and [FeII] emission (Shultz *et al.* 1995) confirms that the emission is due to shocks.

Aside from NGC 7129/HH 1 there are at least four other potential Herbig-Haro objects to the northeast of LkHα 234: GGD 33, GGD 34, GGD 35, and HH 105. GGD 33 was initially suspected of being an HH object by Gyulbudaghian *et al.* (1978). The observations of Hartigan & Lada (1985) indicated there are two components to the object, a and b, and that both are reflection nebulosities. It has been determined that GGD 33a is a T Tauri star with associated reflection nebulosity and GGD 33b is either a reflection nebulosity (Magakian & Movsesian 1997) or a possible outflow (Miranda *et al.* 1994a).

Hartigan & Lada (1985) determined that GGD 34 is an HH object. Later observations showed that GGD 34 is actually comprised of three emission patches (Gomez de Castro *et al.* 1993) where one of the patches is a jet (Ray 1987; Gomez de Castro *et al.* 1993). Each patch is blueshifted with average radial velocities of -180 km s^{-1}, -140 km s^{-1}, and -150 km s^{-1} (Magakian & Movsesian 1997), the last one being that of the jet.

GGD 35 was confirmed to be an HH object by Gyulbudaghian *et al.* (1978), Cohen & Fuller (1985), and Hartigan & Lada (1985). Radial velocity observations by Cohen & Fuller (1985) showed a single component at -162 km s^{-1}. The radial velocity observations by Magakian *et al.* (1994) revealed that

emission from the central and northwestern regions of the object is double-peaked, with peaks at -80 and -180 km s^{-1} and the eastern region had a single peak at -110 km s^{-1}.

Another object also found to be an HH object is HH 105 (Hartigan & Lada 1985). The optical nebulosity consists of two bright patches joined by an arc of emission (Ray 1987). No obvious exciting star was found (Hartigan & Lada 1985; Ray 1987). Magakian and Movsesian (1997) measured the radial velocity in [SII] of one patch to be -6 km s^{-1}, and that of the other to be -17 km s^{-1}. The radial velocities published by Mitchell & Matthews (1994) show that the most redshifted patch is coincident with the redshifted ^{12}CO J = 3 → 2 emission in the molecular outflow.

Early infrared studies at 2.2 μm of the NGC 7129 region (Strom et al. 1972; Cohen & Schwartz 1983) showed that all observed infrared sources were associated with optically visible stars. LkHα 234 was found to be an IRAS source (21418+6552) at all frequencies measured (Clark 1991). A re-analysis of the IRAS data has demonstrated that the cavity may be seen at 25 μm (Eiroa et al. 1998). An embedded population of stars near LkHα 234 was not discovered for over two decades after the initial studies of the region. To date, a total of eight deeply embedded infrared sources within 20″ of LkHα 234 have been observed (Weintraub et al. 1994; Weintraub et al. 1996). One source, PS 1, 3″ from LkHα 234 at a position angle of ≈310° was initially detected via polarization measurements alone (Weintraub et al. 1994) but was imaged at 10 μm by Cabrit et al. (1997) (referred to as IRS 6 in their paper). There appears to be a cometary nebula to the northwest of LkHα 234 visible in the N and L′ bands with PS 1 at the head of the nebula (Weintraub et al. 1996; Cabrit et al. 1997). The photometry by Cabrit et al. (1997) indicates that, at 17 μm, PS 1 is comparable in intensity to LkHα 234. At 2 μm, an arc of emission corresponding to the optical filament was detected by Cabrit et al. (1997). They also imaged a molecular hydrogen jet which is coincident with the inner portion of the optical jet, and detected substructure within the knots of the jet.

NGC 7129 has been surveyed for maser emission. Water maser emission, first detected by Schwartz & Buhl (1975), appeared to be associated with LkHα 234. Higher resolution observations found a total of four H$_2$O masers (Cesarsky et al. 1978; Sandell & Olofsson 1981; Tofani et al. 1995). The

position of one maser corresponds to that of LkHα 234, one is offset to the northeast of LkHα 234 at the approximate position of PS 1, one is offset to the southwest of LkHα 234, and one is associated with the FIRS (Cesarsky et al. 1978; Sandell & Olofsson 1981; Tofani et al. 1995). All four masers are highly variable in the number and intensity of emission peaks, and the velocities at which the peaks are detected (Schwartz & Buhl 1975; Cesarsky et al. 1978; Rodriguez et al. 1980; Sandell & Olofsson 1981; Wooterlout et al. 1988; Felli et al. 1992; Palla & Prusti 1993; Tofani et al. 1995). Neither OH nor SiO maser emission has been detected in NGC 7129 (Rodriguez et al. 1980).

Attempts have been made to detect x-ray emission from LkHα 234 and its surroundings. Due to the low resolution of the Einstein x-ray observatory, emission from LkHα 234 was not confidently detected, although x-rays from BD +65 1637 were detected (Damiani et al. 1994). X-ray emission associated with LkHα 234 was not observed by Zinnecker & Preibisch (1994) with ROSAT, but was at the position of BD +65 1637. Observations of NGC 7129 at radio frequencies have also been made (see Skinner et al. (1993) for a review of successful observations). A 3.6 cm continuum source was observed approximately 2″ from LkHα 234 along a position angle of 307° (Skinner et al. 1993). This is coincident with the 10 μm source detected by Cabrit et al. (1997) and with PS 1 (Weintraub et al. 1994).

As was stated above, NGC 7129 was initially classified as a reflection nebula. The four brightest stars each have reflection nebulosities associated with them, and there are numerous arcs of nebulosity to the south and west of LkHα 234 (Hartigan & Lada 1985; Eiroa et al. 1992). Reflection nebulosities were detected in association with HH 105, GGD 33, GGD 34, and GGD 32 (Hartigan & Lada 1985; Ray 1987; Eiroa et al. 1992). A separate reflection nebulosity, RNO 138, was found to the south of LkHα 234 (Cohen 1980; Hartigan & Lada 1985). This nebula has an S-shaped morphology and the illuminating star, RNO 138S, is a pre-main sequence star located at the centre of the nebulosity (Miranda et al. 1994b).

The idea that NGC 7129 may be a site of triggered star formation was first proposed by Bechis et al. (1978). Based on their CO observations and the fact that the values of reddening decreased from east to west (Strom et al. 1972; Racine 1968) across the region, they argued that there existed a low-density bubble on the near side of the nebula. They determined that the combined luminosity of LkHα 234,

BD +65 1637, and BD +65 1638 was sufficient to clear the bubble of gas via radiation pressure acting on grains. Alternatively they noted that BD +65 1638, the most evolved of the three stars, may have been luminous enough to have produced the initial cavity which then resulted in the formation of the molecular ridge and the two stars LkHα 234 and BD +65 1637. These two stars may then have aided in expanding the cavity. Bechis *et al.* (1978) proposed that the FIRS is also a result of triggered star formation. The molecular cavity discovered by Bertout (1987) is more evidence for a bubble. Additionally, the [SII] and Hα observations of Miranda *et al.* (1993) showed that the molecular cavity was completely surrounded by Herbig-Haro objects and reflection nebulosities, and that there was a hole in the middle of the nebulosity. A lack of 25 μm emission is also coincident with the position of the cavity (Eiroa *et al.* 1998). Bertout (1987) suggested that the cavity was formed from an expanding wind from LkHα 234 alone. The calculations by Bechis *et al.* (1978), and the detection of potential future sites of star formation in the molecular ridge by Mitchell & Matthews (1994) argue against that mechanism.

Originally the exciting source for the redshifted molecular outflow associated with LkHα 234 was thought to be LkHα 234 itself (Edwards & Snell 1983; Sandell & Liseau 1985; Bertout 1987). Ray *et al.* (1990) also proposed that the optical jet was driven by LkHα 234. The optical jet axis, however, fit the inner CO jet but not the larger collimated outflow (Mitchell & Matthews 1994). With the discovery of PS 1, Weintraub *et al.* (1994) have put forth the suggestion that this deeply embedded protostar may currently be driving the outflow. They do not rule out the possibility that LkHα 234 may have driven the outflow in the past, but they believe that it is too evolved at this time to drive an outflow.

The problem with PS 1 as the driving source of the outflow is the orientation of its polarization disk (Weintraub *et al.* 1994; Weintraub *et al.* 1996), and the observations by Cabrit *et al.* (1997). The projected polarization disk should be perpendicular to the outflow axis and parallel to the circumstellar disk. In the case of PS 1, however, the polarization disk is nearly parallel with the outflow axis (Weintraub *et al.* 1994; Weintraub *et al.* 1996). The observations by Cabrit *et al.* (1997) show that PS 1 (their 10 μm source) does not lie along the axis of the infrared jet they discovered. They propose that PS 1

may be the exciting source for the outer optical jet at a position angle of 252° (Ray *et al.* 1990), but that the infrared jet at 226° may be driven by an as yet undiscovered, more deeply embedded source.

Since the discovery of moving gas in NGC 7129, the question of the relationship between the redshifted molecular outflow, the blueshifted high velocity gas to the southwest, and the Herbig-Haro objects has been debated. One proposal places the blueshifted gas within the blue lobe of the FIRS with the FIRS as the driving source of both the moving gas and the HH objects GGD 32 and HH 103 (Edwards & Snell 1983; Magakian *et al.* 1994). Ray *et al.* (1990) included RNO 138 as a possible source for the two HH objects. Another interpretation is that the blueshifted gas is the counterpart to the redshifted outflow associated with LkHα 234 and is responsible, through interactions with the interstellar medium, for the HH objects (Sandell & Liseau 1985; Bertout 1987; Magakian & Movsesian 1997). It has also been proposed that HH 105 is the result of an interaction of the redshifted outflow with the interstellar medium (Mitchell & Matthews 1994; Magakian & Movsesian 1997). Radial velocity data indicates a relationship between the redshifted outflow and HH 105 as previously described. Other than the geometrical relationship between the outflow and the southern HH objects there is no evidence that the outflow associated with LkHα 234 is bipolar.

New observations of the outflows in NGC 7129 and the high velocity blueshifted gas in a number of molecular transitions are presented in this thesis. The observations will be discussed in §2. The features observed in the data at the ambient velocity, as well as those seen at higher velocities are presented in §3. The equations and procedures applied to the data for the calculation of kinematical quantities are presented in §4 and §5. The results of the kinematical calculations for the redshifted outflow associated with LkHα 234, the blueshifted gas near GGD 32/HH 103, and the FIRS bipolar outflow are given in §6. A comparison of these calculations to previously published results follows, along with a discussion of the possible relationship between the high velocity blueshifted gas near GGD 32/HH 103 and the redshifted outflow associated with LkHα 234.

2 OBSERVATIONS

All data dealt with in this paper were taken with the James Clerk Maxwell Telescope (JCMT) on Mauna Kea, Hawaii. The common user receivers RxA2 and RxB3i, along with the "Dutch" Autocorrelation Spectrometer (DAS) and the "Canadian" Acousto-Optical Spectrometer (AOSC), were utilized. See Tables 1 and 2 for the particular receiver/spectrometer combination used for a given observation, the velocity resolution obtained, and the grid spacings of all maps. The technique used to acquire the data, position switching or raster scanning, is given in these tables. With the position switching technique (PSSW) the off-source position is observed after each on-source integration in order to remove background sky noise. Raster scanning involves a single observation of the off-source position at the end of each scan line. The frequencies, the main beam efficiencies (η_{MB}) and the half-power beam widths (HPBW) of the transitions discussed in this paper are given in Table 3. Whenever possible the same velocity intervals were used to calculate the baseline for every spectrum in a given map or data set. For all spectra only linear baselines were removed using the SPECX function REMOVE-LINEAR-BASELINE (Padman 1992). The V_{LSR} of the NGC 7129 star-forming cloud is approximately -10.0 km s^{-1} and is hereafter referred to as the "quiescent" or "ambient" velocity. Similarly, the terms "blueshifted" and "redshifted" are with respect to the quiescent velocity. The region to the south and southwest of LkHα 234 will be referred to as the "southern region of NGC 7129" or "NGC 7129 south" following the notation of Hartigan & Lada (1985).

With the exception of the ^{12}CO J = 3 $\rightarrow$ 2 map of NGC 7129 south which was made by G. Sandell alone, all observations were made by some combination of G. Mitchell, H. Matthews, G. Sandell, and B. Miskolczi. Unless otherwise specified, all offsets are given with respect to LkHα 234 (α(1950) = 21^h 41^m 57.08^s, δ(1950) = +65° 53′ 09″). The ^{12}CO J = 3 $\rightarrow$ 2 map of LkHα 234 and its immediate surroundings was previously published (Mitchell & Matthews 1994).

Table 1. Observation Dates for LkHα 234 Region. The detectors are also shown.

Transition	Date of Observation	Receiver/ Spectrometer	Technique	Velocity Resolution [km s^{-1}]	Grid Spacing
^{12}CO J = 3 → 2	June 1993	RxB3i/AOSC	PSSW	0.22	7.5" x 7.5"
^{13}CO J = 3 → 2	August 1994	RxB3i/AOSC	PSSW	0.28	7.5" x 7.5"
^{12}C^{18}O J = 3 → 2	June 1995	RxB3i/DAS	PSSW	0.10	---
HCO$^+$ J = 3 → 2	June 1995	RxA2/DAS	RASTER	0.10	7.5" x 7.5"
^{12}CO J = 2 → 1	November 1995	RxA2/DAS	PSSW	0.21	30" x 30"
H^{13}CO$^+$ J = 3 → 2	November 1995	RxA2/DAS	PSSW	0.10	---
H^{13}CO$^+$ J = 4 → 3	November 1995	RxB3i/DAS	PSSW	0.10	---

Table 2. Observation Dates for NGC 7129 South. The detectors used are included.

Transition	Date of Observation	Receiver/ Spectrometer	Technique	Velocity Resolution [km s^{-1}]	Grid Spacing
^{12}CO J = 2 → 1	June 1995	RxA2/DAS	PSSW	0.10	30" x 30"
^{12}CO J = 3 → 2	October 1996	RxB3i/DAS	RASTER	0.20	4" x 8"
^{13}CO J = 3 → 2	October 1996	RxB3i/DAS	PSSW	0.14	10" x 10"

Table 3. Transition Frequencies and Relevant Telescope Parameters.

Transition	Frequency [Ghz]	HPBW ["]	η_{MB}
^{12}CO J = 2 → 1	230.5	20	0.69
H^{13}CO$^+$ J = 3 → 2	260.6	20	0.69
HCO$^+$ J = 3 → 2	267.6	20	0.69
^{12}C^{18}O J = 3 → 2	329.3	15	0.58
^{13}CO J = 3 → 2	330.6	15	0.58
^{12}CO J = 3 → 2	345.8	15	0.53*
H^{13}CO$^+$ J = 4 → 3	347.0	15	0.58

*from Mitchell & Matthews (1994). All other values from Matthews (1994).

The ^{13}CO J = 3 → 2 map includes a region approximately 150″ x 80″ to the northeast of

LkHα 234, as well as a strip approximately 100″ wide running 150″ to the south of LkHα 234 along the

molecular ridge. The ^{12}CO J = 2 → 1 map of LkHα 234 encompasses a region approximately 240″ x 100″

in dimension. The composite HCO⁺ J = 3 → 2 map is a map of a 80″ x 60″ region centred on LkHα 234

and a 80″ x 60″ region centred on (70″, 30″) in the outflow. Two spectra of the transition ^{12}C^{18}O J = 3 → 2

were taken at the positions (0″, 0″) and (52.5, 37.5). A ^{12}CO J = 2 → 1 map of the southern region of

NGC 7129 is approximately 400″ x 300″ in size. Due to emission in the off-source position used to

measure the sky background 98 of 167 spectra were contaminated at the line centre. An example of a

contaminated spectrum is shown in Figure 2. The contamination occurs in the approximate velocity range

of -12 km s⁻¹ to -6 km s⁻¹. Since the map was composed of a number of individual raster scans the

contamination was limited primarily to spectra west of LkHα 234. The ^{12}CO J = 3 → 2 map of NGC 7129

south encompasses a region approximately 450″ x 200″ in size. This particular map is unusual in that the

grid spacing, as shown in Table 2, is 4″ x 8″. The map includes the region about the FIRS bipolar outflow,

and curves northwest around the western edge of the molecular cavity to include the region containing

GGD 32 and HH 103. Limited observations of the ^{13}CO J = 3 → 2 transition were made, consisting of 18

points of observation near GGD 32/HH 103 and 16 points of observation in the red lobe of the FIRS bipolar

outflow.
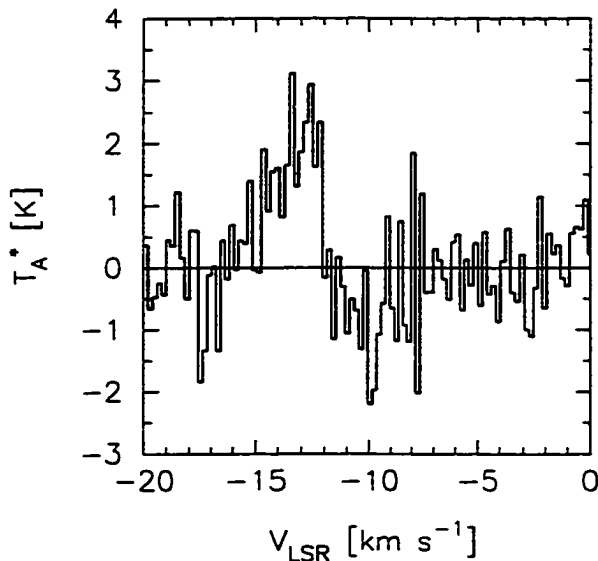
Figure 2. A Sample Contaminated ^{12}CO J = 2 → 1 Spectrum from NGC 7129 South. The contamination is limited to the velocity range -12 to -6 km s⁻¹.

3 DISTRIBUTION OF MOLECULAR GAS

In this section, the distribution of gas observed in NGC 7129 is discussed. The spectra, channel maps, and intensity maps have been chosen to show representative features. Channel maps are a series of integrated intensity maps that show changes in the distribution of gas with velocity. All integrated intensities refer to antenna temperatures. Antenna temperature is defined as the observed intensity corrected for antenna and telescope losses (Matthews 1994). All velocities are given with respect to the local standard of rest (-10 km s^{-1}). Every image is oriented with north to the top and east to the left. Offsets throughout this section are with respect to the position of LkHα 234 unless otherwise stated.

3.1 Gas Near the Quiescent Velocity

As noted in the Introduction, the dominant features in all CO transitions at velocities near the ambient velocity are the molecular ridge and cavity. The structure of the molecular ridge and the features seen within the ridge will be discussed in the context of CO integrated intensity maps and channel maps. A brief discussion of observations in other transitions is included.

A composite ^{12}CO J = 2 → 1 map of NGC 7129 is shown in Figure 3. The greyscale image is integrated intensity over the velocity range -11 to -9 km s^{-1}. The positions of the four brightest stars have been marked on the figure, as well as the brightest HH objects, the reflection nebula RNO 138 and the FIRS. The molecular ridge is the most prominent feature seen in the figure. A number of intensity peaks are visible within the ridge. Due to the sparse sampling the molecular ridge is quite broad, and both LkHα 234 and SVS 13 appear to be embedded within it. Little structure is seen in the gas to the northeast and south of LkHα 234 and the ridge . There is no intensity peak associated with the position of the FIRS.
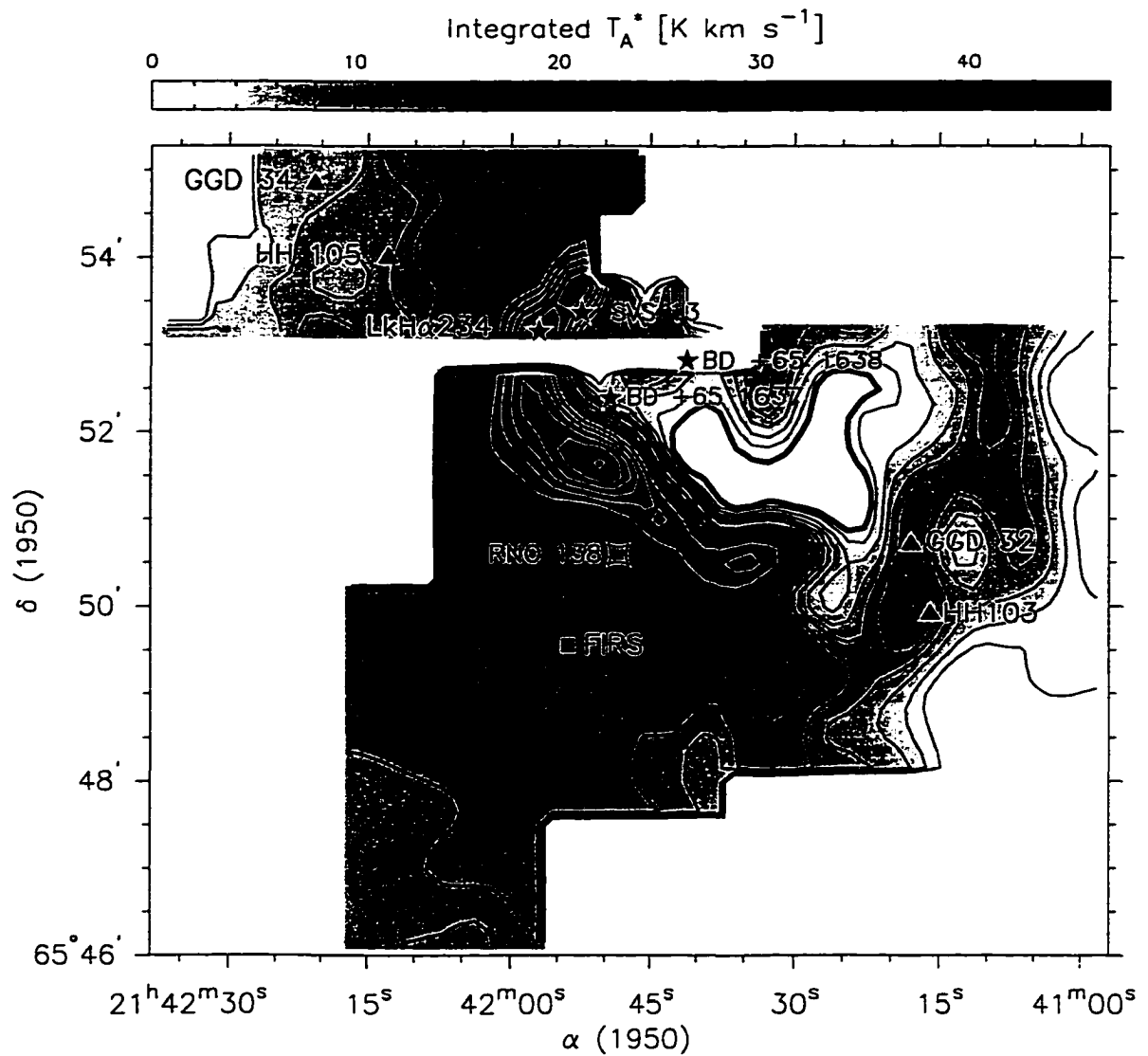
Figure 3. Ambient ^{12}CO J = 2 → 1 Gas in NGC 7129. The positions of the brightest stars are marked, as well as other objects of interest. The greyscale image is integrated intensity over the velocity range -11 to -9 km s^{-1}. The thick contour is the zero intensity contour, and represents the molecular cavity. The contours are: 2 to 10 K km s^{-1} in 2 K km s^{-1} intervals, and 10 to 46 K km s^{-1} in 4 K km s^{-1} intervals.

The molecular cavity to the southwest of LkHα 234 is indicated by the thick contour. Due to the contamination of the line centres mentioned in §2, the position of the zero contour as marked on the figure is not reliable. Comparison of the $^{12}CO = 2 \rightarrow 1$ data with observations such as Bertout (1987), however, indicate that the general position, the shape, and the angular extent of the cavity is in agreement with previously published data.

Channel maps of ^{13}CO J = 3 → 2 integrated intensity from the velocity range -12 to -7 km s^{-1} are given in Figure 4. The channel maps show that the molecular ridge is well defined in the narrow velocity range -11.0 to -9.5 km s^{-1}. The molecular cavity lies to the west of the ridge contours. Within this velocity range several intensity peaks are evident. The one at (-22.5″, 10″) corresponds to Peak 1 (Mitchell & Matthews 1994). Many of the intensity peaks are extended, the largest, which may be double peaked, is at (-45″, -90″). It has the approximate dimensions of 60″ x 30″ (0.28 x 0.14 pc at a distance of 1 kpc). A ^{12}CO J = 2 → 1 peak is coincident with this ^{13}CO peak. The differences between the ^{13}CO J = 3 → 2 and ^{12}CO J = 2 → 1 maps are due to the sampling of the maps and the beam sizes for each transition. As noted in the previous section the ^{13}CO J = 3 → 2 map is fully sampled with a HPBW of 15″, whereas the ^{12}CO J = 2 → 1 map is sparsely sampled (30″ x 30″) with a beam size of 20″. This also applies to comparisons of ^{12}CO J = 3 → 2 and J = 2 → 1 features. A ^{13}CO spectrum at the offset (-45″, -90″), along with H$^{13}CO^+$ J = 3 → 2 and J = 3 → 2 spectra, are presented in Figure 5. All three spectra are nearly Gaussian, with the ^{13}CO and H$^{13}CO^+$ J = 3 → 2 spectra having pronounced blue wings. Blueward of -12 km s^{-1} only emission from LkHα 234 is present and it extends out to a velocity of -13 km s^{-1}. Redward of -9 km s^{-1} there is no emission to the south of LkHα 234. The redshifted ^{13}CO emission to the northeast of LkHα 234 is the molecular outflow to be discussed in the next section, "High Velocity Gas".

Channel maps of ^{12}CO J = 3 → 2 to the south and west of LkHα 234 over the velocity range -14 to -6.5 km s^{-1} are shown in Figure 6. At -14 km s^{-1} the only features evident are the blue lobe of the FIRS bipolar outflow and the high velocity blueshifted gas near GGD 32/HH 103, both of which are discussed in detail in §3.2. At ≈-13 km s^{-1}, the FIRS appears to be embedded in a broad ridge-like structure. Redward of ≈-12 km s^{-1} the blueshifted gas near GGD 32/HH 103 seems to belong to the same
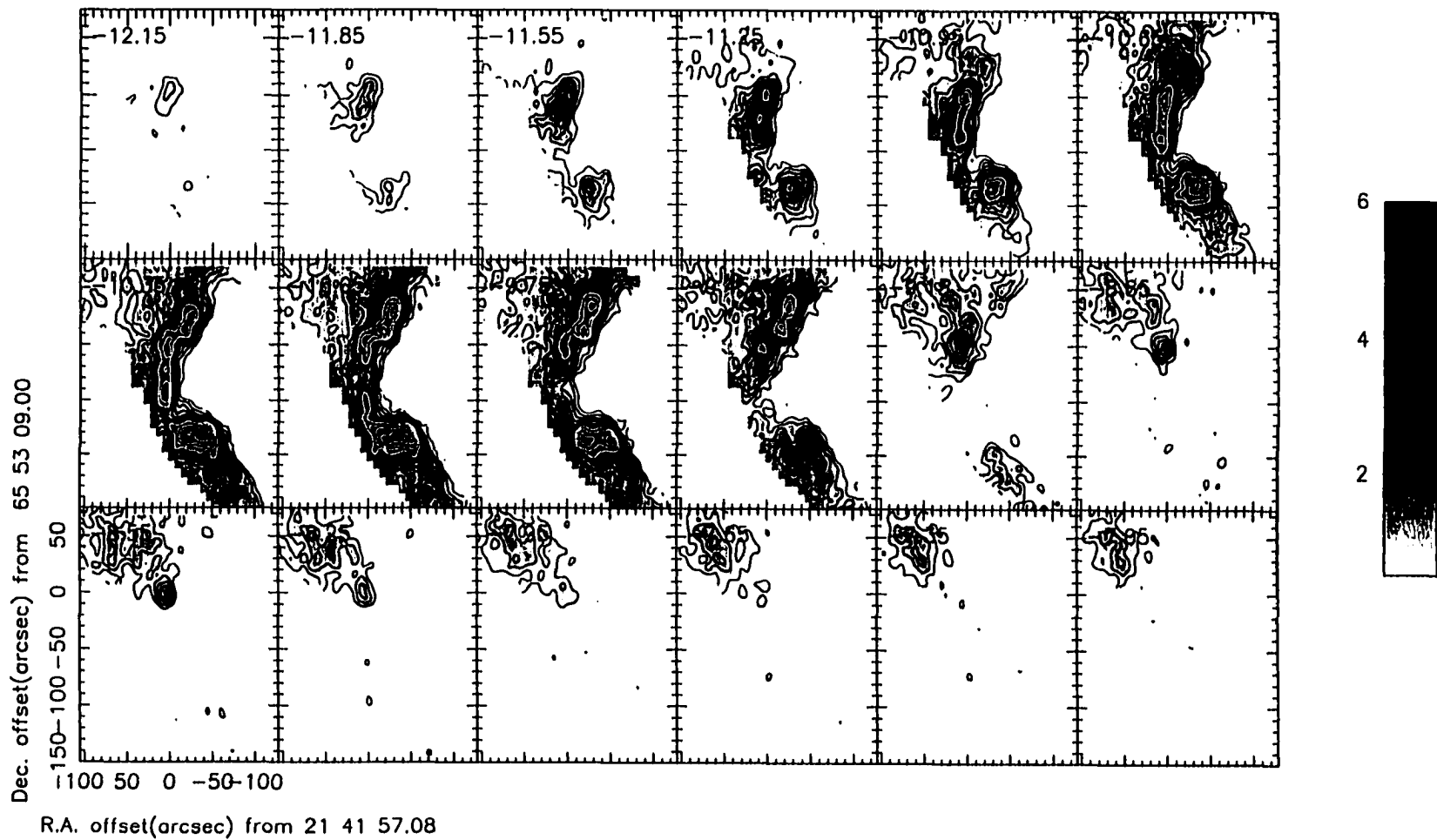
Figure 4. ^{13}CO J = 3 → 2 Channel Maps of LkHα 234 and the Molecular Ridge. The contour base level and intervals are 0.5 K km s^{-1}.
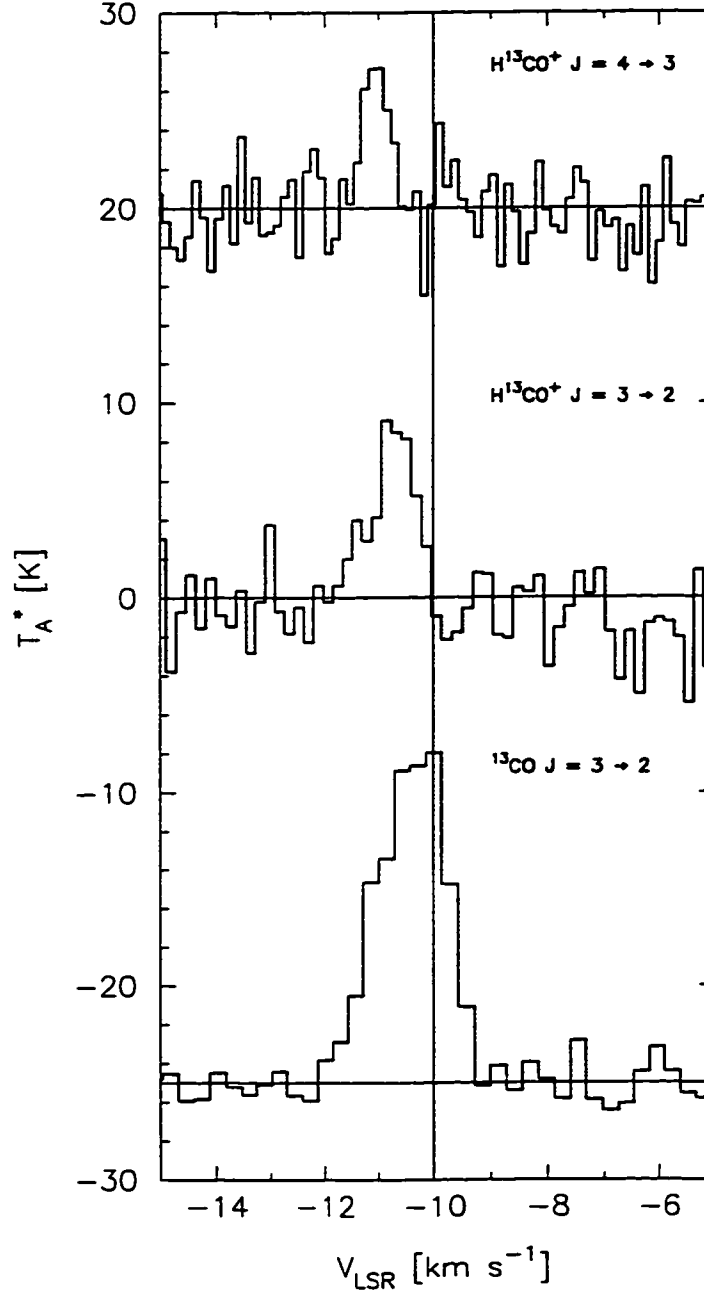
Figure 5. Spectra From the Peak in the Molecular Ridge at (-45″, -90″). The transitions are as indicated. Both the $H^{13}CO^+$ J = 3 → 2 and J = 4 → 3 spectra have been multiplied by a factor of 20 and twice binned.
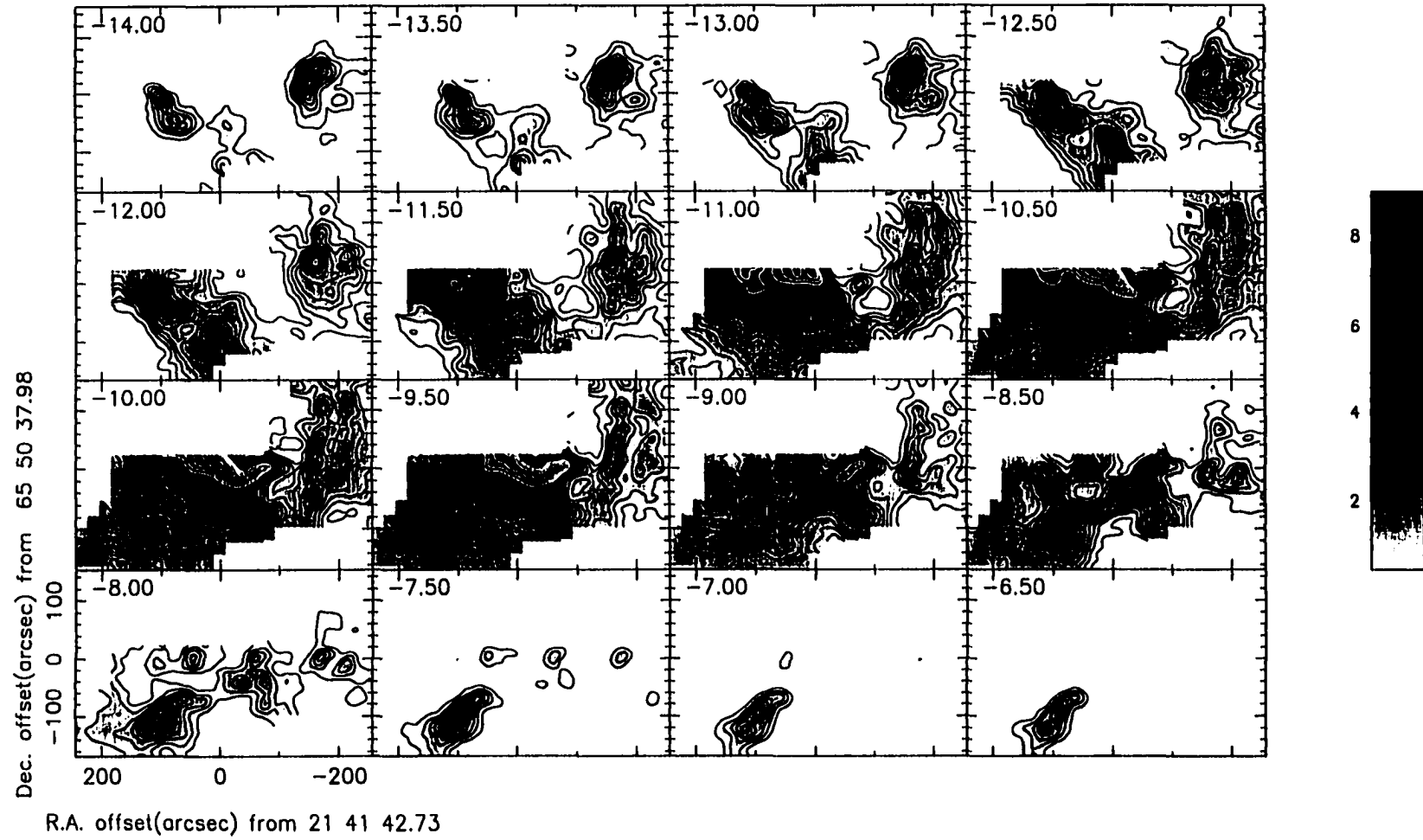
Figure 6. ^{12}CO J = 3 → 2 Channel Maps of NGC 7129 South. The contour base level and intervals are 0 and 0.5 K km s^{-1} respectively.

ridge feature. As the ambient velocity is approached from the blue, the eastern section of this ridge narrows and migrates northwest through the position of RNO 138 to the final position of the ridge at ambient velocities. The western section of the ridge remains at the same position for all velocities. A similar change in position of the ridge as the quiescent velocity is approached is seen in the ^{12}CO J = 2 → 1 data. A number of emission peaks can be found in the ridge near the quiescent velocity. Some of the peaks are contained within filamentary structures at the western edge of the map. These structures may also be seen in the ^{12}CO J = 2 → 1 data. The structures do appear to belong to the molecular ridge which is not as narrow as the ridge on the eastern border of the molecular cavity. As with the J = 2 → 1 data, there is no intensity peak associated with the position of the FIRS in the J = 3 → 2 transition.

It was noted earlier that there is a velocity interval in which elongated, filamentary structures exist in the ^{12}CO J = 3 → 2 data and J = 2 → 1 data. A ^{12}CO J = 3 → 2 map of the western segment of the molecular ridge, integrated over the velocity interval -11.25 to -8.5 km s^{-1}, is shown in Figure 7. Two distinct filaments can be seen, with several intensity peaks within them. None of the ambient gas J = 3 → 2 peaks are coincident with the positions of GGD 32 or HH 103. ^{12}CO J = 3 → 2 spectra at several positions in this interesting region are shown in Figure 8. The positions from which these spectra were observed are marked on Figure 7. As can be seen in the figure, the spectra were taken from both high and low intensity regions. Although there is a variety of line shapes, all spectra have a pronounced blue wing. Some of the wings extend out to ≈-20 km s^{-1}. The spectra from positions C, E and F, and possibly D, are double peaked with one peak at the ambient velocity and the second due to blueshifted high velocity gas. At C the most intense emission is blueshifted. The intensity of both peaks at positions D and E are approximately equal. The ambient peak is much more intense than the blueshifted peak at position F. As expected, the spectrum from position B has no intensity peak at ambient velocities, but does have a peak corresponding to moving gas. The spectra from positions C and D have an extended red wing, although not nearly as extended as the corresponding blue wings.
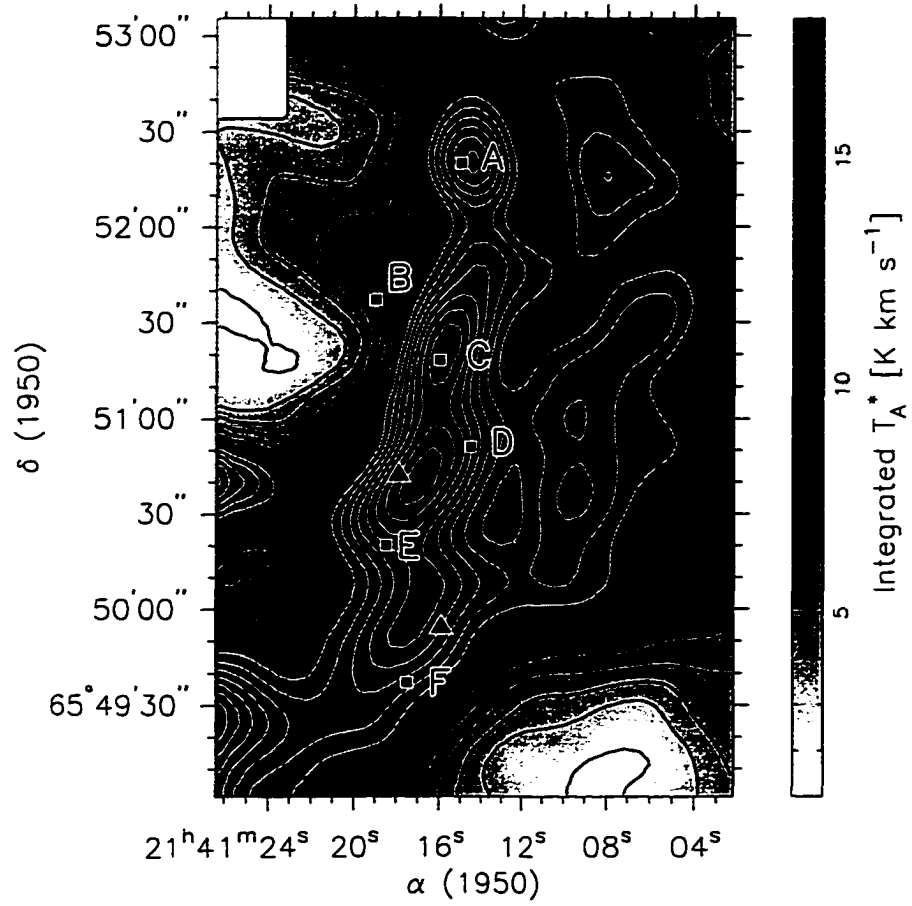
Figure 7. Filamentary Structures Near GGD 32/HH 103. The greyscale is ^{12}CO integrated intensity over the velocity range -11.25 to -8.5 km s^{-1}. The contour base level and interval are 1.0 K km s^{-1}. The squares with letters indicate the positions of the spectra to be shown in the next figure.
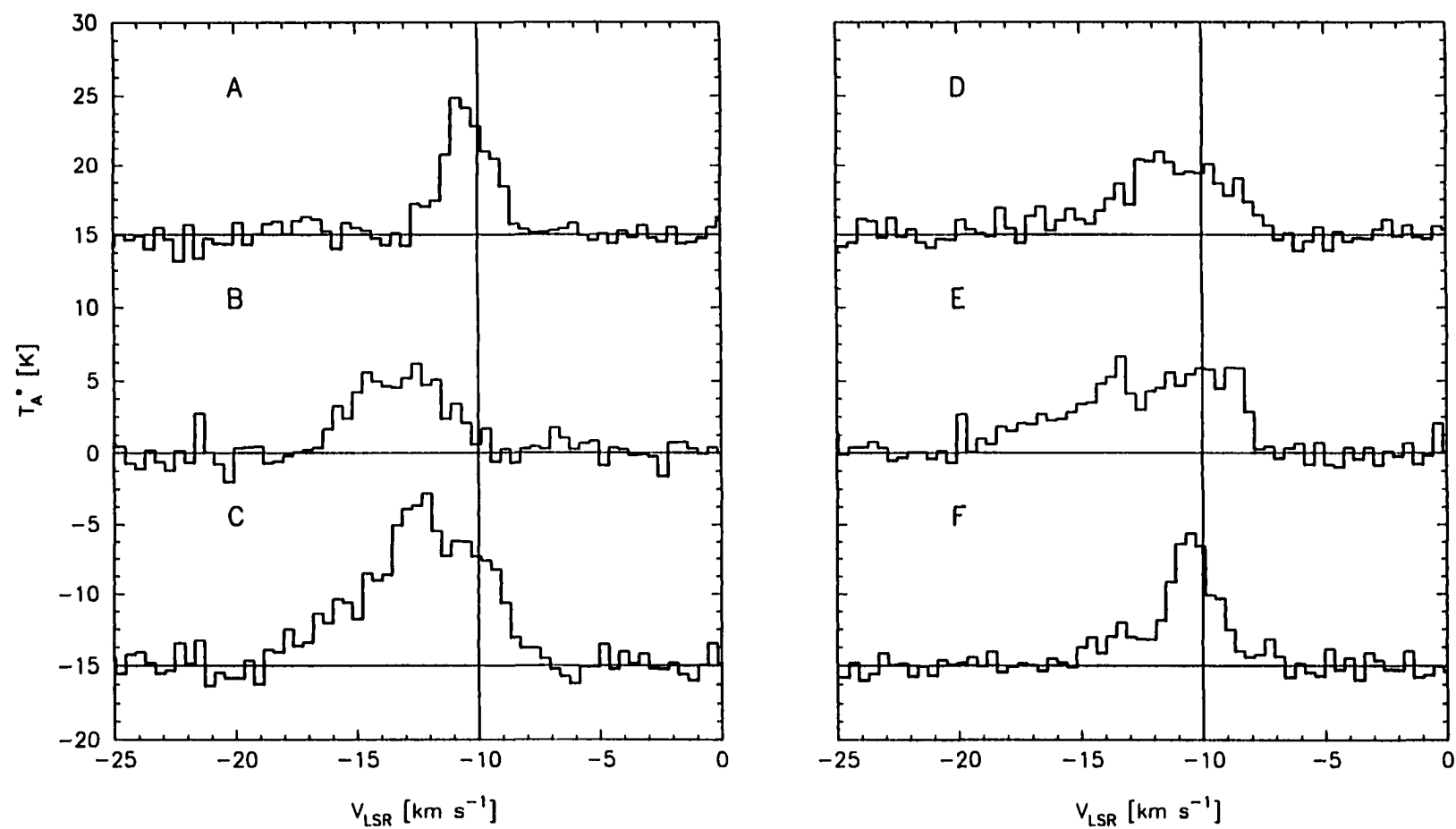
Figure 8. ^{12}CO J = 3 → 2 Spectra From the Region Containing the Filamentary Structures. The letters refer to the positions marked on Figure 7. With the exception of A, which may have a weak detached blue wing, all spectra have an extended blue wing.

In order to see more clearly the relationship between the molecular ridge and cavity at the ambient velocity, the integrated contours of both ^{13}CO and ^{12}CO J = 3 → 2 over the velocity interval -11 to -9 km s^{-1} are superimposed on the infrared image of Hodapp (1994) in Figure 9. The ^{12}CO contours are indicated by the thicker contours. The ^{13}CO emission drops off more sharply than the ^{12}CO since its abundance is much lower. Between the ^{12}CO and ^{13}CO contours all but the northern section of the molecular ridge is defined. It is evident from Figure 9 that the ^{13}CO molecular ridge south of LkHα 234 is coincident with the infrared emission filament (see Figure 1).

An integrated ^{13}CO antenna temperature map of the velocity interval -11 to -9 km s^{-1} is shown in Figure 10. The positions of the four brightest stars are indicated. The molecular ridge is the most prominent feature in this velocity range. Emission in three CO transitions at the offset (-30″, 30″) within the molecular ridge are shown in Figure 11. All spectra are Gaussian, or nearly Gaussian in shape, and are narrow, indicating that no high velocity moving gas is present at this location. There is no indication of self-absorption in any of the spectra. As with the CS emission peak (Wilking et al. 1986) the ^{13}CO intensity peak associated with LkHα 234 is offset ≈5″ east of the optical position of the star. It is not certain if LkHα 234 is embedded within the ridge. From the ^{13}CO contours it appears that that is the case. Recent interferometric observations of LkHα 234 in HCO$^+$ indicate, however, that the star may not be embedded within the ridge (Mitchell 1998). The broad emission peak at (-45″, -90″) [α(1950) = 21^h 41^m 49.9^s, δ(1950) = 65° 51′ 40″] is almost 40″ directly south of the star BD +65 1637. This star, which is the older of the two Be stars, is clearly not embedded within the molecular ridge. Bechis et al. (1978) found that the flux from BD +65 1637 was great enough to influence its' environment. This result is supported by the recent determination that emission from the IR filament is due to fluorescence rather than shocks (Noriega-Crespo et al. 1997).

SVS 13 appears to lie along the steep slope of the molecular ridge and not to be embedded within it. This is supported by the 2 μm image of Cabrit et al. (1997). In the 2 μm image SVS 13 lies to the west of an H$_2$ emission arc which may be centred on SVS 13 itself. The apex of the arc is marked on Figure 10 by a curly brace symbol and is ≈5″ east of SVS 13. Peak 1 lies ≈10″ due east of the star. SVS 13 may
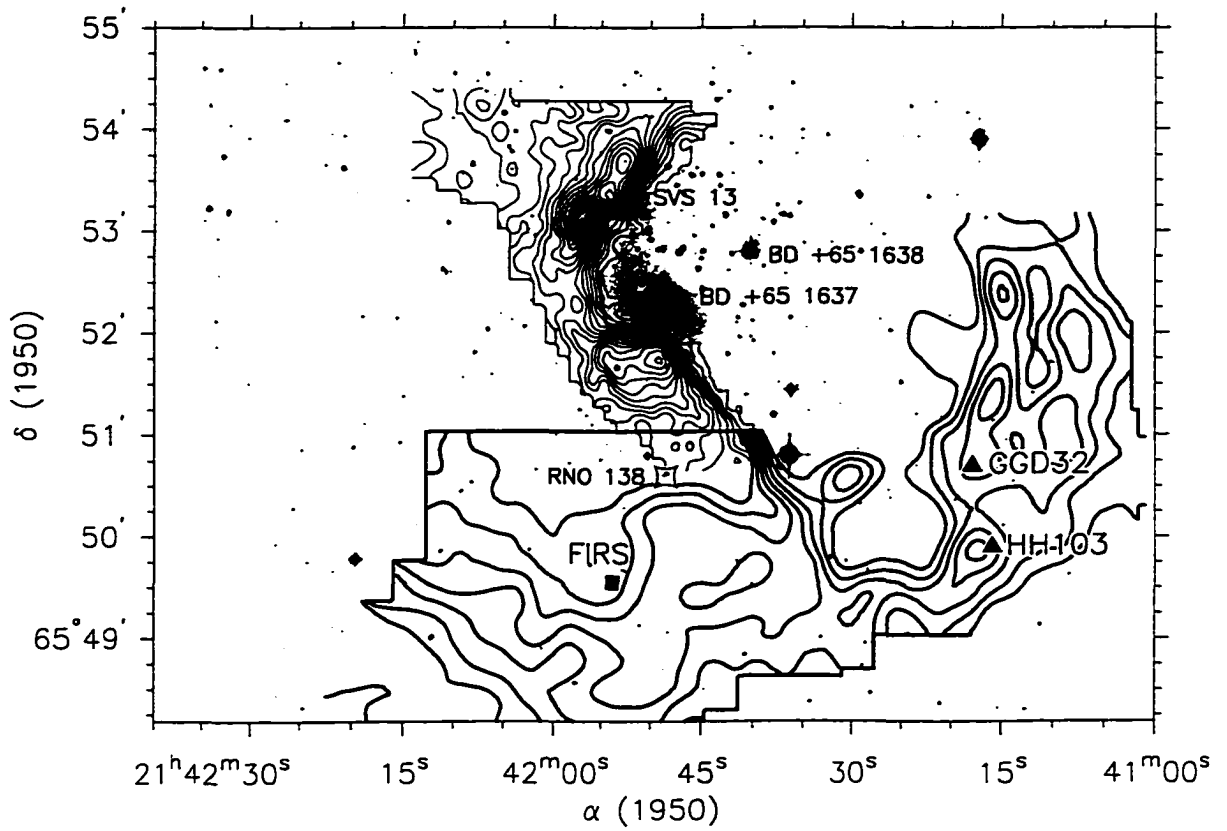
Figure 9. Ambient ^{13}CO and ^{12}CO J = 3 → 2 Gas in NGC 7129. The contours are superimposed on the K' image from Figure 1. The thin contours are of ^{13}CO, and have a base level and interval of 0.5 and 1.0 K km s^{-1} respectively. The brightest stars are labelled, with the exception of LkHα 234 which is indicated by a cross. The thick contours are of ^{12}CO, and have a base level of 1.5 K km s^{-1} and a contour interval of 0.5 K km s^{-1}.
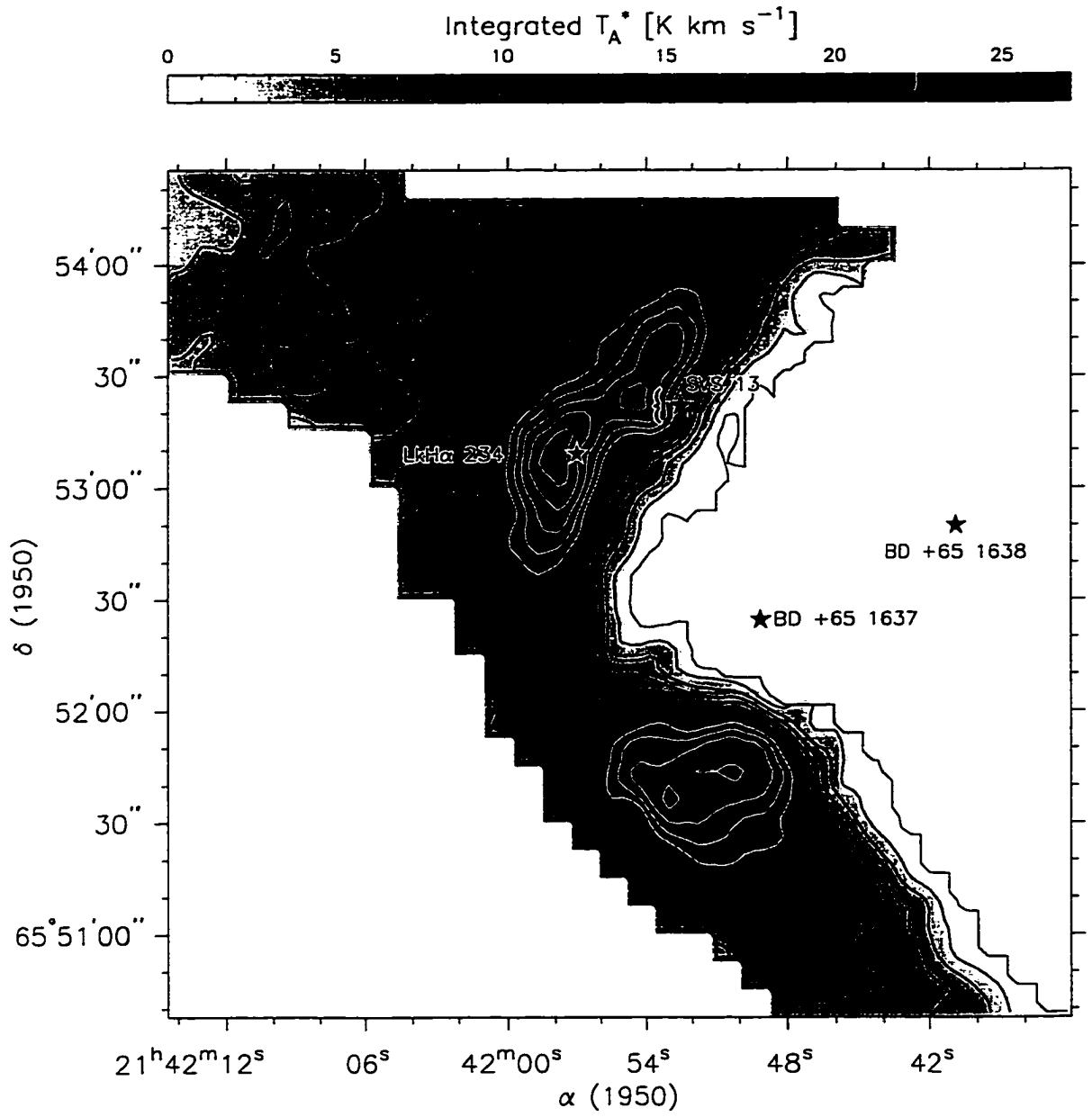
Figure 10. Ambient ^{13}CO J = 3 → 2 Gas Near LkHα 234. The positions of the brightest stars are marked. The curly brace marks the position of the apex of an H_2 emission arc which seems to be centred on SVS 13. The greyscale is integrated intensity over the velocity range -11 to -9 km s^{-1}. The contour base level is 0.0 K km s^{-1} and the contour interval is 2.0 K km s^{-1}.
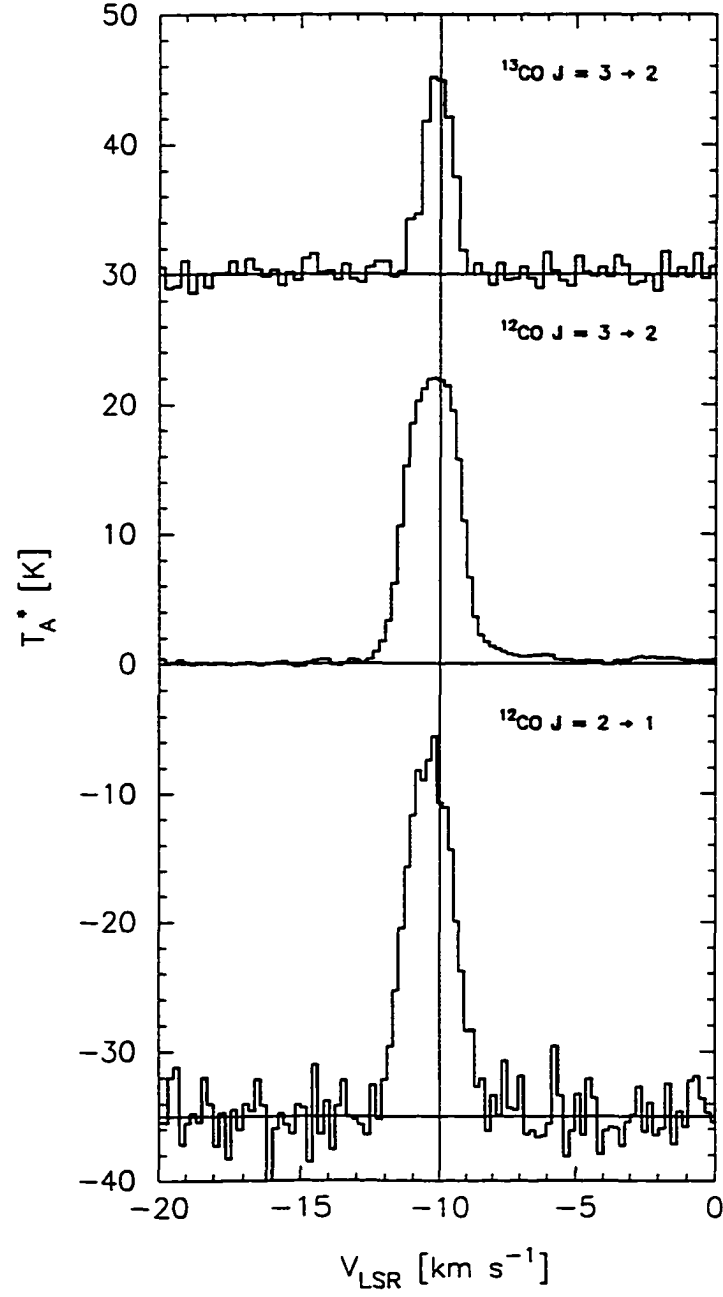
Figure 11. ^{12}CO and ^{13}CO Emission in the Molecular Ridge. The spectra are from the position (-30″, 30″) to the northwest of LkHα 234, and are representative, in shape, of the emission seen in the ridge. The transitions are as labelled in the figure.

be responsible for Peak 1. Since no spectral type is currently available for this star it is not known if its UV flux and/or stellar winds are capable of producing such compressive effects on the local environment. The idea that BD +65 1637 and SVS 13 are responsible for the nearby intensity peaks is consistent with the picture presented by Bechis *et al.* (1978), who argue that the younger stars are now the primary influence in the eastern region of NGC 7129.

An integrated intensity HCO^+ $J = 3 \rightarrow 2$ map about LkHα 234 and the molecular outflow in the velocity range -11 to -9 km s^{-1} is shown in Figure 12. Two intensity peaks are visible. One is coincident with LkHα 234, and the other is to the northeast with an emission peak at (45″, 55″) [α(1950) = 21^h 42^m 4.4^s, δ(1950) = 65° 54′ 4″]. The intensity peak associated with LkHα 234 is slightly offset to the northeast from (0″, 0″) [α(1950) = 21^h 41^m 57.08^s, δ(1950) = 65° 53′ 9″] and is present in the velocity range -12 to -7 km s^{-1}. Since HCO^+ is a dense gas tracer, the fact that this molecular ridge is narrower than that seen in the ^{13}CO transition is not unexpected.

One feature visible in the ^{12}CO $J = 3 \rightarrow 2$ data of Mitchell & Matthews (1994), but not mentioned there, appears at blueshifted velocities. Aside from the maximum intensity peak coincident with LkHα 234, a second peak at the position (45″, 55″) [α(1950) = 21^h 42^m 4.4^s, δ(1950) = 65° 54′ 4″] is present in the velocity range -15 to -12.5 km s^{-1}. As shown in Figure 13 there is a bridge of emission linking LkHα 234 and this secondary peak. Similar features are observed in the ^{12}CO $J = 2 \rightarrow 1$ transition. No corresponding blueshifted emission is observed in either ^{13}CO $J = 3 \rightarrow 2$ or HCO^+ $J = 3 \rightarrow 2$.

The spectra of the four transitions mentioned above and of $^{12}C^{18}O$ $J = 3 \rightarrow 2$ at the position of LkHα 234 are shown in Figure 14. The less abundant species have lines that are not as narrow as those given in Figure 11 from a position in the ridge. The ^{12}CO $J = 3 \rightarrow 2$ spectrum, and possibly the ^{13}CO spectrum, exhibits self-absorption at the line centre. Both the ^{12}CO $J = 2 \rightarrow 1$ and $J = 3 \rightarrow 2$ spectra have very extended wings in comparison to the other species indicating that there is high velocity gas at the position of LkHα 234. The ^{12}CO $J = 3 \rightarrow 2$ spectrum spans the interval from =-20 km s^{-1} to +12 km s^{-1}. Of all ^{12}CO $J = 3 \rightarrow 2$ spectra, the one from the position of LkHα 234 has the most extended wings.
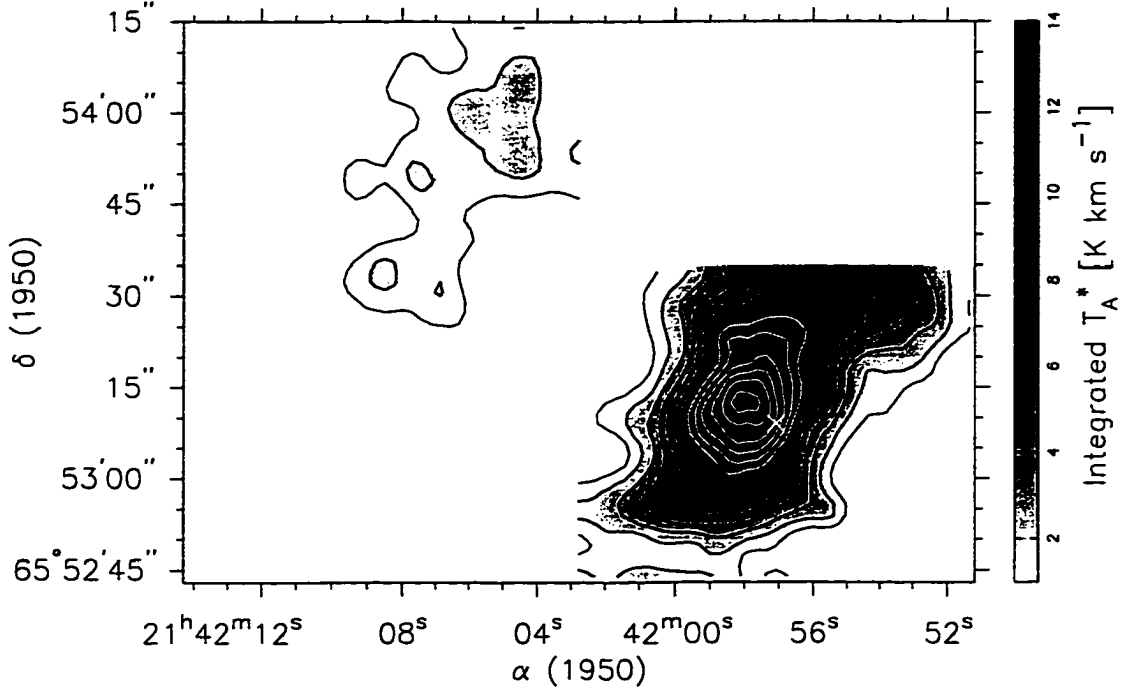
Figure 12. Ambient HCO⁺ J = 3 → 2 Gas Near LkHα 234. The position of LkHα 234 is marked by a cross. The greyscale is integrated intensity over the velocity range -11 to -9 km s⁻¹. The contour base level and intervals are each 1.0 K km s⁻¹.
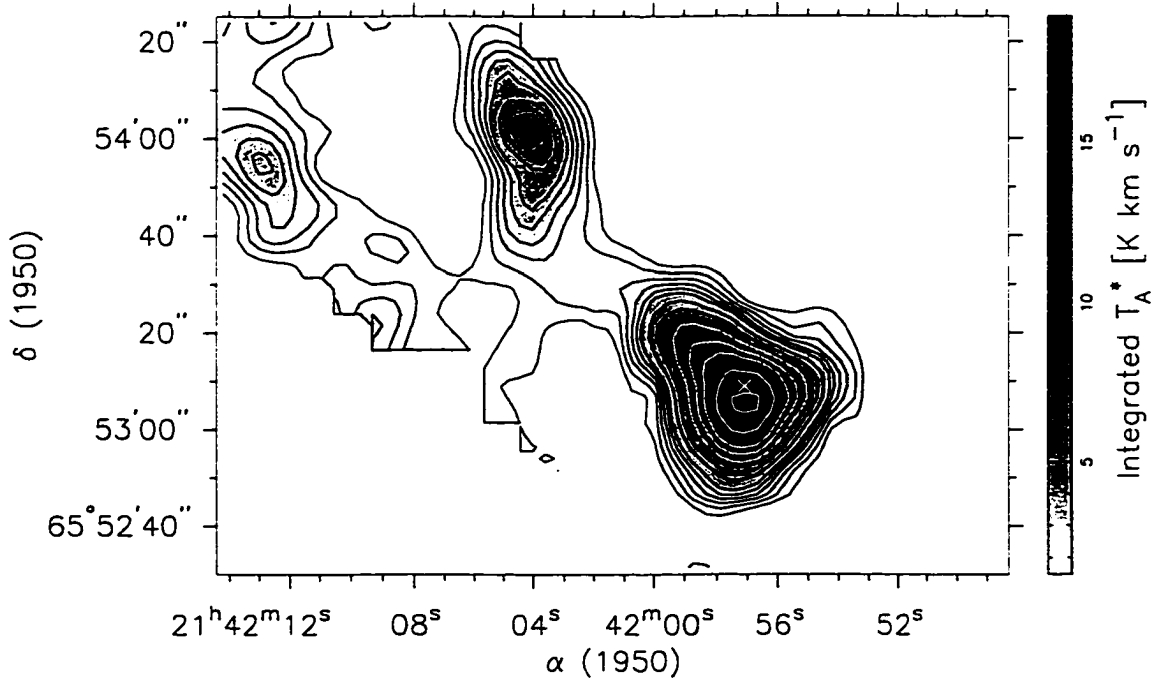
Figure 13. Blueshifted ¹²CO J = 3 → 2 Gas to the Northeast of LkHα 234. The position of LkHα 234 is indicated by a cross. The greyscale is integrated intensity over the velocity range -15 to -12.5 km s⁻¹. The contours are: 1.5 to 4.0 K km s⁻¹ in steps of 0.5 K km s⁻¹, 4 to 12.0 K km s⁻¹ is 2.0 K km s⁻¹ intervals, and 12 to 20.0 K km s⁻¹ in 4.0 K km s⁻¹ intervals.
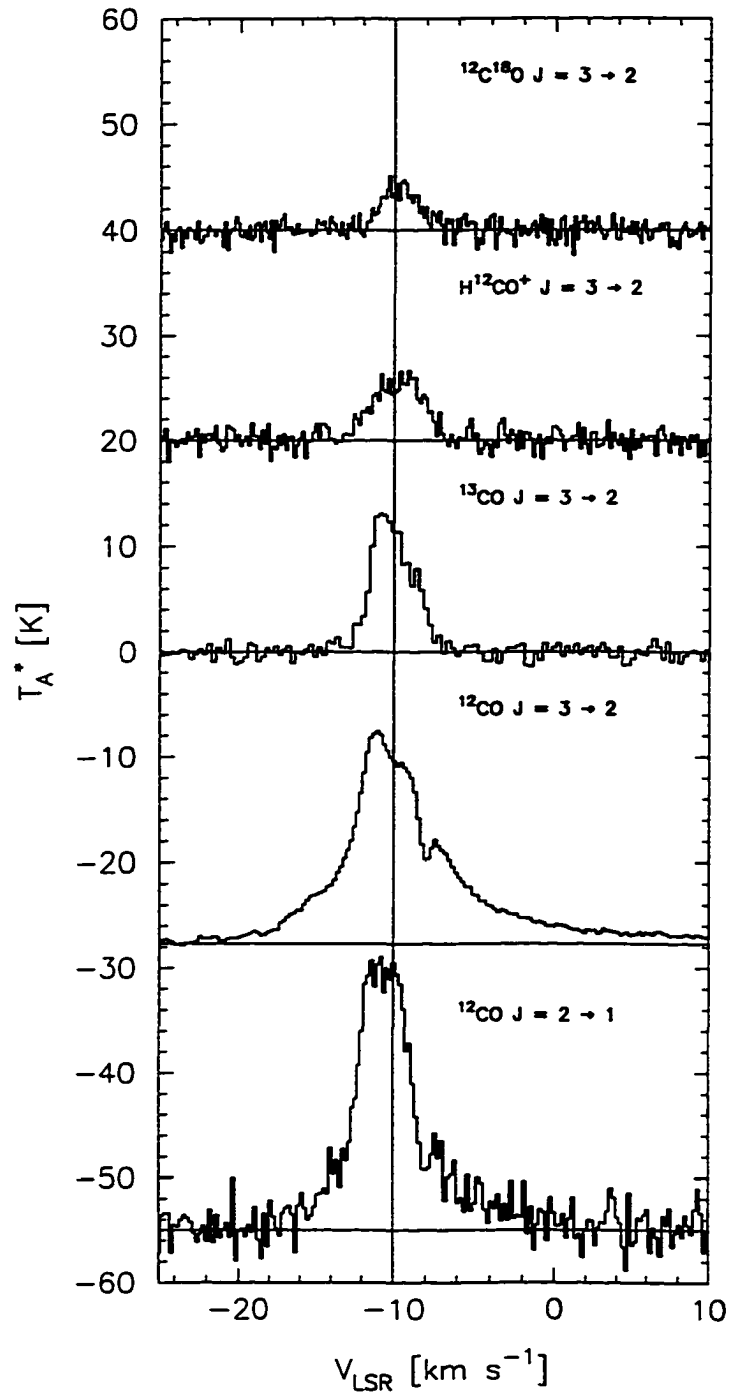
Figure 14. Spectra From the Position of LkHα 234. The transitions are as marked on the figure. The red wing of the ^{12}CO J = 3 → 2 spectrum extends to a velocity of +12 km s^{-1}.

3.2 High Velocity Gas

The structure of the moving gas is discussed in this section. Overviews of the two outflows in the region as well as the blueshifted gas near GGD 32/HH 103 in ^{12}CO J = 2 → 1 are given first. Following these will be the observations in ^{12}CO and ^{13}CO J = 3 → 2 and details of particular features. A discussion of the various spectral line shapes seen in the outflow associated with LkHα 234 is included.

^{12}CO J = 2 → 1 Emission:

Plots of the outflows as seen in the ^{12}CO J = 2 → 1 transition are shown in Figure 15 superimposed on the J = 2 → 1 greyscale ambient image from Figure 3. The contours for the redshifted outflow associated with LkHα 234 are the integrated intensity contours for the velocity range -8 to -7 km s^{-1}. The redshifted gas for the outflow as a whole extends to a velocity of ≈3.5 km s^{-1}, with the emission peak at (90″, 55″) [α(1950) = 21^h 42^m 10.1', δ(1950) = 65° 54′ 14″] persisting to a velocity of ≈1.5 km s^{-1}. The peak in the outflow is approximately coincident with the position of the ^{12}CO J = 3 → 2 emission peak and of HH 105. ^{12}CO J = 2 → 1 and J = 3 → 2, and ^{13}CO J = 3 → 2 spectra at the position of the ^{12}CO emission peak are shown in Figure 16. All three spectra exhibit a prominent semi-detached red wing. In the ^{12}CO spectra the emission at redshifted velocities is much stronger than the emission at quiescent velocities. In the ^{13}CO spectrum the emission at the ambient velocity is stronger than that at redshifted velocities.

Figure 15 also shows the high velocity blueshifted gas to the southwest of LkHα 234 which appears to be spatially associated with the Herbig-Haro objects GGD 32 and HH 103. The contours represent integrated intensity over the velocities -16 to -15 km s^{-1}. The blueshifted emission extends over the velocity interval ≈-17.5 to -11.5 km s^{-1}. Drawn on Figure 15 is the axis of the optical jet (solid line) at a position angle of 252° (Ray et al. 1990). For comparison, the axis of the 2.2 μm infrared jet (dashed line) discovered by Cabrit et al. (1997) at a position angle of 226° has been plotted as well. The redshifted
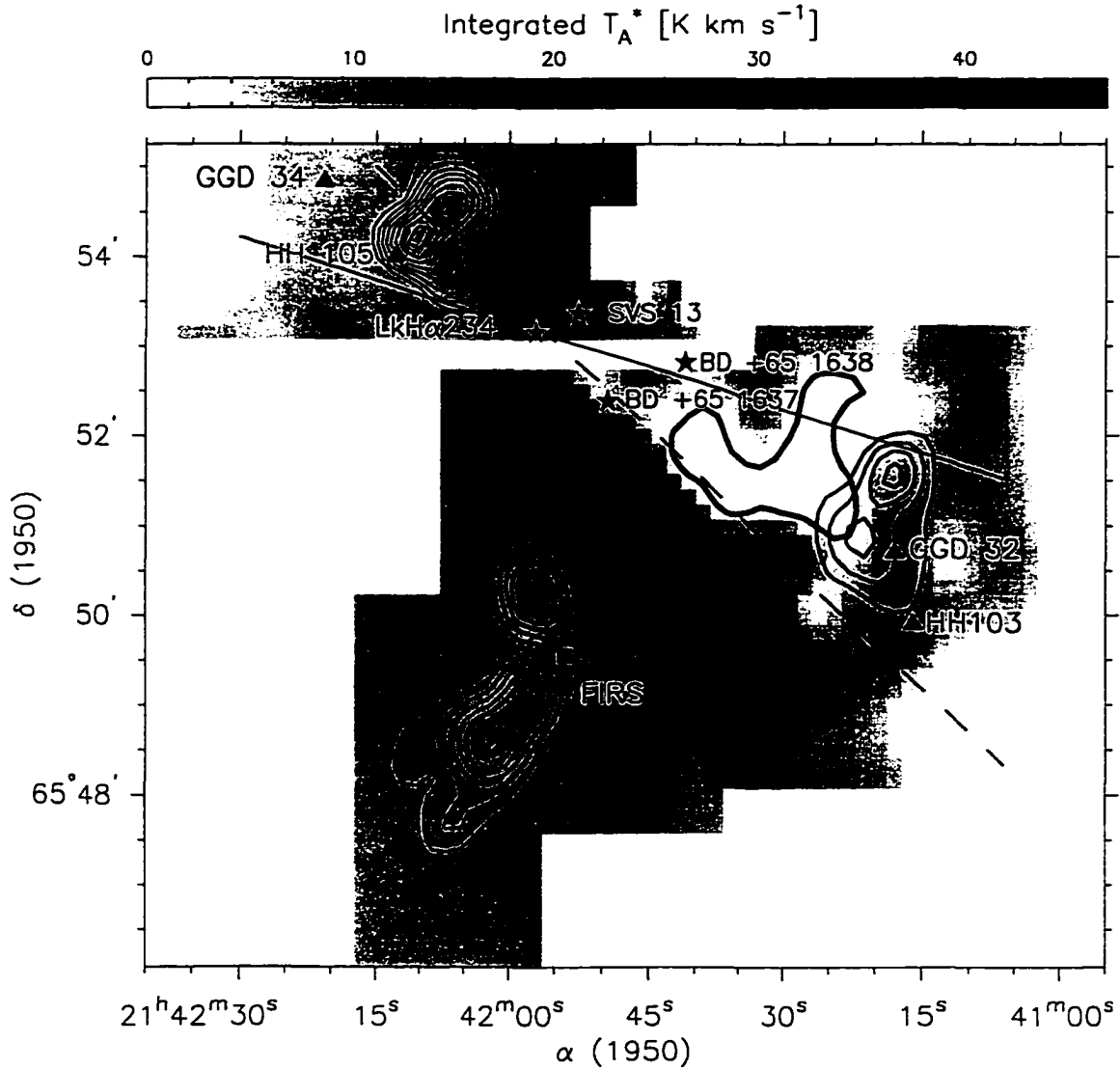
Figure 15. High Velocity ^{12}CO J = 2 → 1 Gas in NGC 7129. The positions of the brightest stars are marked, as well as other objects of interest. The greyscale is from Figure 3. Thin contours indicate redshifted gas, and thick represent blueshifted gas. The single, thick contour is the zero intensity contour. The blueshifted contours near GGD 32/HH 103 are for the velocity range -16 to -15 km s^{-1}. The contours for the blue lobe of the FIRS are over the velocity range -15 to -14 km s^{-1}. The contours of the red lobe of the FIRS are for the velocity interval -7 to -6 km s^{-1}. The contours for the redshifted outflow associated with LkHα 234 are over the velocity range -8 to -7 km s^{-1}. For the high velocity gas near GGD 32 and both lobes of the FIRS the contour base level and interval are each 1.0 K km s^{-1}. The base level and interval for the outflow associated with LkHα 234 are 3.0 and 1.0 K km s^{-1} respectively. The solid line represents the optical jet axis, and the dashed line represents the infrared jet axis.
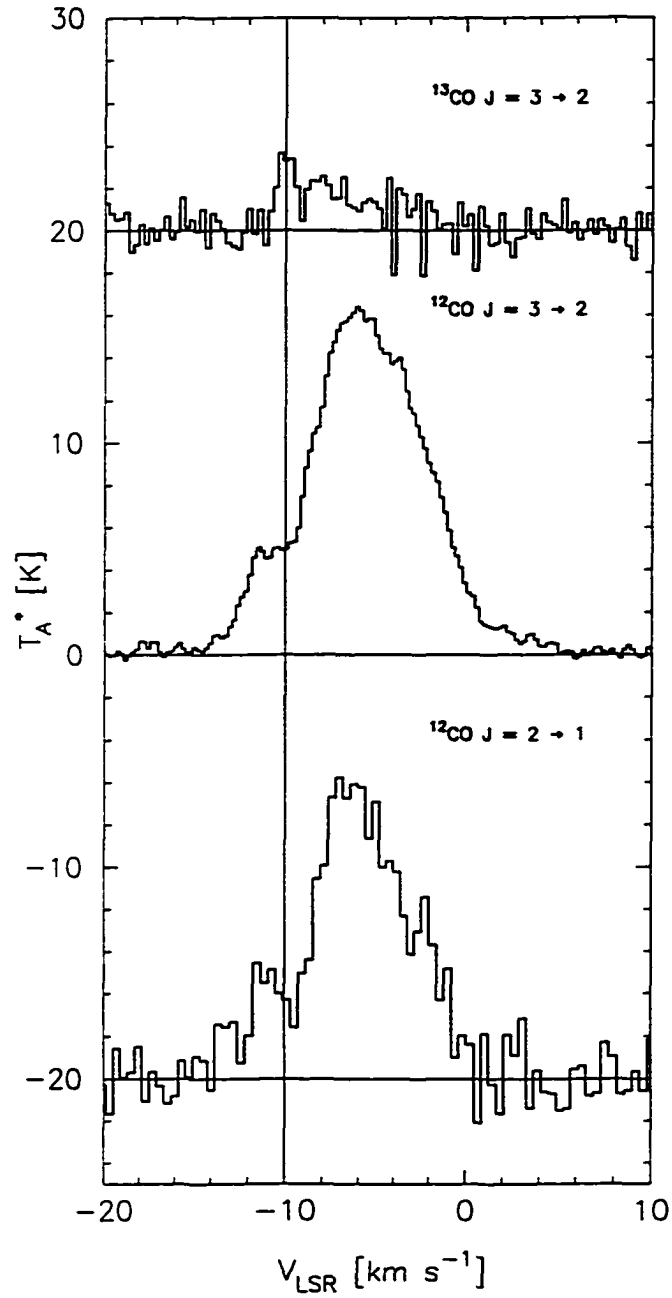
Figure 16. ^{13}CO and ^{12}CO Emission in the Outflow Associated with LkHα 234 at (90″, 52.5″). This position corresponds to the maximum ^{12}CO emission in the outflow.

molecular outflow associated with LkHα 234 is almost centred on the infrared jet axis, while the blueshifted gas is offset to the north of this axis. The optical jet axis delineates a southern boundary to the molecular outflow, and a northern boundary to the blueshifted gas.

The same figure shows the bipolar outflow from the FIRS to the south of LkHα 234. The integrated contours for the blueshifted and redshifted lobes are over the velocity ranges -15 to -14 km s^{-1} and -7 to -6 km s^{-1} respectively. The redshifted emission extends over the velocity range -8 to -3 km s^{-1}, and the blueshifted emission extends over the velocity interval -18 to -13 km s^{-1}. Each lobe has a single intensity peak: the red and blue lobe peaks are at (30″, -275″) [α(1950) = 21^h 42^m 1.1^s, δ(1950) = 65° 48′ 39″] and (0″, -175″) [α(1950) = 21^h 41^m 56.9^s, δ(1950) = 65° 50′ 16″] respectively.

Molecular J = 3 → 2 Emission:

The bipolar outflow and high velocity blueshifted gas in the ^{12}CO J = 3 → 2 transition are shown in Figure 17 along with the redshifted outflow associated with LkHα 234. This redshifted outflow is as shown in Mitchell & Matthews (1994). The high velocity blueshifted gas has the shape of a kidney. This may indicate the presence of a wind-cloud interaction due to a poorly collimated wind from the direction of LkHα 234 interacting with an isolated gas clump. Emission from the blueshifted gas extends over the velocity interval -18.5 to -12 km s^{-1}. The two HH objects in the region, GGD 32 and HH 103, consist of knots of shocked gas. Emission from both atomic and molecular hydrogen has been detected, as well as from atomic ions (see §1 for references). There is a large discrepancy in the widths of the Hα lines of the HH objects and those of the molecular component. The Hα lines have emission extending over a velocity range of ≈-150 to +30 km s^{-1}, whereas the CO emission is over the velocity range -20 km s^{-1} to 0 km s^{-1}. The CO lines are narrower by a factor of 9. If there were a single HH object, then this could be explained by a clump in the collimated wind interacting with ambient material. There is no explanation for the differing radial velocities of so many HH objects at this time (Magakian et al. 1994).
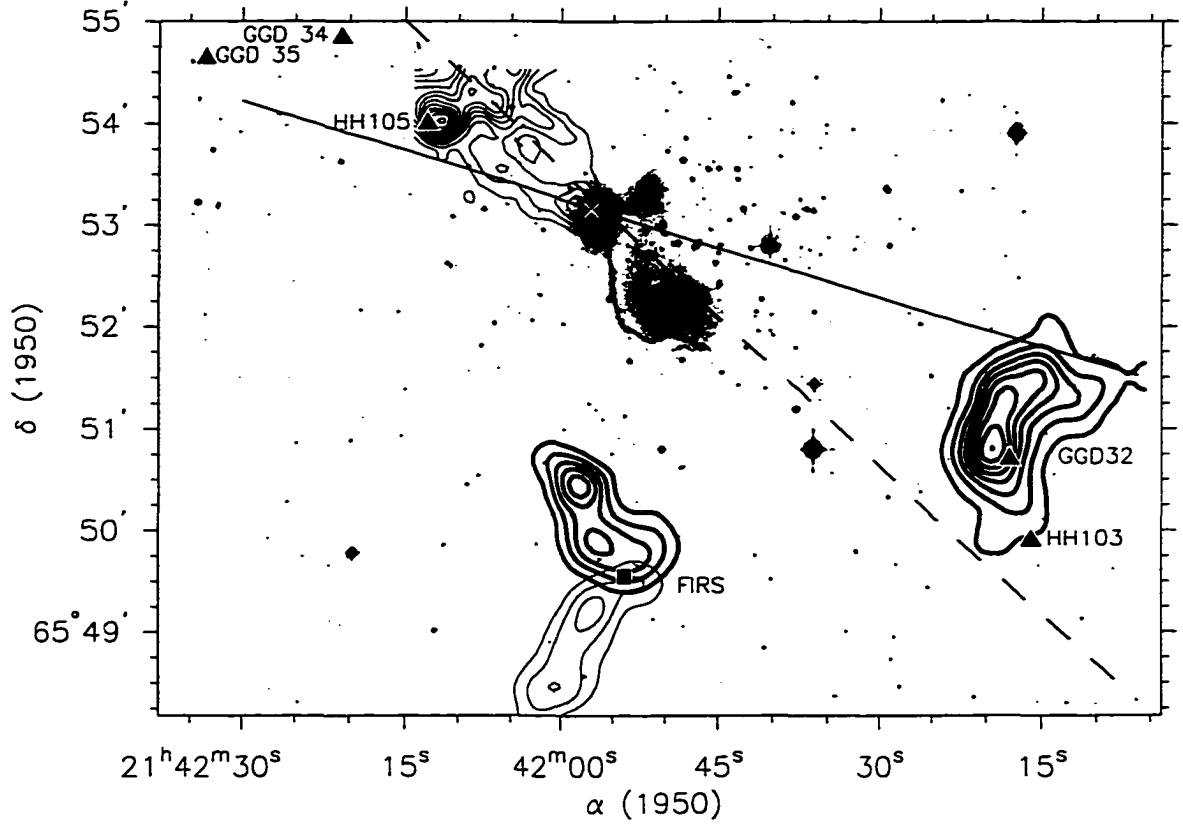
Figure 17. High Velocity ^{12}CO J = 3 → 2 Gas in NGC 7129. The K' image is from Figure 1. The thickness of the contours have the same meaning as for Figure 15. The jet axes are as previously defined in Figure 15. The position of LkHα 234 is marked by a cross. The contours of the high velocity gas near GGD 32/HH 103 are over the velocity range -16 to -15 km s^{-1}. For the blue and red lobes of the FIRS the contours are over the intervals -16 to -15 km s^{-1} and -7 to -6 km s^{-1} respectively. The contours of the redshifted outflow associated with LkHα 234 are over the velocity range -3.5 to -3.0 km s^{-1}. The contour base level and interval for both lobes of the FIRS and the high velocity gas near GGD 32 are both 1.0 K km s^{-1}. The base level and interval for the redshifted outflow associated with LkHα 234 are each 0.5 K km s^{-1}.

The jet axes are as shown in Figure 15. Near LkHα 234, the optical jet axis of 252° fits the redshifted outflow quite well (Mitchell & Matthews 1994). Further out along the outflow (≈30″) the infrared jet axis of 226° is a better fit. Neither proposed jet axis satisfactorily intersects the high velocity blueshifted gas. However, the two axes essentially bound the gas to the southwest, giving some support for an open wind. It is interesting to note that geometrically LkHα 234 lies very close to a line drawn from HH 105 to GGD 32 which would support the idea of a single source for both HH objects.

Emission from the blueshifted lobe of the FIRS is present over the velocity range -18.5 to -12 km s^{-1}. The emission from the redshifted lobe extends over the velocities -8 to -3 km s^{-1}. There is a remarkable symmetry between the two lobes of the outflow seen in both this transition and in ^{12}CO J = 2 → 1. The orthogonal geometry, as projected onto the plane of the sky, is striking. Each lobe has two J = 3 → 2 intensity peaks. In the blue lobe, the two peaks are at (7″, -161″) [α(1950) = 21^h 41^m 58.3^s, δ(1950) = 65° 50′ 26″] and (-3″, -196″) [α(1950) = 21^h 41^m 56.3^s, δ(1950) = 65° 49′ 53″] with the former peak more intense that the latter. In the red lobe, the two peaks are at (27″, -281″) [α(1950) = 21^h 42^m 0.6^s, δ(1950) = 65° 48′ 27″] and (2″, -241″) [α(1950) = 21^h 41^m 57.2^s, δ(1950) = 65° 49′ 12″], with the latter peak being of greater intensity. Spectra from the J = 3 → 2 intensity peaks, as well as from the position of the FIRS, are given in Figure 18. For comparison the J = 2 → 1 spectra from the two peaks in that transition and the FIRS are also shown. Both ^{12}CO spectra from the position of the FIRS have extended red and blue wings. The spectra have redshifted and blueshifted maxima, but no maximum at the quiescent velocity. Both J = 3 → 2 spectra from the blueshifted peaks have a single maximum with very extended blue wings and no maximum at the ambient velocity. The J = 3 → 2 spectra from each of the redshifted intensity peaks have two maxima, one at redshifted velocities and the other at slightly blueshifted velocities. The J = 2 → 1 spectra are very similar in shape to the corresponding J = 3 → 2 spectrum. Again, there is no maximum at ambient velocities, and the spectra have very extended wings. The average position angles for the red and blue lobes, obtained using both the ^{12}CO J = 2 → 1 and J = 3 → 2 data, are approximately 142° and 26° respectively.
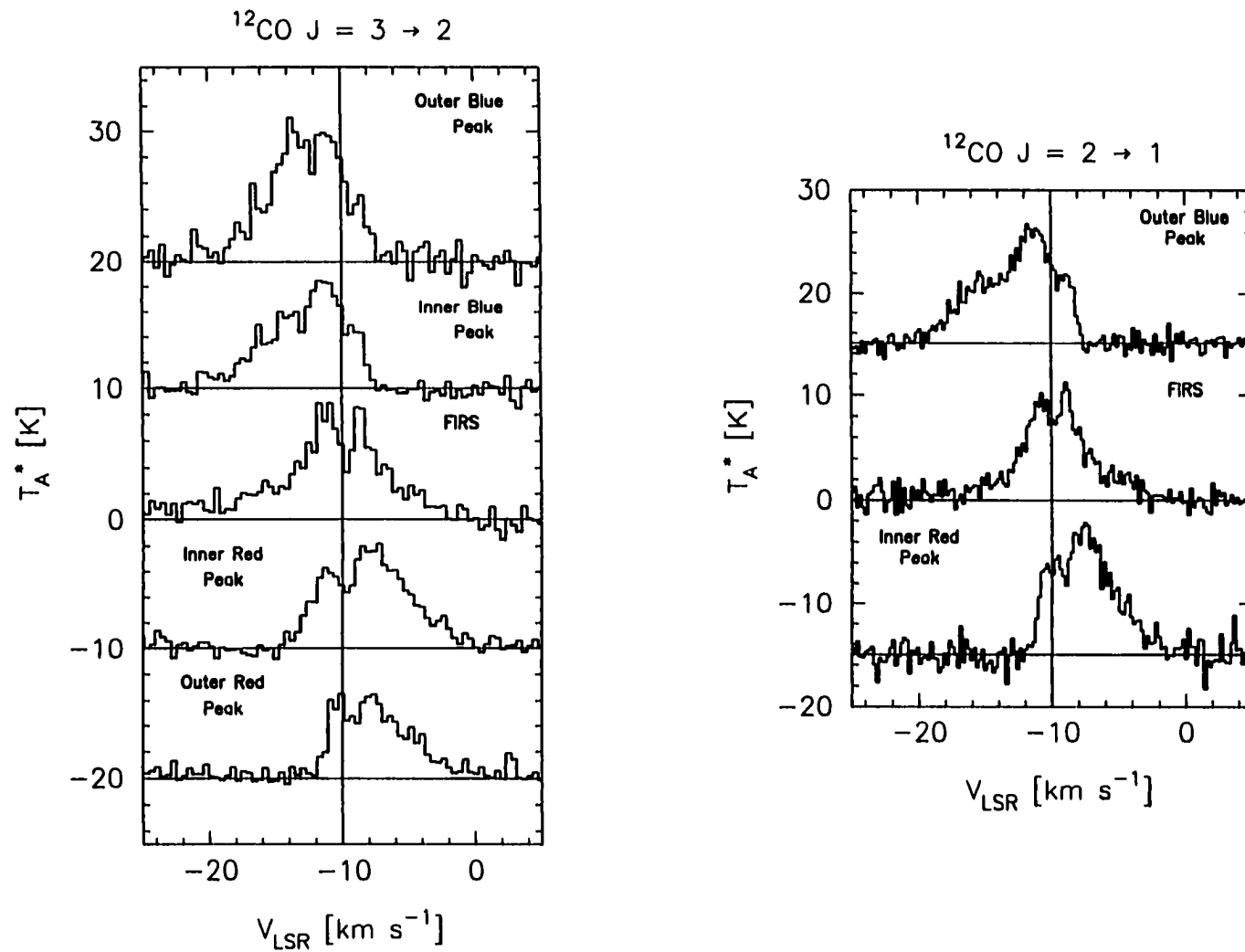
Figure 18. ^{12}CO Spectra from the Bipolar Outflow of the FIRS. The ^{12}CO J = 3 → 2 spectra (left set) are from both blueshifted peaks (top two), the position of the FIRS (middle), and both redshifted peaks (bottom two). The ^{12}CO J = 2 → 1 spectra (right set), where "inner" and "outer" refer to the position of the J = 3 → 2 peak. Again, the middle spectrum is from the position of the FIRS.

As noted in the previous section, redward of $=$-9 km s^{-1} the ^{13}CO J = 3 → 2 emission is confined to the immediate vicinity of LkHα 234 and the region to the northeast in the direction of the ^{12}CO molecular outflow. Three ^{13}CO integrated intensity maps of the region about LkHα 234 and the molecular outflow are shown in Figure 19. For comparison, the corresponding ^{12}CO integrated intensity maps of the outflow are shown to the right of the ^{13}CO maps. The top pair of maps, (a), are over the velocity range -9 to -8 km s^{-1}. In this velocity range the strongest emission in both transitions is associated with LkHα 234. The outflow in ^{13}CO has a sinuous and clumpy appearance. Extended structures as seen in ^{12}CO may be masked by ambient gas in this velocity range. The inner position angle of the ^{13}CO outflow is $=$20°, and that of the ^{12}CO outflow is $=$10°. The outflow as seen in ^{12}CO is coincident with that of the inner ^{13}CO outflow. The ^{13}CO outflow has a number of intensity peaks, the strongest at (60″, 30″), whereas, the ^{12}CO intensity peaks are at (75″, 60″) and (100″, 50″). The next in the series of maps is over the velocity range - 8 to -7 km s^{-1}. Compared to the velocity interval above, the outflow in ^{13}CO is somewhat straighter and has a single intensity maximum northeast of LkHα 234 at (60″, 30″). The outflow in ^{12}CO is more extended in this interval, comparable in both extent and position angle ($=$65°) with the ^{13}CO outflow. The ^{12}CO intensity maximum is further northeast of LkHα 234 at (75″, 65″). The last pair of maps are over the velocity range -7 to -6 km s^{-1}. Emission at the position of LkHα 234 is not detected in ^{13}CO but is in ^{12}CO. In both transitions a "backward C" feature is evident out in the outflow. The ^{13}CO redshifted gas is visible out to $=$-5 km s^{-1}, whereas the greatest extent of emission in the ^{12}CO outflow is $=$+2 km s^{-1}.

In a region centred approximately on (20″, 25″) [α(1950) = 21^h 42^m 0.4^s, δ(1950) = 65° 53′ 32″] with a diameter of $=$30″, there is a peculiar triple-peaked structure to the ^{12}CO spectra. Shown in Figure 20 are the ^{12}CO and ^{13}CO J = 3 → 2 spectra, and the ^{12}CO J = 2 → 1 spectrum at an offset of (30″, 30″) [α(1950) = 21^h 42^m 2.0^s, δ(1950) = 65° 53′ 38″]. The ^{12}CO spectra have a triple-peaked structure (two redshifted peaks, one blueshifted), whereas the ^{13}CO spectrum has a double-peaked structure (one at the ambient velocity, the other redshifted). Evidently the outflow, in this particular region, has complex structure.
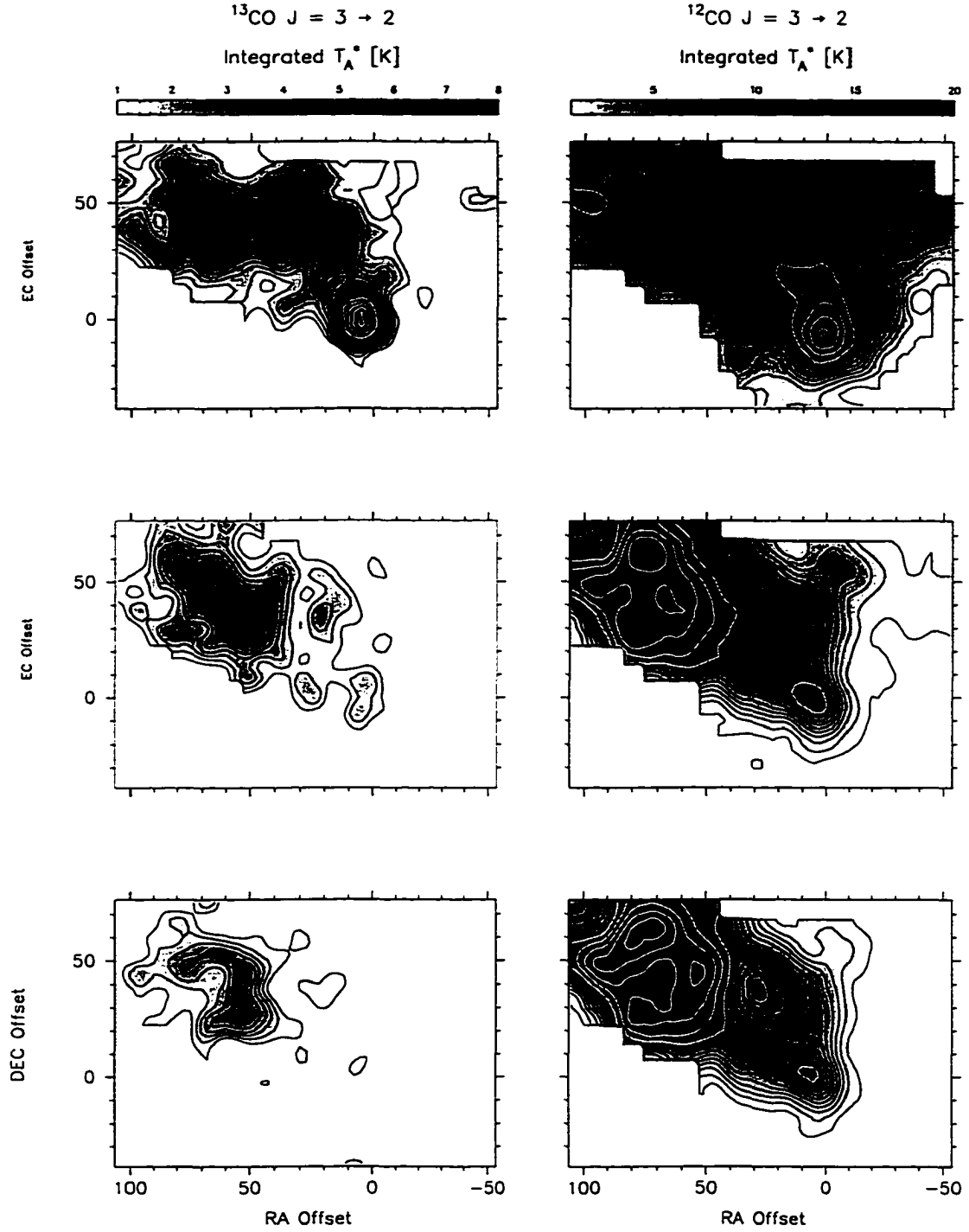
Figure 19. The Molecular Outflow Associated With LkHα 234 As Seen in ^{12}CO and ^{13}CO J = 3 → 2. Each pair of maps is for a particular velocity interval: (a) -9 to -8 km s^{-1}, (b) -8 to -7 km s^{-1}, and (c) -7 to -6 km s^{-1}. The ^{13}CO contours have a base level and interval of 1.0 and 0.5 K km s^{-1} respectively. The ^{12}CO contours increase in steps of 1.0 K km s^{-1} between 1.0 and 10.0 K km s^{-1}, and then increase in 2.0 K km s^{-1} steps up to 20.0 K km s^{-1}.
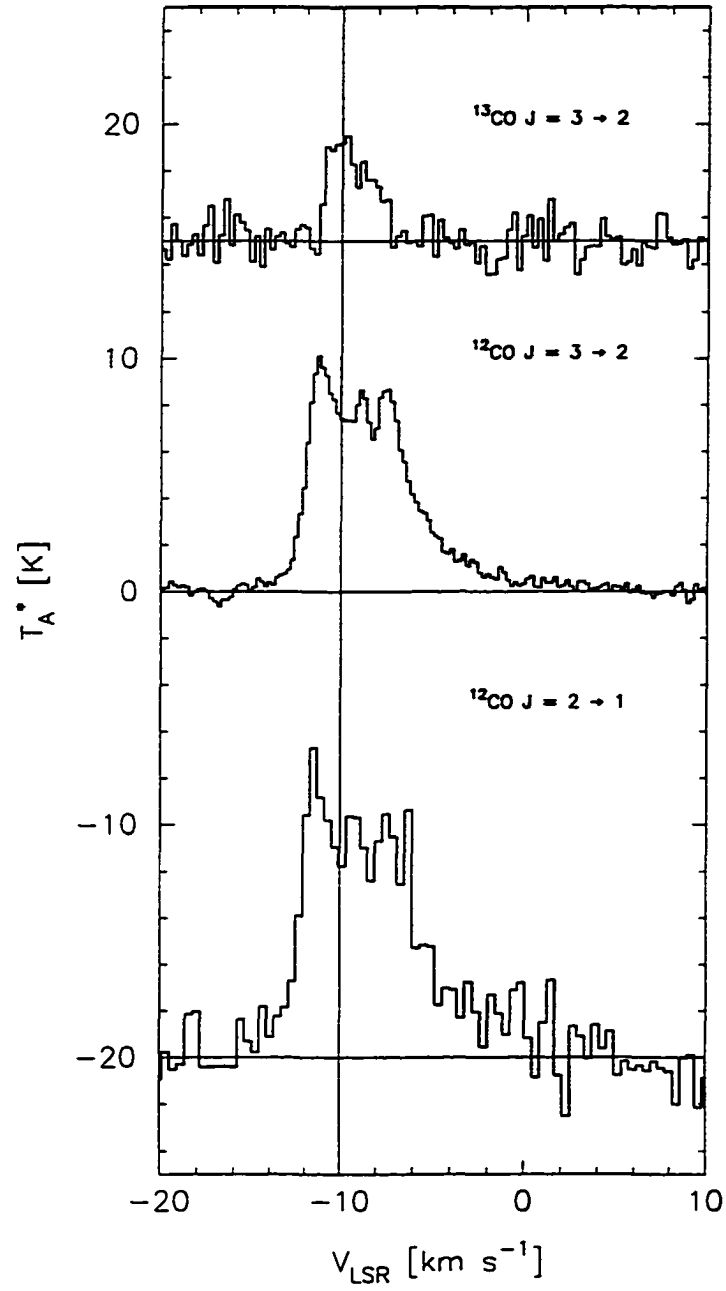
Figure 20. ^{13}CO and ^{12}CO Emission in the Outflow Associated With LkHα 234 at (30″, 30″). This position lies within the region where the ^{12}CO spectra are triple-peaked.

Figure 21 is an integrated HCO^+ $J = 3 \rightarrow 2$ intensity map over the velocity interval -8 to -7 km s^{-1}.

There is an intensity peak centred on LkHα 234, and a peak in the molecular outflow at (55″, 45″) [α(1950) = 21^h 42^m 6.2^s, δ(1950) = 65° 53′ 54″]. Extended redshifted emission in the outflow is present

only in the narrow velocity range shown in this figure. The HCO^+ peak in the outflow does overlap with

the region of peculiar triple-peaked ^{12}CO spectra mentioned above. Whether the peculiar spectra are a result

of an interaction of outflowing material with a dense clump will require further investigation. HCO^+,

$^{12}C^{18}O$, and ^{13}CO $J = 3 \rightarrow 2$ spectra from a position near the HCO^+ peak in the outflow are shown in

Figure 22. The HCO^+ and $^{12}C^{18}O$ $J = 3 \rightarrow 2$ spectra exhibit a detached red wing which is indicative of

moving gas. The red wing of the HCO^+ spectrum is particularly

extended, out to ≈+1 km s^{-1}. The ^{13}CO $J = 3 \rightarrow 2$ spectrum has a semi-detached wing. For all three

spectra, emission at the redshifted peak is approximately equal to that at the ambient velocity. The

redshifted peak in each transition occurs at the same velocity (≈-7.5 km s^{-1}).

The ^{13}CO $J = 3 \rightarrow 2$ spectra from the red lobe of the FIRS are shown in Figure 23. The positions

of each point of observation relative to that of the FIRS (α(1950) = 21^h 41^m 53.86^s,

δ[(1950) = +65° 49′ 33″) are indicated on Figure 24. These coordinates are a new JCMT position for the

submillimetre continuum source (Sandell 1996). If ^{13}CO was detected the appropriate symbol on the figure

is encompassed by a circle. For the FIRS, ^{13}CO is detected at all observation points. In most positions a

detached red wing is not present, but in all spectra an extended red wing is present.

The ^{13}CO $J = 3 \rightarrow 2$ spectra from the region of the high velocity blueshifted gas are shown in

Figure 25. In a number of positions no line is visible, possibly due to a low signal-to-noise ratio. The blue

wings are not as extended as the red wings seen in the redshifted lobe of the FIRS. The positions of the

points of observation are given along with those of the components of GGD 32 and HH 103 in Figure 26.

The symbols used in this figure are the same as those for the FIRS figure. It can be seen from the figure

that the northern components of HH 103 lie at the southern boundary of the moving gas. Nearly all of the

components of GGD 32 are coincident with the high velocity blueshifted gas. This may indicate that the

Herbig-Haro objects are embedded within the high velocity gas.
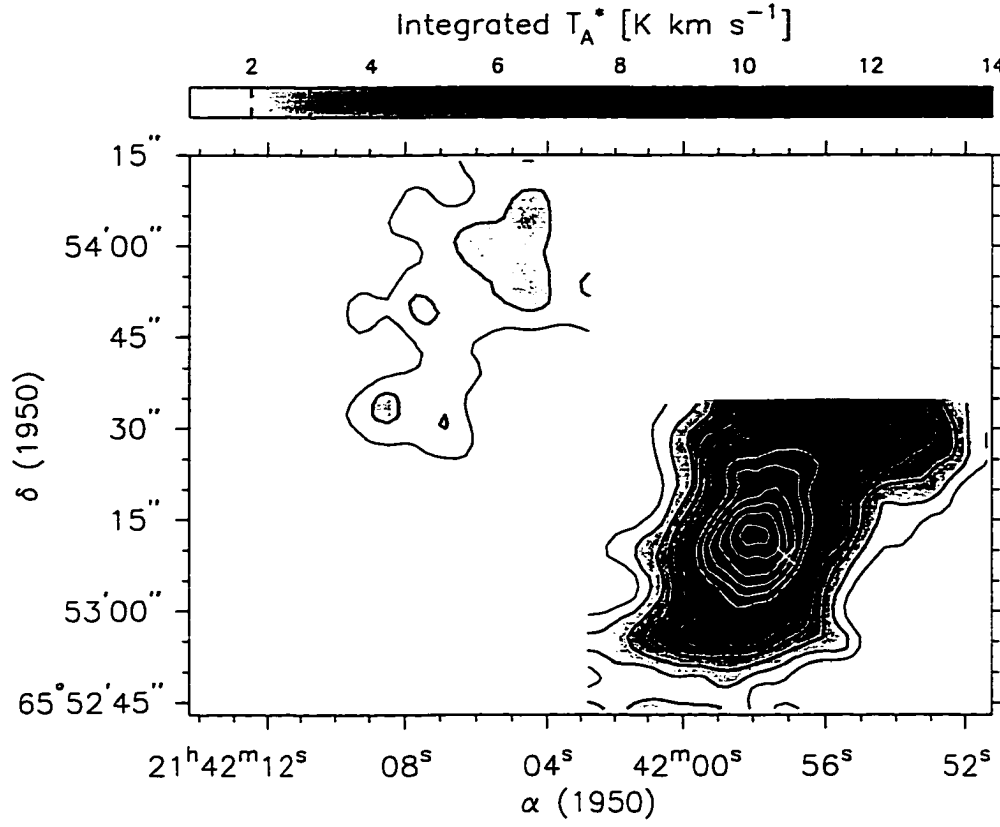
Figure 21. High Velocity HCO⁺ J = 3 → 2 Gas Near LkHα 234. The cross marks the position of LkHα 234. The greyscale is integrated intensity over the velocity interval -8 to -7 km s⁻¹. The contour base level and interval are both 0.25 K km s⁻¹.
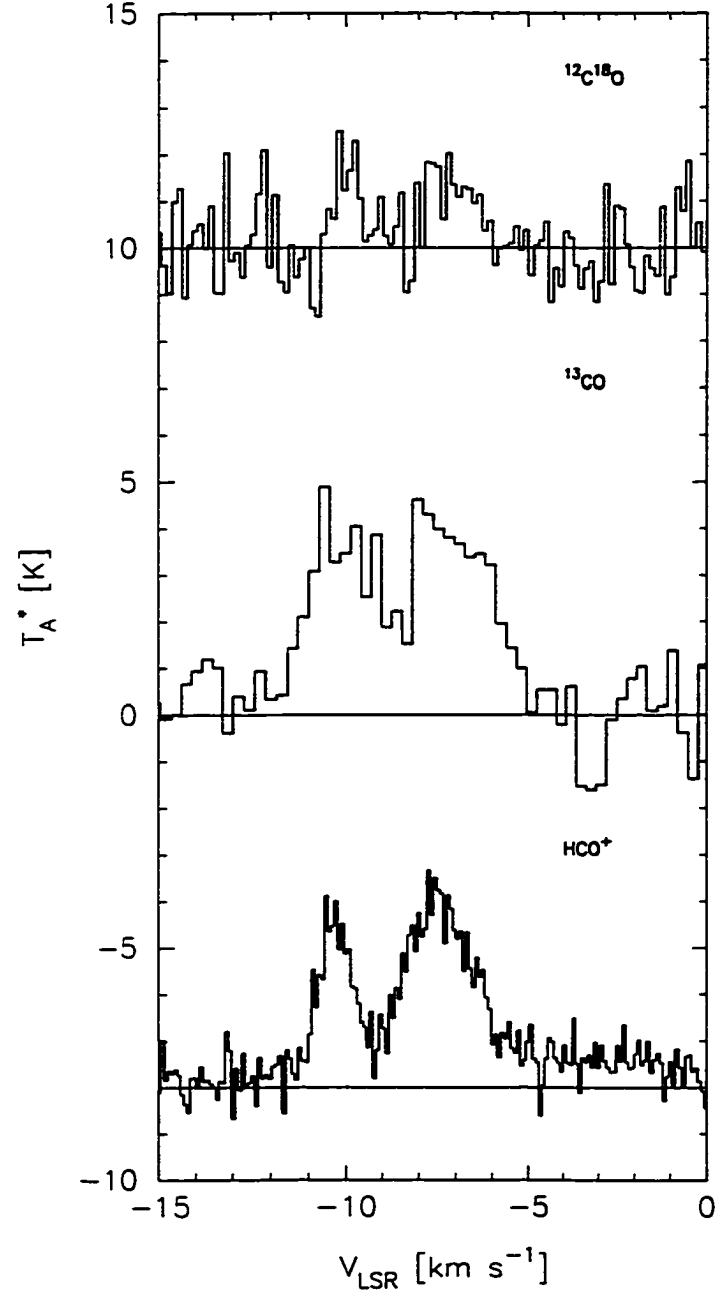
Figure 22. Emission Detected in the Outflow Associated With LkHα 234 at (52.5″, 37.5″). Both the $^{12}C^{18}O$ and HCO$^+$ J = 3 → 2 spectra have been multiplied by a factor of two. The $^{12}C^{18}O$ spectrum was twice binned. The wing of the HCO$^+$ J = 3 → 2 spectrum extends out to a velocity of +1 km s^{-1}.
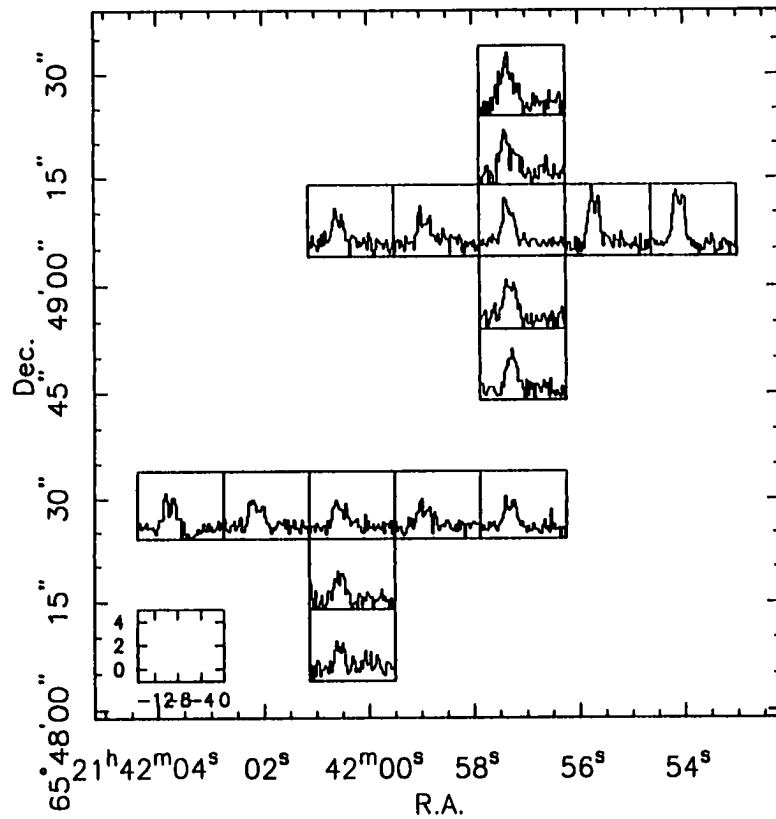
Figure 23. Grid-Spectrum of ^{13}CO J = 3 → 2 Observed Near FIRS. All spectra have been twice binned.
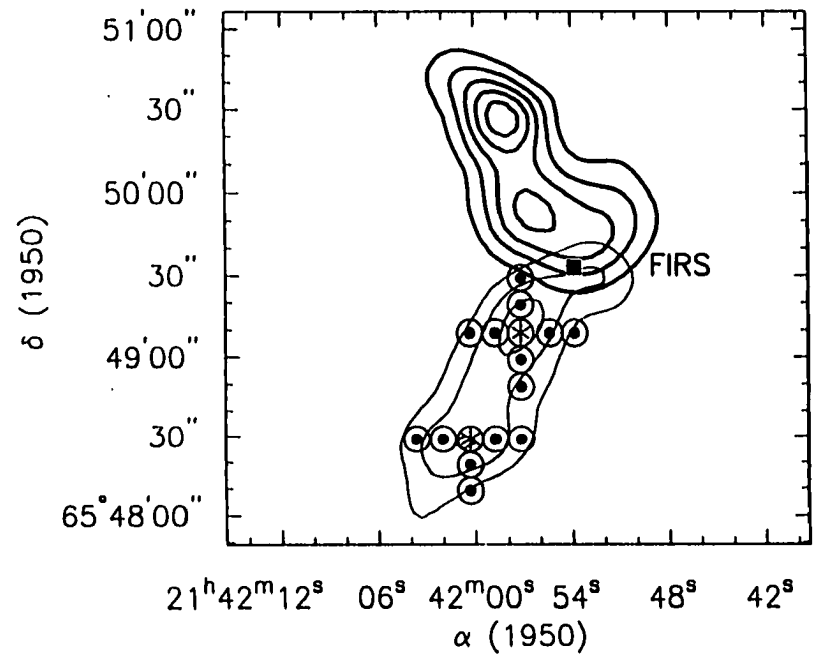
Figure 24. ^{13}CO Points of Observation With Respect to the Position of the FIRS. An asterisk indicates a position that was observed more than once while a dot indicates a single observation. In either case, if ^{13}CO was detected the appropriate symbol is encompassed by a circle. The contours are the same as those in Figure 17.
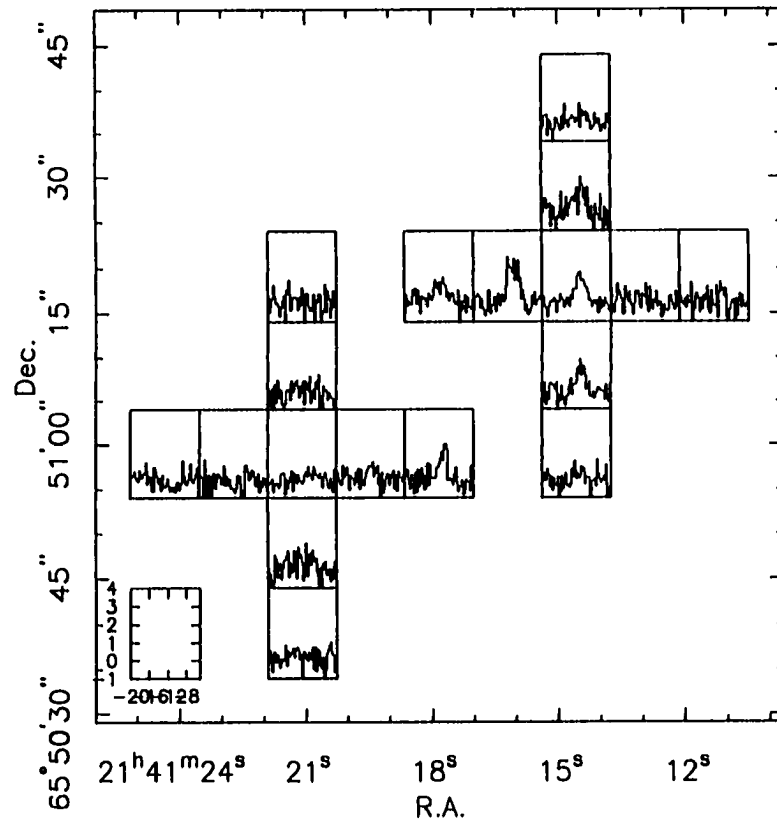
Figure 25.   Grid-Spectrum of ^{13}CO J = 3 → 2 Observed Near GGD 32 and HH 103. All spectra have been binned twice.
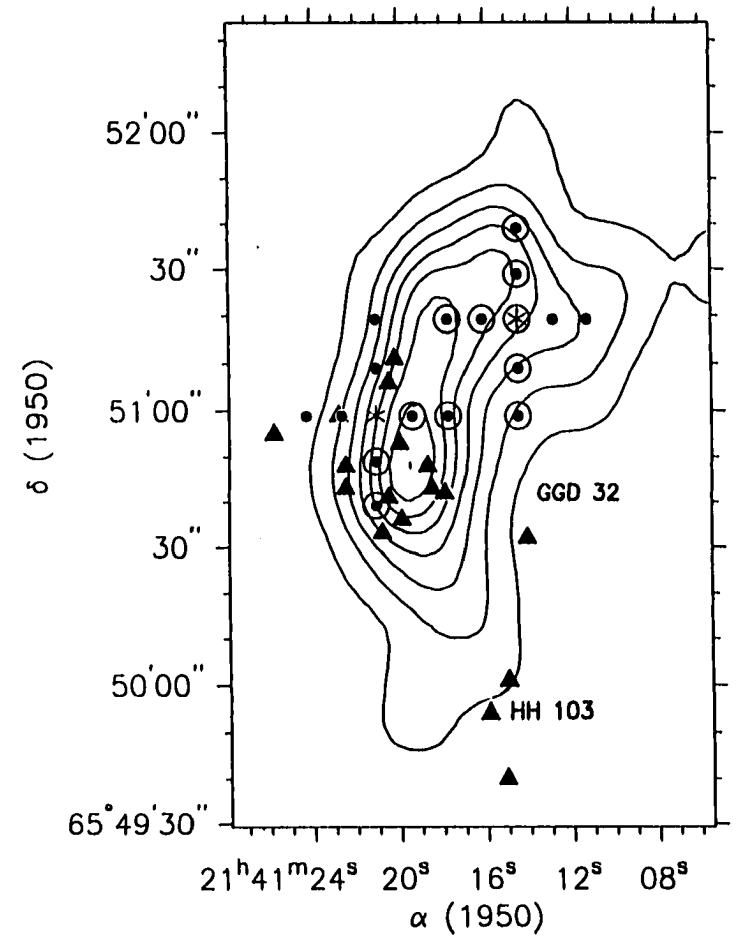
Figure 26. ^{13}CO Points of Observation With Respect to the Positions of GGD 32 and HH 103. The symbols are defined as in Figure 24. The contours are the same as those for Figure 17.

A schematic of NGC 7129 is given in Figure 27. The four brightest stars are marked. as well as the HH objects in the region. Both the ambient and high velocity gas is included. The molecular cavity, as indicated. is more open on the eastern and southeastern boundaries than on the western edge.
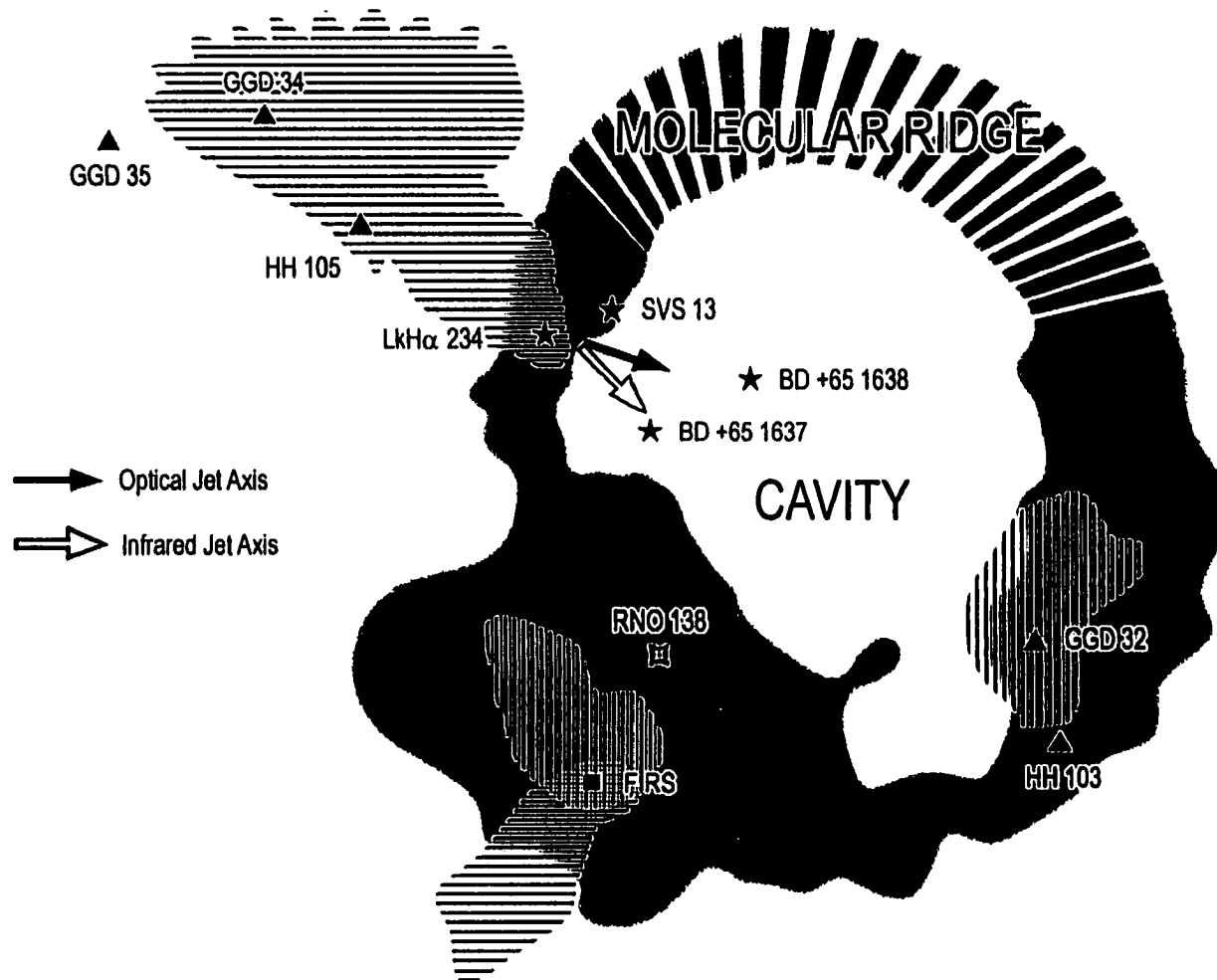
Figure 27. Schematic of NGC 7129. The brightest stars are marked, as are the HH objects. The ambient molecular ridge surrounding the cavity is indicated by greyscale. High velocity redshifted gas is marked by horizontal lines, whereas blueshifted high velocity gas is shown by vertical lines. Dashed lines represent regions where no data is available.

4 METHODS OF DETERMINING PHYSICAL PARAMETERS

4.1 Radiation Temperature, Optical Depth, and Excitation Temperature

The quantity recorded at the telescope is antenna temperature, T_A^*, which is dependent on the particular telescope used. The antenna temperature is defined as the observed intensity corrected for antenna and telescope losses (Matthews 1994). Antenna temperature is related to the radiation temperature, T_R, through

$$T_R = \frac{T_A^*}{\eta_{MB} f} \qquad\qquad 1$$

where η_{MB} is a measure of the deviation of the beam pattern from one that is Gaussian (Matthews 1994), and f is the filling factor of the gas observed. The radiation temperature is defined as

$$T_R = \frac{h\nu}{k}(1 - e^{-\tau_\nu})\left(\frac{1}{e^{\frac{h\nu}{kT_{ex}}} - 1} - \frac{1}{e^{\frac{h\nu}{kT_{cb}}} - 1}\right) \qquad\qquad 2$$

where h is the Planck constant, k is the Boltzmann constant, ν is the frequency of the transition, τ_ν is the optical depth along the line of sight at that frequency, T_{ex} is the excitation temperature of the source, and T_{cb} is the temperature of the cosmic microwave background (2.7 K). The term involving T_{cb} may be dropped when $T_{ex} \gg T_{CMBR}$ (Mitchell *et al.* 1992). If $T_{ex} > 4$ K, then the first term of (eq. 2) is at least

a factor of seven greater than the term involving T_{cb}. For many regions in the interstellar medium, including NGC 7129, this assumption is valid and the second term may be excluded when calculating T_R. Since the radiation temperature depends on both optical depth and excitation temperature, an independent method to determine one of the two variables is desired.

If the radiation temperatures of two isotopomers in the same state are available, then one can use (eq. 2) to find the optical depth for one of the molecules. The method requires the assumption that *the excitation temperatures for both isotopomers are approximately equal*. The optical depth for either isotopomer may be found if the abundance ratio, α, for the two isotopes is known. Given two isotopomers, A and B, in the same rotational state their respective optical depths are given by the line ratio

$$\frac{T_R^A}{T_R^B} = \chi (T_{ex}) \frac{1 - e^{-\alpha \tau^B}}{1 - e^{-\tau^B}} \qquad 3$$

and

$$\tau^A = \alpha \tau^B \quad . \qquad 4$$

The function $\chi(T_{ex})$ has the form

$$\chi (T_{ex}) = \frac{\nu^A}{\nu^B} \frac{e^{\frac{h\nu^B}{kT_{ex}}} - 1}{e^{\frac{h\nu^A}{kT_{ex}}} - 1} \quad . \qquad 5$$

If $\chi(T_{ex})$ is approximately equal to one, then this function may be excluded from (eq. 3), greatly simplifying

the calculations. Where the ^{12}CO and ^{13}CO $J = 3 \rightarrow 2$ transitions are of interest $\alpha = 60$ (Langer &

Penzias 1990). For the ^{12}CO to ^{13}CO line ratio, $\chi(T_{ex})$ has the functional dependence shown in Figure 28.

As long as $T_{ex} > 5$ K the effect of $\chi(T_{ex})$ on the radiation temperature ratio is an decrease of less than a

10%. For the ^{12}CO to ^{13}CO line ratio, this simplification is valid. Since the frequency difference between

the ^{13}CO and $^{12}C^{18}O$ transitions is very small (1.3 GHz), $\chi(T_{ex})$ may be excluded from (eq. 3) for these

calculations as well. The abundance ratio between ^{13}CO and $^{12}C^{18}O$ is 10 (Penzias 1981). In terms of

observables, the ^{13}CO optical depth may be found, *provided the filling factors of ^{12}CO and ^{13}CO $J = 3 \rightarrow 2$

are approximately equal*, using

$$\frac{\eta_{MB}^{13}}{\eta_{MB}^{12}} \frac{(T_A^*)^{12}}{(T_A^*)^{13}} \approx \frac{1 - e^{-60\tau^{13}}}{1 - e^{-\tau^{13}}} \,. \qquad 6$$

A graph of the above relation is shown in Figure 29, with the physically forbidden regions marked. The

region of positively sloped hatching, $\tau < 0$, is excluded by the definition of optical depth. The function

itself is asymptotic at $(T_R$ ratio$) = 1.0$, excluding ratios < 1.0 (the region with negatively sloped hatching).

The region between $(T_R$ ratio$) = 0.0$ and 1.0, corresponding to a $T_R(^{12}CO) < T_R(^{13}CO)$, is forbidden for

theoretical reasons. A negative temperature ratio is obviously unphysical. Due to the asymptotic nature

of the function, the optical depth is well determined when $\tau(^{13}CO) < 1.2$, or $\tau(^{12}CO) < 72$.

Once the optical depth is known, it may be used in conjuction with the radiation temperature to

find the excitation temperature. Using equations 1 and 2 for molecule A, and solving for T_{ex} yields,

$$T_{ex} = \frac{\dfrac{hv^A}{k}}{\ln\left[\dfrac{hv^A}{k} \dfrac{1}{T_R^A} (1 - e^{-\tau^A}) + 1\right]} \,. \qquad 7$$
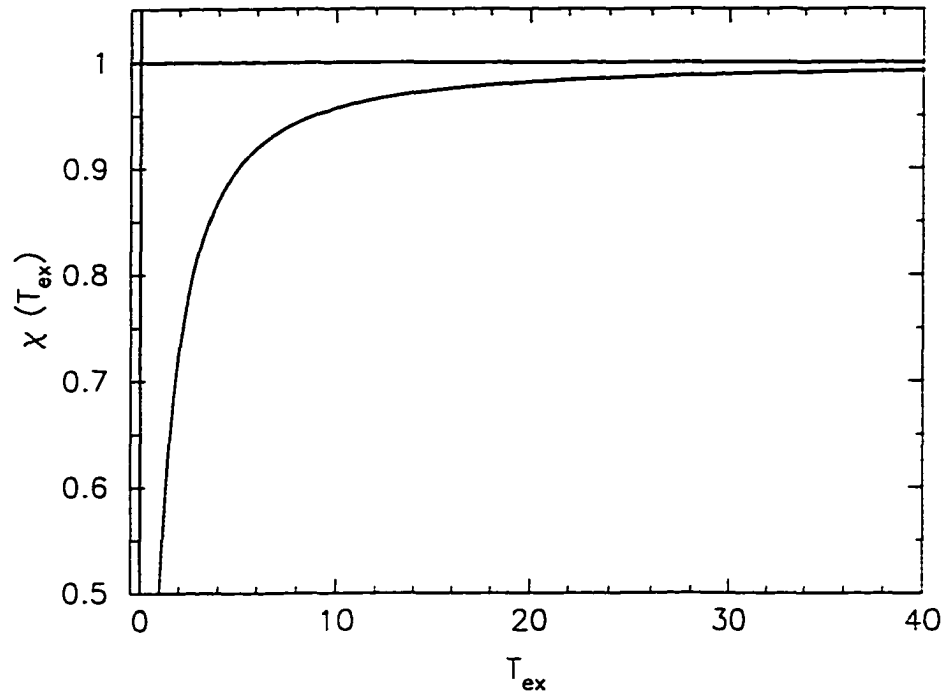
Figure 28. Graph of the T_{ex}-Dependent Factor in the Radiation Temperature Line Ratio.
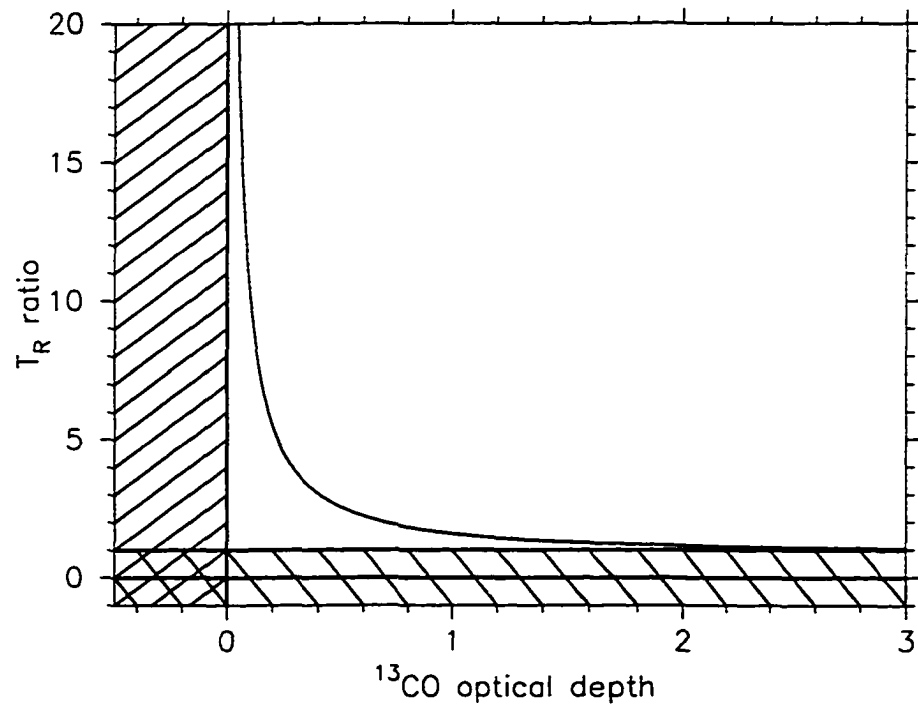
Figure 29. Graph of Radiation Temperature Ratio versus ^{13}CO Optical Depth. Physically the radiation temperature ratio cannot be negative, and theoretically it must be greater than one (negatively sloped hatching). The optical depth must be positive (positively sloped hatching).

In particular, the T_{ex} for ^{12}CO is found with the results from (eq. 3) using the ^{12}CO and ^{13}CO $J = 3 \rightarrow 2$ line ratio:

$$T_{ex} = \frac{16.595}{\ln\left[\frac{16.595}{T_R^{12}}(1 - e^{-\tau^{12}}) + 1\right]} \; K \; . \qquad 8$$

A contour plot of T_{ex}, as dependent on radiation temperature and optical depth, is given in Figure 30. As can be seen from the contours for a given T_R, the excitation temperature decreases very slowly as the optical depth grows large $(\tau^{12} > 5)$. The largest values of T_{ex} occur for low optical depth and high radiation temperature combinations. For the ^{13}CO excitation temperature determined from the ^{13}CO to $^{12}C^{18}O$ ratio a constant of 15.865 must be used in the above equation instead of 16.595.

4.2 Column Density

Due to the length of the derivation of the expression for column density, the full derivation is given in Appendix A. With the assumption of Local Thermodynamic Equilibrium (LTE), the equation for the column density of CO gas in a given rotational state and in a given velocity interval, Δv_l, has the form

$$N = \frac{3k}{8\pi^3 B\mu^2} \frac{T_{ex} + \frac{hB}{3k}}{J + 1} \frac{e^{\frac{hBJ(J+1)}{kT_{ex}}}}{1 - e^{-\frac{h\nu}{kT_{ex}}}} \tau^{12}\Delta v \qquad 9$$

where J is the rotational quantum number of the lower state, μ is the dipole moment of the molecule in
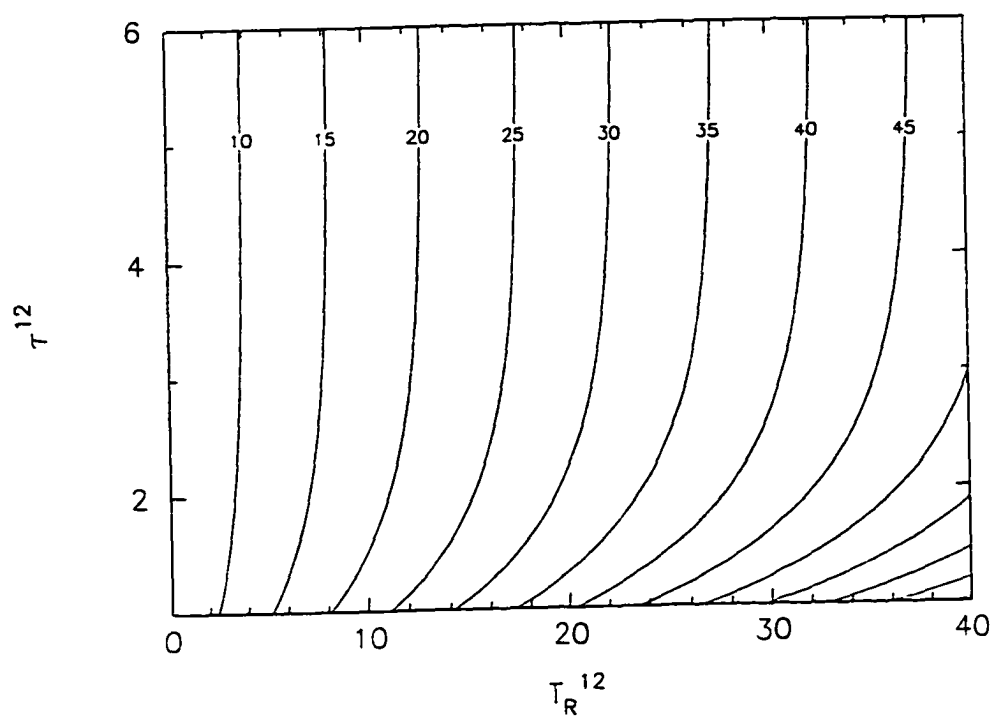
Figure 30. Excitation Temperature as a Function of ^{12}CO Optical Depth and Radiation Temperature. The excitation temperatures are indicated on the contours.

question and B is its rotational constant. The velocity interval, Δv_r, used for the calculation could be as narrow as the channel width or as wide as a few km s^{-1}. Referring to Appendix A, it is important to note that a given calculation of column density is an average over the beam area *for the specific velocity interval stated.* As one can see from the form of (eq. 7), the column density is directly proportional to the width of the velocity interval. The dependence of column density on excitation temperature is more complex. For ^{12}CO, $\mu = 1.12 \times 10^{-19}$ esu-cm and B = 5.764×10^{10} Hz (Giannakopoulou 1994). If the transition of interest is J = 3 → 2, then the rotational quantum number is equal to 2, and the specific equation for this transition is

$$N^{12} = (7.698 \times 10^8)(T_{ex} + 0.922) \frac{e^{\frac{16.597}{T_{ex}}}}{1 - e^{-\frac{16.595}{T_{ex}}}} \tau^{12} \Delta v \ cm^{-2}. \qquad 10$$

Note that in this equation the constants in the exponential terms are dependent on the isotopomer considered. All other constants are valid for all isotopomers of carbon monoxide as long as the transition examined is the J = 3 → 2 transition. Figure 31 is a contour plot of column density as a function of excitation temperature and optical depth for the particular case of the ^{12}CO J = 3 → 2 transition. As can be seen from the graph, for a fixed optical depth there is a minimum in column density at an excitation temperature of approximately 10 K. The greatest values of column density occur for high optical depth, high excitation temperature combinations.
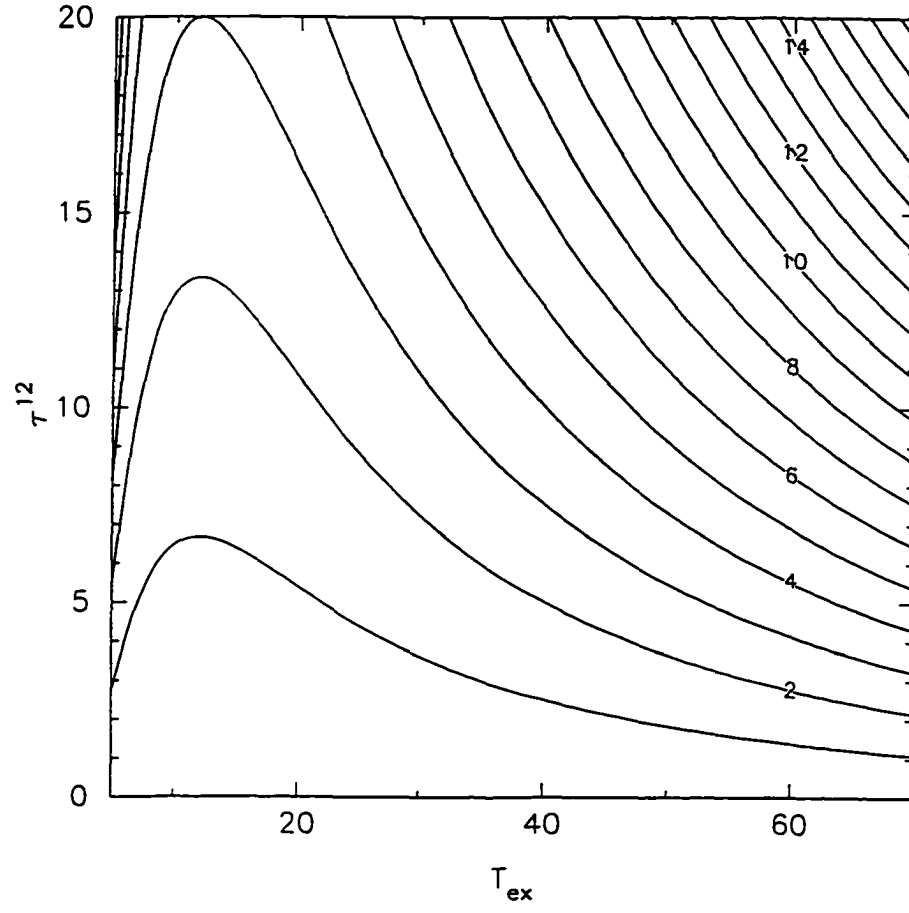
Figure 31. Contour Plot of Column Density, $N^{12}(T_{ex}, \tau^{12})$. Each curve is labelled with the value of column density in units of 10^{16} cm^{-2}.

4.3 Mass

In order to calculate the mass contained in a velocity interval, one must first find the column density of molecular hydrogen. For the sources considered in this paper, an abundance ratio of 10^4 is assumed between the H_2 and ^{12}CO column densities (Mitchell 1993). In order to calculate the surface density over the region observed, the beam area, in the appropriate units, must be known. For an angular beam area of approximately $15''$ at a distance of 1 kpc (Racine 1968), the area at the source is 3.95×10^{34} cm^2. If the distance to NGC 7129 is 1.25 kpc, as suggested by Shevchenko and Yakubov (1989), then the beam area at the source is 6.18×10^{34} cm^2. The surface density for a given velocity interval, Δv_j, is defined as

$$\sigma_j = 1.4 \cdot N_j (H_2) \cdot 2 m_H$$

11

where the factor of 1.4 is an adjustment for the abundance of helium (Mitchell 1993), $N_j(H_2)$ is the column density of molecular hydrogen in the given velocity interval, and m_H is the mass of a hydrogen atom. Now, the mass per velocity interval (in $M_\odot$) may be calculated via:

$$m_{s_j} = \frac{A\sigma_j}{M_\odot}$$

12

where A is the beam area, and $M_\odot$ is the mass of the sun.

4.4 Momentum and Kinetic Energy

If one is interested in the kinematics of the region, the momentum and kinetic energy contained in a velocity interval may respectively be calculated as

$$P_j = \frac{(v_j - V_{LSR})}{\cos \theta} m_{s_j},$$ 13

and

$$E_{k_j} = \frac{1}{2} \frac{(v_j - V_{LSR})^2}{\cos^2 \theta} m_j$$ 14

where θ is the orientation of the jet with respect to the line of sight, and v_j is the mean average velocity within the chosen velocity interval Δv_j. The equations given above are designed to calculate the kinematical quantities with respect to the cloud/source velocity for a jet. Thus, both the momentum and kinetic energy vanish at the V_{LSR}.

4.5 Optically Thin Approximation

The optically thin method employs the approximation that $\tau \ll 1$. Again, one only has the definition of radiation temperature from (eq. 2). Because the radiation temperature is dependent on both optical depth and excitation temperature, one of the variables must be set by some other means. The excitation temperature or optical depth calculated through the methods given in the above paragraphs may be used as an input value, or, if that is not possible, another analysis technique may be used to find an excitation temperature.

If one has two transitions of a given molecule available, it is possible to find an excitation temperature. The full derivation is given in Appendix B. The assumption here is that *the excitation temperatures for both transitions of the molecule are equal.* The relationship between the optically thin excitation temperature and the radiation temperatures may be expressed as

$$\frac{T_R^A}{T_R^B} = \frac{J_A^2}{J_B^2} \exp\left[-\frac{hB}{k}\left(J_A(J_A + 1) - J_B(J_B + 1)\right)\right]$$

15

where J_A and J_B are the lower states of the two transitions. In terms of the ^{12}CO J = 3 $\rightarrow$ 2 and J = 2 $\rightarrow$ 1 transitions, and *assuming that the filling factors for the two transitions are approximately equal,* the excitation temperature may be found as,

$$T_{ex} = \frac{-\frac{hB}{k}}{\ln\left(\frac{4}{9} \frac{\eta_{MB}^{21}}{\eta_{MB}^{32}} \frac{(T_A^*)^{32}}{(T_A^*)^{21}}\right)} \quad K.$$

16

This relationship is plotted in Figure 32. The function does have an asymptote which is dependent on the particular transitions involved. For this example, the excitation temperature is approximately linear in radiation temperature ratio for ratios less than one. For larger ratios, T_{ex} becomes unbounded (at $T_R = 2.25$ K in this example) after which this equation gives unphysical (negative) values of T_{ex}. Once the excitation temperature has been calculated, the optical depth may be found from (eq. 2). In Figure 33, the dependence of optical depth on excitation temperature is shown. For all radiation temperatures observed in this thesis, if $T_{ex} \geq 10$ K, then $\tau < 9$.

In general, the column density in the optically thin regime may be found using the relationship

$$N_{thin} = \frac{3k}{8\pi^3 hBv\mu^2} \frac{(T_{ex} + \frac{hB}{3k})}{J + 1} \frac{e^{\frac{hBJ(J + 1)}{kT_{ex}}}}{e^{-\frac{hv}{kT_{ex}}}} T_R \Delta v \quad . \qquad 17$$

The full derivation is given in Appendix B. It is important to note that the column density is independent of optical depth. If the two transitions considered are ^{12}CO $J = 2 \rightarrow 1$ and $J = 3 \rightarrow 2$, then the above equation gives

$$(N^{12})_{thin} = (4.639 \times 10^7)(T_{ex} + 0.922) \frac{e^{\frac{16.597}{T_{ex}}}}{e^{-\frac{16.595}{T_{ex}}}} \frac{T_A^*}{\eta_{MB}} \Delta v \quad K \qquad 18$$

A contour plot of column density as a function of $J = 3 \rightarrow 2$ radiation temperature and excitation temperature is given in Figure 34. The highest values of column density occur for large T_{ex} and large $(T_A^*)^{32}$ combinations.. The equations to calculate the mass, momentum, and kinetic energy are the same as (eq.10) through (eq. 12).
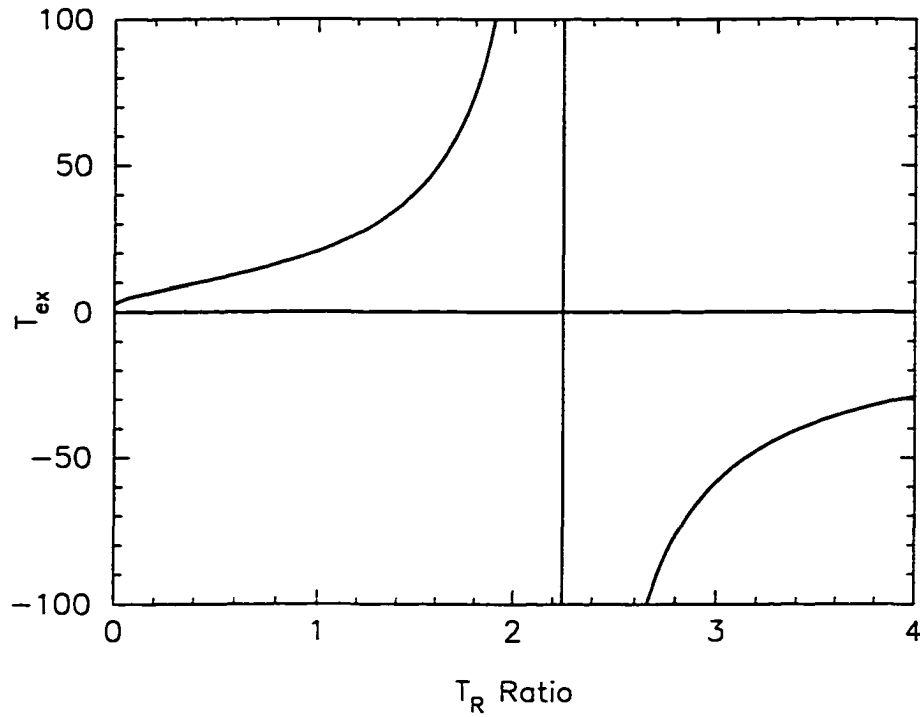
Figure 32. Plot of Excitation Temperature versus Radiation Temperature Ratio for the Optically Thin Regime. This graph shows the transition-dependent asymptote. The constants used to produce this graph are for the ^{12}CO J = 3 → 2 to J = 2 → 1 line ratio.
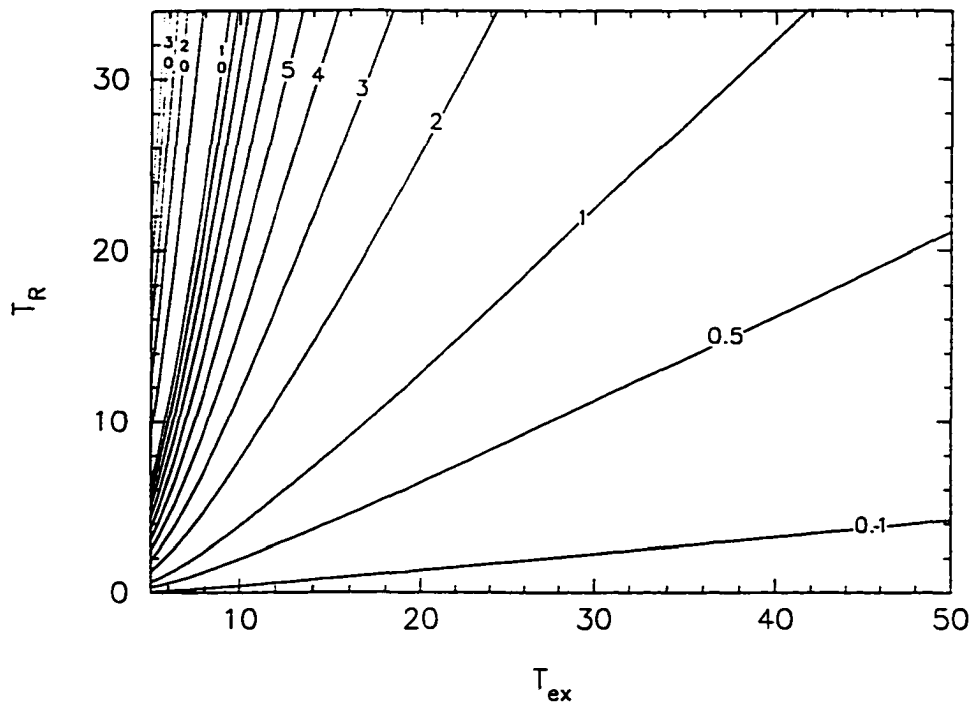
Figure 33. Contour Plot of Optically Thin Optical Depth. The optical depth is a function of excitation temperature and ^{12}CO J = 3 → 2 radiation temperature.
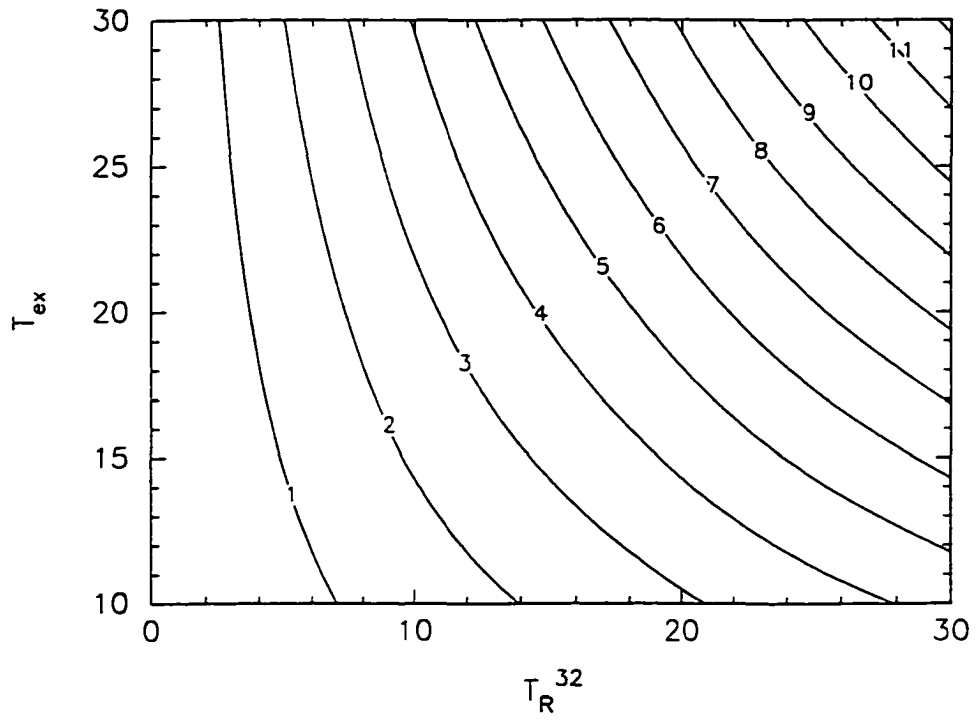
Figure 34. Contour Plot of Optically Thin Column Density. The column density is a function of ^{12}CO J = 3 → 2 radiation temperature and excitation temperature. Each curve is labelled with the value of column density in units of 10^{14} cm^{-2}.

4.6 Notes on the Effects of Self-Absorption and Filling Factors

In order to accurately interpret the results of calculations when the methods described above have been used, there are two effects which must be considered. One is that the observed line shapes may have been altered by the process of self-absorption. The other is that a beam filling factor less than unity can reduce the strength of the line. producing an observed line shape that is lower in temperature than the actual line. These physical effects will lead to an underestimation of some quantities, and an overestimation of others.

If the physical situation is such that there is an extended, cooler, less dense envelope surrounding a hot, dense core then self-absorption may occur. The cooler gas in the foreground will absorb photons emitted from molecules in the core. The more abundant the species, the greater the effect. For example, consider emission from the $J = 3 \rightarrow 2$ transition of the isotopomers ^{12}CO and ^{13}CO where the former is the more abundant species. If the ^{12}CO spectrum exhibits self-absorption it is not necessarily true that the less abundant species will also be self-absorbed at the same position. If the more abundant species is the only species exhibiting self-absorption, then it is possible to estimate upper or lower limits to the actual values. If both species are self-absorbed then it is not possible from those two transitions to determine the effects on the calculations without additional information.

Consider the ^{12}CO and ^{13}CO $J = 3 \rightarrow 2$ transitions where only the ^{12}CO spectrum is self-absorbed. Self-absorption, by definition, produces a lower antenna temperature than would normally be observed and results in a lower radiation temperature (eq. 1). The lower radiation temperature for the more abundant species leads to a radiation temperature ratio that is artificially low. From the graph of optical depth versus radiation temperature ratio (Figure 29) it can be seen that an artificially low radiation temperature ratio produces an increase in the optical depth. Using the self-absorbed antenna temperature will give a value which is an upper limit to the actual, pre-self-absorbed value of optical depth. A decrease in the excitation temperature results from the artificially low ^{12}CO radiation temperature and artificially high optical depth (Figure 30), so the temperature obtained from the uncorrected data will be a lower limit to the actual

excitation temperature. The effect on the column density is not as apparent. An examination of Figure 31 shows that if the excitation temperature is reduced and the optical depth is increased. then it is not known whether the altered column density lies above, below, or on the contour corresponding to the actual value.

In the range of ^{12}CO and ^{13}CO antenna temperatures considered here. and hence the optical depths and excitation temperatures, the partial derivative of the column density (eq. 9) with respect to the ^{12}CO radiation temperature may be of either sign. The curve defined where this partial derivative is equal to zero, or the curve of invariant column density, *for no self-absorption and all filling factors equal to one.* is given in Figure 35. The curve has been superimposed on the column density contours of Figure 31. To the left of the curve of invariant column density the derivative is negative, and to the right it is positive.

To determine the sign of the partial derivative for a particular value of self-absorbed column density, an estimate of the amount of self-absorption is required. For a every value of self-absorption there is an associated curve of invariant column density. Figure 36 is a plot of the curves of invariant column density for self-absorptions of 0 and 5 K, overlaid on the column density contours. The symbols marked on the curves indicate how a value is mapped from the curve for a self-absorption of 0 K onto the 5 K self-absorbed curve. Self-absorption maps a point originally on the curve of invariant column density for 0 K, *along a column density contour.* to a position corresponding to a higher optical depth and lower excitation temperature. If the self-absorbed value of column density lies on the appropriate shifted curve, then it is equal to the actual column density. If the self-absorbed value of column density lies to the left of the shifted curve of invariant column density then it is a lower limit to the actual value since the derivative is negative. To the right of the curve, where the derivative is positive, the self-absorbed value is an upper limit to the actual value. The effects of using the self-absorbed ^{12}CO antenna temperature on the calculations is summarized in Table 4.
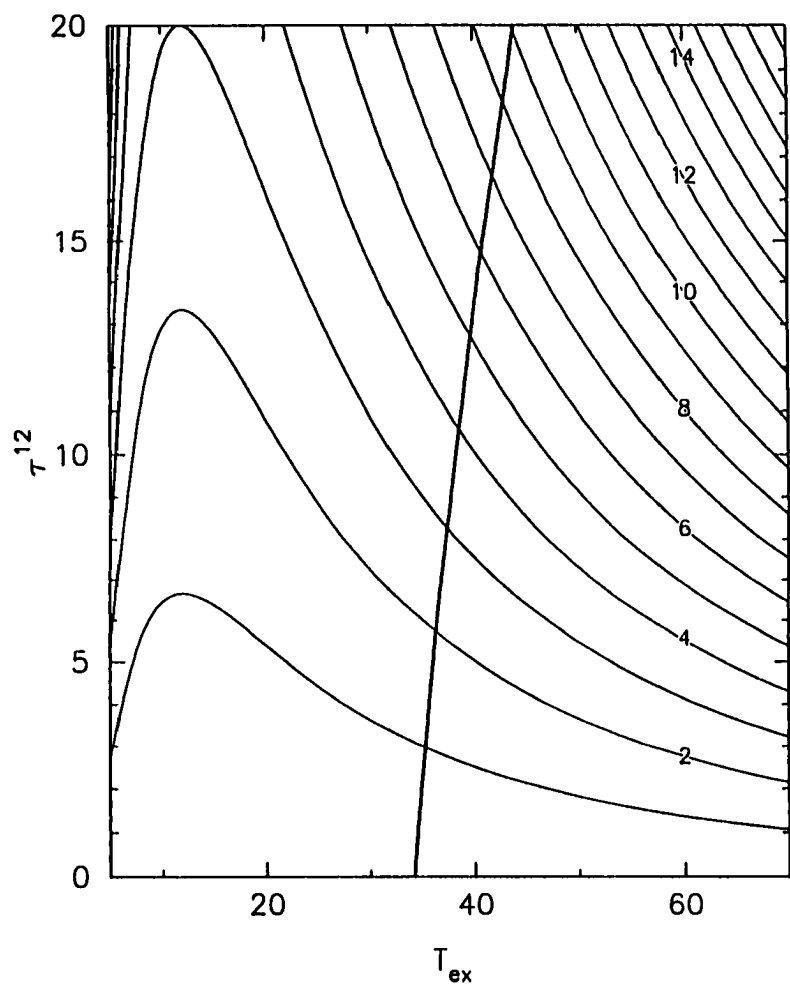
Figure 35. Curve of Invariant Column Density for Zero Self-Absorption. The curve is superimposed on the contours of the column density function (Figure 31). To the left of the curve, the partial derivative of column density is negative, and to the right it is positive.
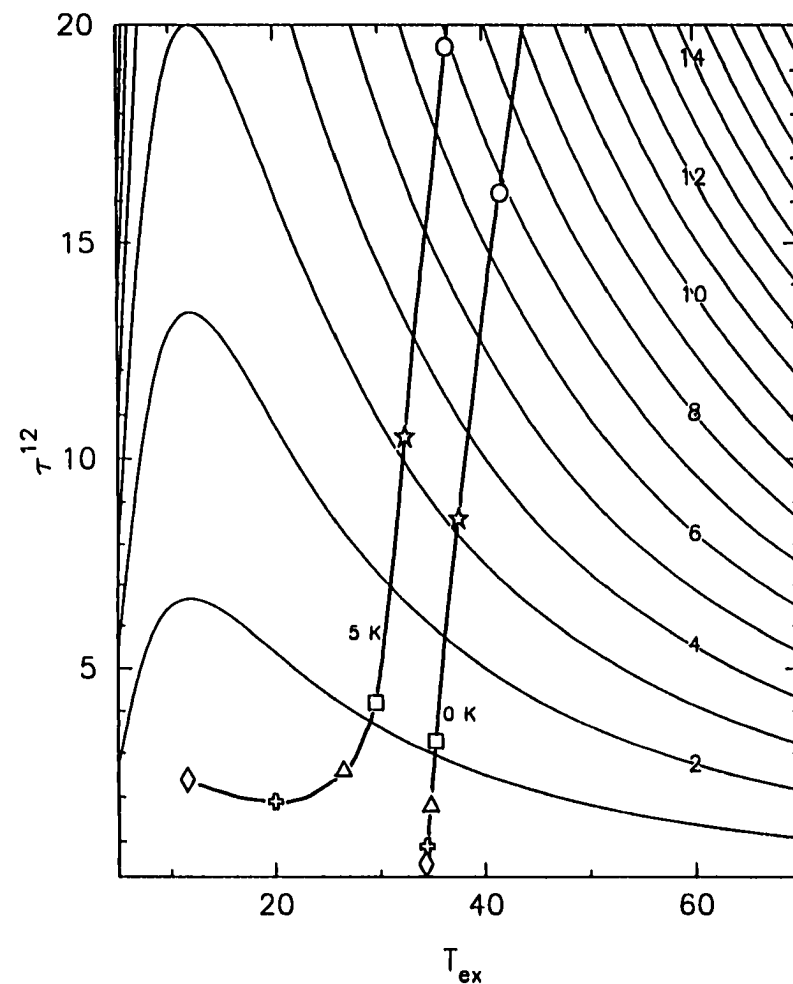
Figure 36. Curves of Invariant Column Density for Self-Absorptions of 0 and 5 K. The two curves are labelled, with temperatures, for the amount of self-absorption, and are superimposed on the contours of Figure 31. The other symbols indicate how a point on the curve for no self-absorption maps onto the 5 K self-absorption curve.

Table 4. Effects of Using a Self-Absorbed T_A^* On Calculated Quantities. For the ^{12}CO column density the situations are: (1) value lying to the left of the relevant curve of invariant column density; (2) value lying on the relevant curve of invariant column density; and (3) value lying to the right of the relevant curve of invariant column density.

Calculated Quantity		a Lower Limit	Unaffected	an Upper Limit
τ^{12}				✓
T_{ex}		✓		
^{12}CO N	(1)	✓		
	(2)		✓	
	(3)			✓

When comparing the emission at a particular transition from two isotopomers, the emission line from the less abundant species which traces the denser gas is less optically thick than that of the more abundant isotopomer (Genzel 1991). As a result the denser gas may be clumpier than the less dense gas. From (eq. 1) it can be seen that a filling factor less than one for the ^{13}CO J = 3 → 2 transition produces an increase in the ^{13}CO radiation temperature. This will decrease the T_R ratio used to find the optical depth, and results in an increased optical depth (Figure 29) and a decreased excitation temperature (Figure 30). An examination of the partial derivative of the column density with respect to the ^{13}CO radiation temperature shows that a reduction in the ^{13}CO filling factor changes the optical depth and excitation temperature in such a way as to follow the curve of invariant column density for the case of all filling factors equal to one and no self-absorption. The effect on the column density is then given by the situation shown in Figure 35. Assuming that both the ^{12}CO and ^{13}CO filling factors are equal to one, when the latter is actually less than one, produces the same effects on the calculated values summarized in Table 4.

Filling factor effects can also come into play in the optically thin situation. Since the excitation energy increases as the rotational quantum number increases, it would be expected that the emission originating from the hottest regions would have a lower filling factor than widespread emission from cooler surroundings. For example the ^{12}CO J = 2 → 1 transition might have a larger filling factor than the J = 3 → 2 transition. As previously stated, a filling factor less than one leads to an increase in the J = 3 → 2 radiation temperature (eq. 1) which increases the T_R ratio. This produces an increase in the excitation temperature (Figure 32). The partial derivative of optical depth (eq. 2, rearranged) with respect to the J = 3 → 2 radiation temperature is negative for all values. An increase in radiation temperature and excitation temperature would result in a decrease in optical depth (Figure 33). Since the derivative of the column density with respect to the J = 3 → 2 radiation temperature is always positive an increase in the radiation and the excitation temperatures produces an increase in the column density (Figure 34). Assuming that both the J = 2 → 1 and J = 3 → 2 filling factors *are equal to one*, when the J = 3 → 2 filling factor may be less than one, results in upper and lower limits, as described in Table 5.

Table 5. Effects of Assuming Both Filling Factors Are Unity. If both the ^{12}CO J = 2 → 1 and J = 3 → 2 filling factors are assumed to be equal to one the following calculated quantities are either upper or lower limits to the actual values.

Calculated Quantity	a Lower Limit	an Upper Limit
J = 3 → 2 T_R	✓	
T_R ratio	✓	
T_{ex}	✓	
J = 3 → 2 τ		✓
J = 3 → 2 N_{thin}	✓	

5 ANALYSIS OF HIGH VELOCITY GAS

5.1 Procedure for Redshifted Outflow Associated with LkHα 234

Since complete maps of the outflow region in the transitions ^{12}CO J = 3 → 2 and ^{13}CO J = 3 → 2 were available, the kinematical properties of the outflow could be obtained. The intersection of the two maps is shown in Figure 37. Of the 264 positions observed, ^{13}CO J = 3 → 2 was detected for all but 15. These 15 positions are indicated in Figure 37 by dark grey shading, and are situated in the molecular cavity. For each position calculations of optical depth, excitation temperature, column density, mass, momentum, and kinetic energy were made for each velocity channel. The velocity interval where both ^{12}CO and ^{13}CO emission was detected will be said to belong to the "inner region". The "outer regions" are those sections of the ^{12}CO wing where no ^{13}CO emission was detected. In the outer regions, the gas was assumed to be optically thin, and the relevant equations were applied. The appropriateness of this assumption will be discussed in §6.1. The mass, momentum, and kinetic energy were calculated as described in the previous section for the blue, the inner red, and the outer red wings. For every quantity a graph of the value versus velocity channel was produced for each position observed. The error, per channel, for every quantity was also propagated. The procedure was, for the most part, automated due to the large number of calculations required.

In order to use these data in a C program, it must be in ASCII form. Using the SPECX function WRITE-ASCII-FILE (Padman 1992) one may produce an ASCII file of any spectrum in the SPECX buffer. This function, however, also includes the spectrum header in the output file which must be removed. Once this is done, the file may easily be read into any program. Since the ^{13}CO J = 3 → 2 spectra were more noisy than the corresponding ^{12}CO spectra, curves were fit, by hand, to 230 of 264 ^{13}CO spectra in an effort to reduce noise spikes induced by the nonlinear equations derived from theory. The fitting was done in a systematic manner. A continuous curve was fit to the original spectrum, with the odd exception due to
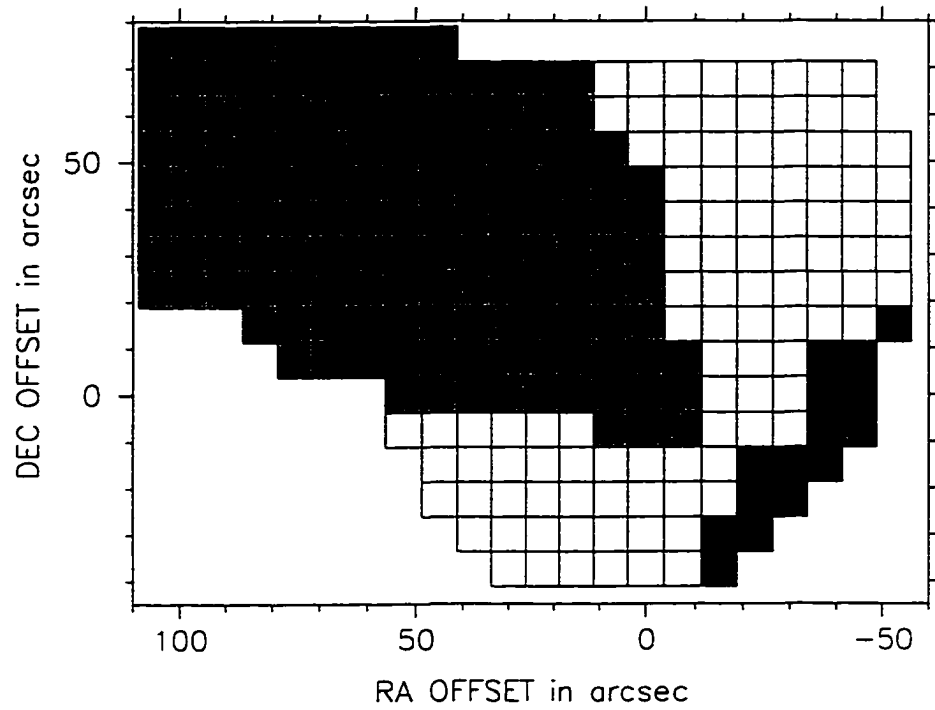
Figure 37. The Areas of Both ^{12}CO and ^{13}CO Observations. The dark grey squares represent positions where ^{13}CO was not detected. The area containing the molecular outflow is defined by the light grey squares. White squares indicate where ^{12}CO and ^{13}CO were detected, but not considered to be part of the outflow.

extreme noise. In those cases, the original spectrum was smoothed in order to more easily fit such a curve. The binning was usually done by a factor of two, but sometimes a factor of three or four was required. The curve was fit by eye, guided by the shape of a more highly binned spectrum. In most cases only a single wing or the central section of a given spectrum was noisy enough to warrant replacement by sampled data from the continuous curve. If a value for a channel was not significantly altered by the fitting, the original value was not replaced. In the segment of the spectrum concerned, the corresponding channels in the ASCII file were altered to those read off the fitted curve.

The error, σ, on a given spectrum (and on a given channel in the spectrum) was calculated according to Sage (1990). This method takes into account the uncertainty due to noise (T_{rms}) and the uncertainty in the determination of the baseline of the spectrum (Sage 1990). The T_{rms} is the sigma quoted by the function FIND-SPECTRUM-STATISTICS in SPECX (Padman 1992). The equation for the uncertainty due to the baseline, as well as the final form of the error equations are given in Appendix C. Two files for each position were created, one for each of the ^{12}CO and ^{13}CO spectra, consisting of the error for a single channel of the relevant spectrum.

With the files at this stage of analysis, the optical depths and excitation temperatures could be calculated. The first step was to resolve the problem of differing channel widths between the ^{12}CO and ^{13}CO spectra. Since the ^{12}CO spectra had the smaller channel width, they were rebinned to the channel width of the ^{13}CO spectra, reducing the velocity resolution of the ^{12}CO data. In order to rebin the data the channel boundaries had to be known for both data sets. The spectra from each data set at the position (-22.5", 7.5") were chosen as sample spectra. A velocity interval was chosen for each data set which encompassed every spectrum in that data set. For the ^{12}CO and ^{13}CO data sets, the velocity intervals chosen were {-28, 22} km s^{-1} and {-20, 10} km s^{-1} respectively. Using the interactive mode of SPECX, the boundary furthest from the V_{LSR} was found for the first and last channel of each interval. Due to the manner in which numbers are stored in electronic media, it was found that the channel width determined in the interactive mode oscillated between two values (not necessarily in a regular fashion). Using the interval boundaries an average channel width of approximately 0.215 and 0.283 km s^{-1} was calculated for

^{12}CO and ^{13}CO respectively. These values agree with the incremental frequency (in MHz) listed by SPECX in the headers of the spectra if one uses the Doppler shift formula to convert to km s^{-1}. From the average channel width, and the lower boundary of the last channel in the interval, the boundaries of each channel were found. The upper boundary of the first channel in the interval was used as a consistency check. Since the entire ^{12}CO spectrum must be rebinned, the boundaries for all ^{12}CO and ^{13}CO channels in the interval (-28, 22) km s^{-1} had to be calculated. Using these boundaries it was then possible to rebin all ^{12}CO spectra to the ^{13}CO boundaries. See Appendix D for details of the rebinning procedure.

In order to know when to switch to the optically thin equations for a given position, the velocity range of each ^{13}CO spectrum had to be known. The extent of each ^{13}CO spectrum was found via an iterative procedure. First, the spectra were visually inspected and the limits (or "limiting channels") chosen on the basis of where the wings of the spectrum appeared to fall to zero. Those channels with a T_A^* estimated to be equal to zero will be referred to as "end channels". The limiting channel for a particular wing of a spectrum was taken as the channel adjacent to the end channel which was closest to the V_{LSR}. Using an intermediate program over a velocity range greater than that of the ^{13}CO spectrum, the optical depths and excitation temperatures were calculated. The excitation temperatures about the channel limits for each position were then examined. If the excitation temperature for the given limiting channel met the following condition, it was taken as acceptable:

$$\sigma_{T_{ex}} \leq T_{ex} \quad . \qquad\qquad 19$$

If the error was greater than the excitation temperature, then the first channel in towards the line centre which satisfied the above condition was chosen. Finally, the ^{13}CO spectra were visually inspected again to see if the chosen limiting channels were reasonable. In all but two cases, they were.

The ^{12}CO limiting channels had to be known since it was desired to terminate the calculations at the end of the ^{12}CO wings. These ^{12}CO limiting channels were chosen by visual inspection alone. A rough

hand drawn curve was fitted to the wings of the spectrum. Again, the channels which were adjacent to the end channels were chosen as the limiting channels. In some cases, where the line appeared to decay into a noisy region a few channels before the channel initially assigned as an end channel, the last channel that could confidently be defined as belonging to the line was chosen as the new end channel. This was done in order to cut down on noise in the line wings.

The optically thin equations require as an input either an optical depth or an excitation temperature if one does not have a second transition. Since the available ^{12}CO $J = 2 \rightarrow 1$ data for the region was sparsely sampled (compared to the oversampled ^{12}CO $J = 3 \rightarrow 2$ data), the excitation temperature was chosen as the input quantity for the optically thin calculations in the outer regions. Once the excitation temperatures were calculated over the inner region the excitation temperatures for the blueshifted and redshifted ^{13}CO limiting channels were inspected for consistency with respect to neighbouring positions. It was found, for both sets of excitation temperatures associated with the limiting channels, that values from position to position across the map rarely agreed at the 1σ-level which was not acceptable. A strategy was developed to improve the agreement between neighbouring positions.

The following procedure will only be described for the redshifted limiting channel, but applies to the blueshifted one as well. The excitation temperatures of the limiting channels for each position were used to calculate two arrays: $T_{ex} + \sigma_{ex}$, and $T_{ex} - \sigma_{ex}$. These two arrays were separately read into SPECX using a specially written script, and two maps were created. Each map was smoothed using the SPECX function INTERPOLATE-MAP (Padman 1992). A HPBW of $15''$, and a radius of $25''$ were chosen as the interpolation parameters. The smoothed value for each position was read out of SPECX using the

interactive mode and entered into two new arrays. These arrays of interpolated values were then used to calculate a new excitation temperature and associated error for each position using the following:

$$\hat{T}_{ex} = \frac{\left[(T_{ex}+\sigma_{T_{ex}})' + (T_{ex}-\sigma_{T_{ex}})'\right]}{2} \qquad\qquad 20$$

$$\hat{\sigma}_{T_{ex}} = \frac{\left[(T_{ex}-\sigma_{T_{ex}})' - (T_{ex}-\sigma_{T_{ex}})'\right]}{2} + \left|T_{ex} - \hat{T}_{ex}\right| \qquad\qquad 21$$

where primes refer to smoothed values, and carats refer to new accepted values. The second term in the error equation is due to shifting T_{ex} to $\hat{T}_{ex}$. As can be seen from Table 6, this markedly improved the agreement in excitation temperatures between positions for the redshifted limiting channels as well as the blueshifted limiting channels. These new excitation temperatures (as given in Figure 38) were used for every channel in the outer wings of the ^{12}CO spectra where no ^{13}CO was detected.

For the positions where no ^{13}CO line was detected, the main problem was determining excitation temperatures. For simplicity, a single excitation temperature was chosen for each position in the following manner. First, two intermediate limiting excitation temperatures were found from the red and blue temperatures. Each was determined from an error-weighted average (Bevington & Robinson 1992) of a position's neighbouring values. This procedure had to be initiated from the positions at the edge of the region with known excitation temperatures and continued, iteratively, outward. An error-weighted average of the two resultant excitation temperatures was taken as the single excitation temperature for the cell. The excitation temperature obtained in this fashion was used for every ^{12}CO channel at a given position.

Table 6(a). Sample Red Wing Input Excitation Temperatures. These temperatures, given in Kelvins, are the values before smoothing. The errors are indicated in parentheses.

		RA OFFSET		
		-15.0″	-22.5″	-30.0″
DEC OFFSET	60.0″	15.8 (0.7)	14.8 (0.7)	12.6 (0.7)
	52.5″	17.0 (0.6)	18.7 (0.6)	15.8 (0.4)
	45.0″	17.0 (1.5)	22.6 (0.5)	12.0 (0.5)

Table 6(b). Sample Red Wing Input Excitation Temperatures. These temperatures, given in Kelvins, are the values after smoothing. The errors are indicated in parentheses.

		RA OFFSET		
		-15.0″	-22.5″	-30.0″
DEC OFFSET	60.0″	15.1 (1.7)	14.9 (1.0)	13.9 (2.3)
	52.5″	16.9 (1.4)	16.7 (2.7)	14.5 (1.9)
	45.0″	17.2 (1.3)	17.5 (5.8)	14.8 (3.4)

Figure 38(a). Input Excitation Temperatures. The excitation temperatures used as input for the optically thin calculations in the red wings of the ^{12}CO spectra are shown for each position. The standard deviations are indicated in parentheses.

DEC OFFSET in arcsec

50

0

Blue Wing Excitation Temperatures

100   80   60   40   20   0   −20   −40   −60

RA OFFSET in arcsec
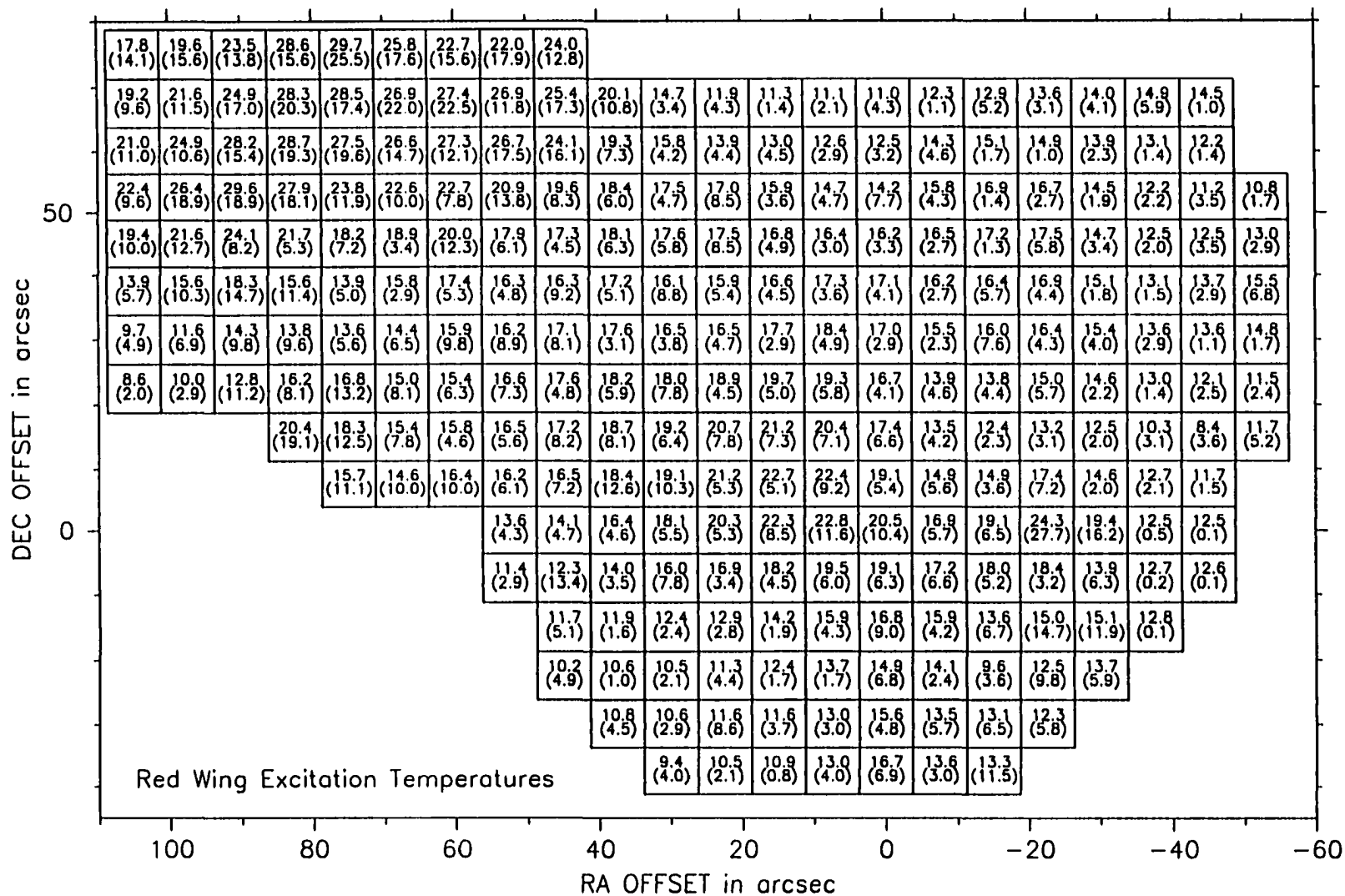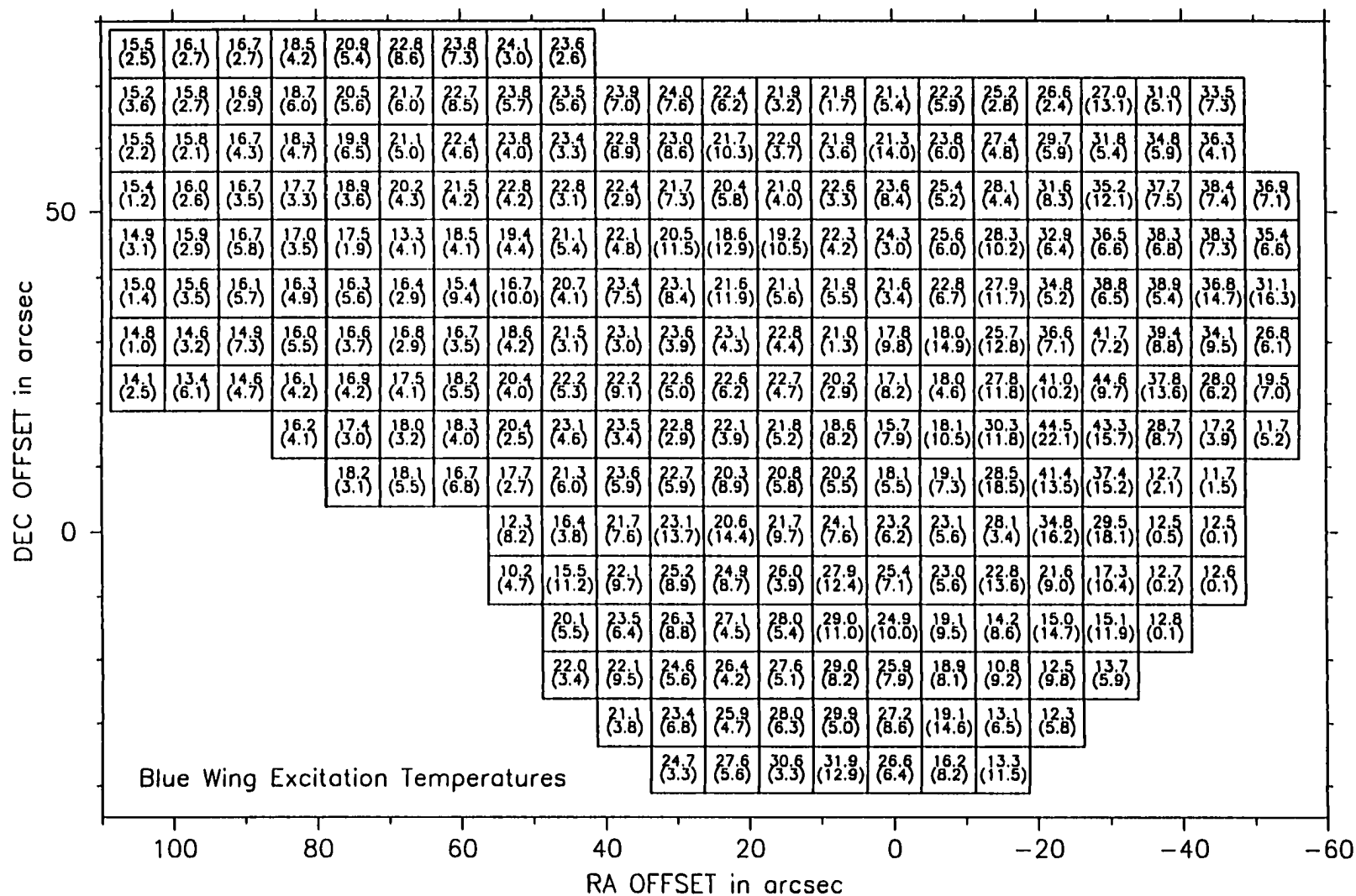
Figure 38(b). Input Excitation Temperatures (continued). The excitation temperatures used as input for the optically thin calculations in the blue wings of the ^{12}CO spectra are shown for each position. The standard deviations are indicated in parentheses.

78

With the ^{12}CO data rebinned, the ^{13}CO limiting channels chosen, and the input excitation temperatures for the optically thin calculations found, the optical depth could be calculated according to (eq. 2) and (eq. 6). For the inner region of the spectrum, a table of T_R ratios for given optical depths was produced with the respective filling factors set equal. An interpolation procedure was then used to find the correct optical depth for a given radiation temperature ratio. The errors on the optical depths were calculated following standard error propagation techniques (see, for example, Bevington & Robinson 1992). All error equations used by the author are given in Appendix C. At this point, the column density, mass, momentum, and kinetic energy could be calculated for every channel at each position.

As was mentioned earlier, the procedure was largely automated. The program PARAM.C was created to fulfil this task. Two types of files were output from the program: data files consisting of physical values and their associated errors, and files to be converted into FITS files. The mass, momentum, and kinetic energy were also calculated for every channel. These quantities were summed over the wings of the spectra to produce a total value for the blue wing, and the inner and outer red wings at each position. The blue wing was defined as those velocities blueward of -10.5 km s^{-1} in which ^{12}CO was detected. The inner red wing was defined as those velocities in the interval -9.5 to -8.0 km s^{-1}, and the outer red wing was defined as those velocities redward of -8.0 km s^{-1} in which ^{12}CO was detected.

Due to the large area covered by the observations, and the fact that the calculations were done channel by channel, the ideal way to display the results of the calculations was in map form, hence the FITS files output. These output files were made only for optical depth, excitation temperature, and ^{12}CO column density. Each file contains the coordinate offsets for the position of concern, and an ASCII list of the values for each channel. The conversion program TOSPECX, written by D. Lane, was used. These FITS files were then read into SPECX using specially written scripts, and maps were created. The purpose of these maps was to obtain a qualitative view of the relative changes of the various quantities over the region observed. With this in mind, the extreme noise spikes were edited out of individual spectra (see Figure 39 for an example). The offending channel value was replaced by an average of its neighbours. This method was used consistently for every spectrum of every quantity as required. The easiest way to replace the

problematic channel value was to alter the original output file from the program PARAM.C, recreate the FITS file, and overwrite the initial spectrum in the map.

As a consistency check the excitation temperatures were calculated for selected positions using different line ratios. The ^{12}CO J = 2 → 1 and ^{12}CO J = 3 → 2 line ratio was used as a check for the calculations in the outer ^{12}CO wings. As a check for the inner region, the $^{12}C^{18}O$ J = 3 → 2 and ^{13}CO J = 3 → 2 line ratio was used. The results of all calculations are presented in the next section.
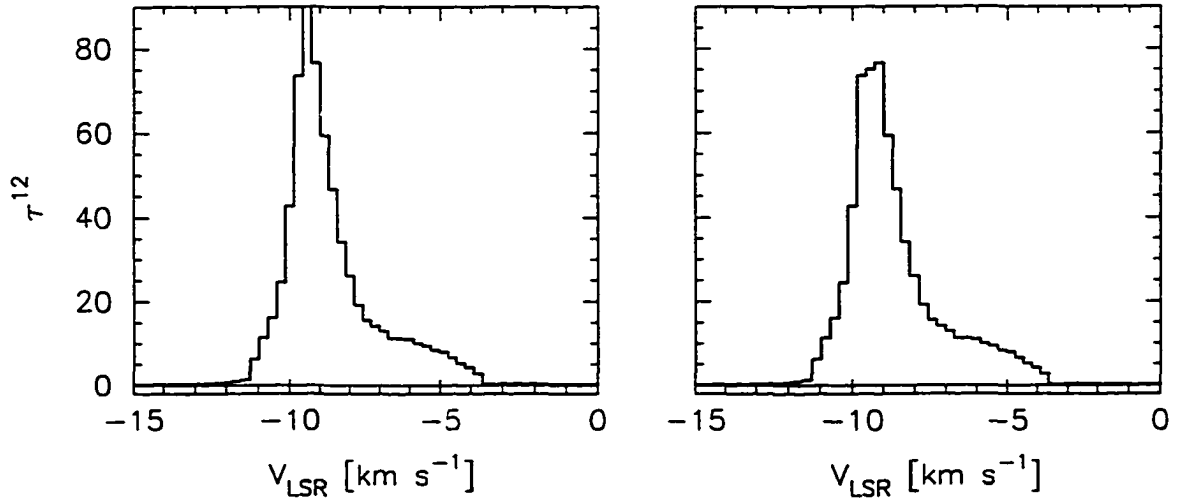
Figure 39. Example ^{12}CO Optical Depths. The graph on the left is the original, and contains a noise spike at -9.3 km s^{-1}. The edited graph, used to create the FITS file, is shown on the right.

5.2 Procedure for FIRS Bipolar Outflow and the Region Near GGD 32/HH 103

As with the LkHα 234 outflow region, it was of interest to know the total mass, momentum, and kinetic energy contained within the redshifted outflow from the FIRS, and within the blueshifted molecular gas associated with GGD 32. The equations for optical depth, excitation temperature, and column density given in §4.1 and §4.2 were applied in the velocity intervals containing a ^{13}CO line. In the velocity intervals where no ^{13}CO J = 3 → 2 line existed and those cells where no ^{13}CO J = 3 → 2 line was detected at all the gas was assumed to be optically thin and the ^{12}CO J = 3 → 2 to J = 2 → 1 ratio was used to calculate excitation temperatures and column densities.

In order to calculate the desired quantities for each region, the problem of differing grid sizes had to be resolved. Recall that the ^{13}CO J = 3 → 2 grid spacing was 10″ x 10″, the ^{12}CO J = 3 → 2 grid spacing was 4″ x 8″, and the ^{12}CO J = 2 → 1 grid spacing was 30″ x 30″. Since the ^{12}CO J = 3 → 2 grid spacing was the smallest, these spectra were averaged to produce two separate sets of ^{12}CO J = 3 → 2 averaged spectra: one with a grid spacing of 10″ x 10″ to be associated with the ^{13}CO spectra, and one with a grid spacing of 30″ x 30″ to be associated with the ^{12}CO J = 2 → 1 spectra. To obtain the 10″ x 10″ set, the ^{12}CO J = 3 → 2 spectra within a given 15″ ^{13}CO J = 3 → 2 beam were averaged. To obtain the 30″ x 30″ set of ^{12}CO J = 3 → 2 spectra, all spectra within 20″ of the centre of a given ^{12}CO J = 2 → 1 observation point were averaged. Both sets of averaged ^{12}CO J = 3 → 2 spectra are then averages over the beams of either the ^{13}CO J = 3 → 2 or ^{12}CO J = 2 → 1 spectra. The two sets of spectra with 10″ x 10″ spacing were used in velocity intervals where the ^{13}CO J = 3 → 2 line was detected, and the two sets of spectra with 30″ x 30″ spacing were used for velocity intervals and positions where no ^{13}CO line was detected.

For each spectrum in the 10″ x 10″ data sets, the relevant wing (red for the FIRS, blue for GGD 32) was split into intervals of approximately 2 km s^{-1} (the actual width depended on line shape). The corresponding spectra from the 30″ x 30″ data set were divided into corresponding intervals. For every position, average values of T_A^* were found graphically for all four spectra. In the intervals where it was

possible to use the ^{12}CO to ^{13}CO J = 3 → 2 line ratio the optical depth, excitation temperature, and

^{12}CO column density were calculated according to the equations in §4.1 and §4.2. For the portion of the

^{12}CO J = 3 → 2 wing where ^{13}CO data did not exist the excitation temperature and optical depth were

calculated from the 30″ x 30″ data set using the optically thin equations (§4.5) which require the

^{12}CO J = 3 → 2 to J = 2 → 1 ratio. Looking at the graph for excitation temperature in the Analysis section

(Figure 31) one can state that the optically thin equation for excitation temperature is approximately linear

when the T_R ratio is less than or equal to one. For these calculations, any T_R ratio for a velocity interval

which was greater than one was classified as a "non-physical" result, and discarded. The discarded values

were replaced by average excitation temperatures calculated over all accepted values produced by the

optically thin calculations.

In the intervals where both ^{12}CO and ^{13}CO from the 10″ x 10″ set were present the optical depth,

excitation temperature, and column density were calculated according to §4.1 and §4.2. In the intervals

where the ^{13}CO line was not present, and the ^{12}CO J = 3 → 2 and ^{12}CO J = 2 → 1 line from the 30″ x 30″

set were present, the optically thin assumption was made and the excitation temperature, optical depth, and

column density were again calculated according to §4.5. In some intervals, due to the different grid

spacings (oversampled as opposed to sparsely sampled) and half-power beam widths, the ^{12}CO J = 3 → 2

average calculated for the 10″ x 10″ data set extended beyond that of the ^{12}CO J = 2 → 1 spectrum. In

these particular intervals, the average optically thin excitation temperature mentioned above was used along

with the average ^{12}CO J = 3 → 2 antenna temperature from the 10″ x 10″ data set to calculate the optical

depth and ^{12}CO column density using the optically thin equations. Regardless of the method used to obtain

the excitation temperature and the ^{12}CO column density, the mass, the momentum, and the kinetic energy

were calculated as described in §4. Total values of mass, momentum, and kinetic energy for the high

velocity gas near GGD 32/HH 103 and the red lobe of the FIRS were calculated for the appropriate wing.

In order to extrapolate the above values to the entire region of concern an estimated size of the

region was required. For each of GGD 32 and the red lobe of the FIRS an estimate of the size, in terms

of beam areas, was found using planimetry. The total mass, momentum, and kinetic energy of the observed

regions were then corrected by a factor equal to the ratio of the number of beam areas in the entire flow to the number of beam areas actually covered by the observations. The number of beam areas covered by the observations was not strictly the number of observation points because of half-beam spacing. A small correction was applied to the number of observation points to account for the overlapping beam areas.

For the FIRS redshifted outflow, the wing was defined as velocities redward of -9.5 km s^{-1} to the end of the red wing of the ^{12}CO J = 3 → 2 (10″ x 10″) spectrum. As mentioned in the Observations section, the contamination of the line centre in the ^{12}CO J = 2 → 1 data was restricted primarily to the western half of the map so it is not a concern here. The number of beam areas observed, corrected for overlap, was approximately 15.1. The area of the outflow was chosen to be the area within the 2.00 K km s^{-1} contour in the velocity range -7.00 to -6.00 km s^{-1}. The velocity range was chosen to maximize the size of the red lobe. The number of beam areas observed covers 71% of the estimated total redshifted outflow area (from planimetry).

Similarly, for the blueshifted molecular fragment, the wing was defined as velocities blueward of -12.0 km s^{-1} to the end of the blue wing of the ^{12}CO J = 3 → 2 (10″ x 10″) spectrum. The line centre contamination here was not an issue since the velocity intervals of concern were blueshifted with respect to the contaminated velocities. The area of the fragment was chosen as the area within the 1.0 K km s^{-1} contour in the velocity range -17.0 to -16.0 km s^{-1}. Again, the velocity range was chosen to maximize the size of the blueshifted fragment. The number of beam areas observed, corrected for overlap, is approximately 17.1, which covers 63% of the estimated total blueshifted outflow area (from planimetry).

6 RESULTS FOR THE HIGH VELOCITY GAS

6.1 Outflow Associated with LkHα 234

Channel by channel calculations of the appropriate physical parameters were done for a region 150″ x 105″ in size about LkHα 234 as described in §5.2. A brief summary of the various excitation temperatures obtained throughout the region will be presented, followed by the column densities. A discussion of the appropriateness of the application of the optically thin assumption and the validity of the excitation temperatures used as input to the optically thin calculations will be given. The kinematical properties of the outflow will then be discussed, as well as the axial momentum distribution.

A grid-spectrum map of the excitation temperatures is given in Figure 40. The highest temperatures, 40 to 55 K, were found in the molecular ridge. The temperatures do not drop off dramatically to the west of the ridge, but remain high into the molecular cavity. For positions in the outflow, the excitation temperature graphs are double-peaked. The highest temperature (≈ 35 to 40 K) occur at a velocity of ≈ -8 km s^{-1}. These temperatures are about 20 K higher than the ambient temperature. There is a region, coincident with the corresponding region of ^{12}CO spectra, where there are three peaks in the excitation temperature graphs.

The ^{12}CO column density grid-spectrum is shown in Figure 41. Due to the vertical scale the extended red wings at positions in the outflow are suppressed. The molecular ridge stands out as the region where the column density graphs peak sharply at the ambient velocity. To the west of the ridge, the column densities drop off rapidly in amplitude but do not go to zero. A comparison of column density with excitation temperature indicates that the gas to the west of the ridge is hot and of low column density. There is a region $\approx 15''$ in diameter and centred at (35″, 22.5″) where there are two column density maxima. This region overlaps the region of triple-peaked ^{12}CO spectra. Further out in the outflow the graphs of
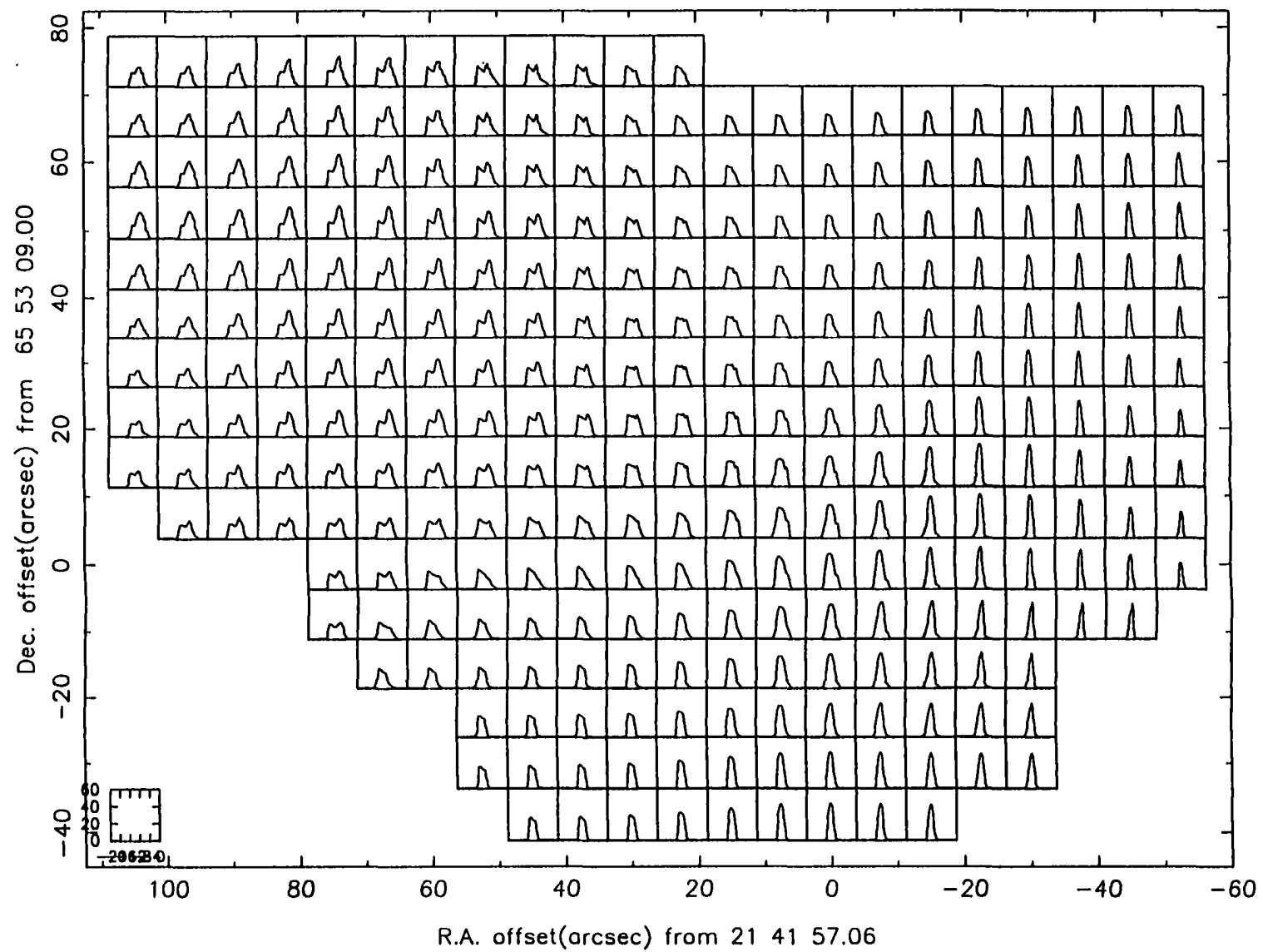
Figure 40. Grid-Spectrum of Excitation Temperature. The vertical scale of each spectrum is in Kelvins.
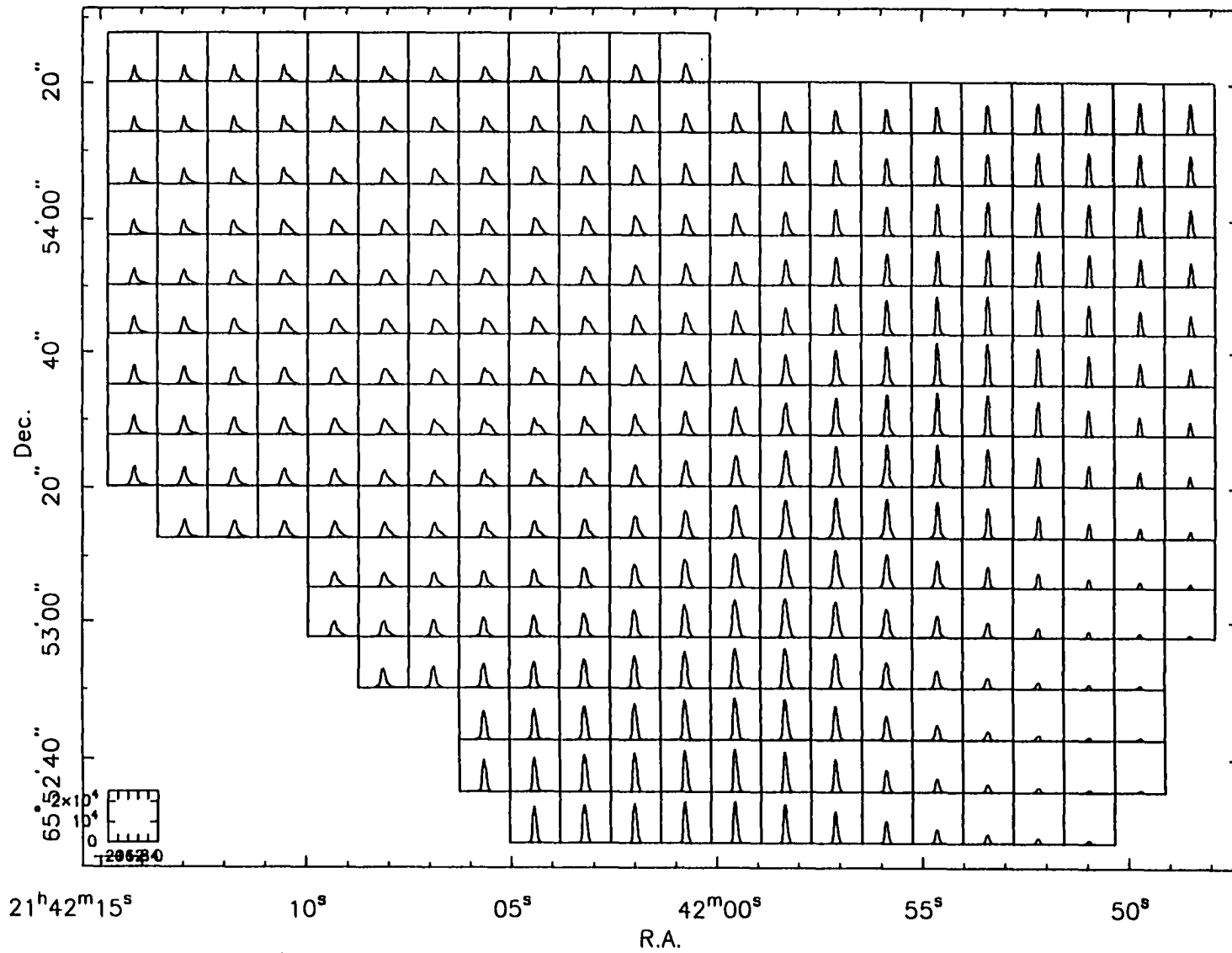
Figure 41. Grid-Spectrum of ^{12}CO Column Density. The vertical scale has been divided by a factor of 10^{13}. Thus the range is 0 to 2.5×10^{17} cm^{-2}.

column density have single peaks with extended red wings. The same gross features are seen in the ^{12}CO optical depth profiles.

Selected channel maps of column density over the velocity range -12 to -6 km s^{-1} are shown in Figure 42. At velocities blueward of the cloud velocity the most prominent feature is a peak associated with LkHα 234. There is a column density peak at (45″, 50″) present in the velocity range -17 to -12.5 km s^{-1} corresponding to the blueshifted ^{12}CO antenna temperature peak. The bridge of emission seen in integrated intensity is visible as a region of increased column density joining LkHα 234 and the peak at (45″, 50″) over the velocities -15 to -12.5 km s^{-1}. The position angle of the bridge of emission, as determined by the inner extended contours near LkHα 234, is ≈41°.

The highest column densities about the ambient velocity occur within the molecular ridge. Peak 1 is visible as part of the southern section of a larger column density enhancement. It is also an excitation temperature peak. The column density peak at ≈(-25″, 35″) corresponds to a ^{13}CO intensity peak to the north of SVS 13.

The transition from a ridge dominated gas distribution to one dominated by the outflow can be seen in column density at ≈9.3 km s^{-1}. Between -8 and -7 km s^{-1} the outflow is visible as an arc of higher optical depths. The outflow is clearly distinguished from the surrounding material in this velocity range and at all others to the red. The ^{13}CO antenna temperature peaks at (60″, 30″) and (30″, 40″) each coincide with a column density peak. As with the outflow in ^{13}CO antenna temperature, the column densities form a structure resembling that of the ^{12}CO outflow by ≈-7.5 km s^{-1}. There is a reversed "C" feature at ≈-5.5 km s^{-1} which corresponds to a feature seen in the ^{12}CO antenna temperatures. For velocities redward of -5 km s^{-1}, the outflow as seen in column density continues to follow the shape of the ^{12}CO outflow, including a peak at (90″, 52.5″). At ≈0 km s^{-1}, the "inner outflow" discussed by Mitchell & Matthews (1994) is seen at a position angle of ≈65° (or 245°) which roughly corresponds to the optical jet axis found by Ray et al. (1990). By ≈+6 km s^{-1} the only emission is at (0″, 0″), representing the broad ^{12}CO wings of the spectra about LkHα 234.
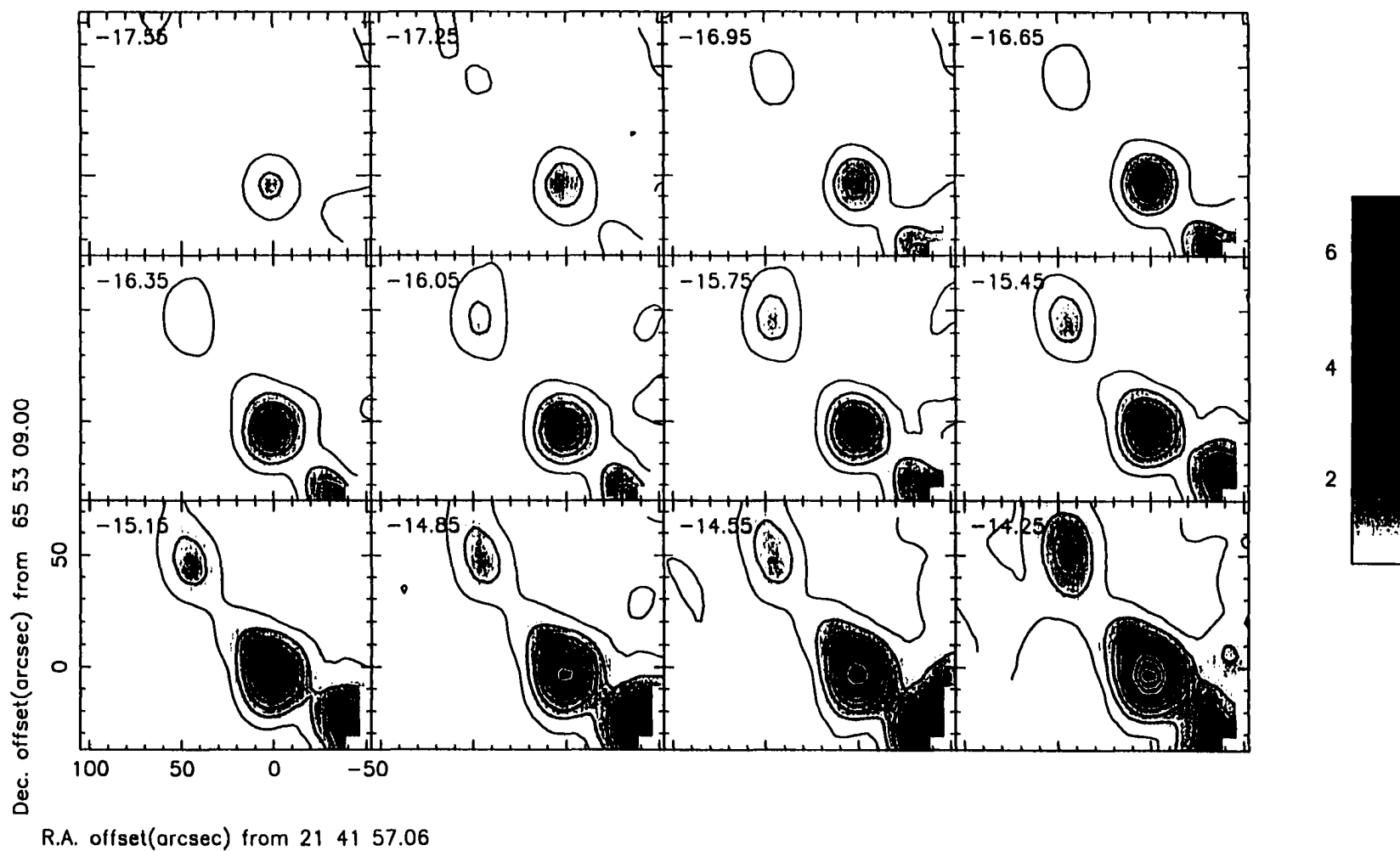
Figure 42. ^{12}CO Column Density Channel Maps. a) The velocity range is -17.7 to -14.0 km s^{-1}. The contour base level and intervals are 0.5 K km s^{-1}.
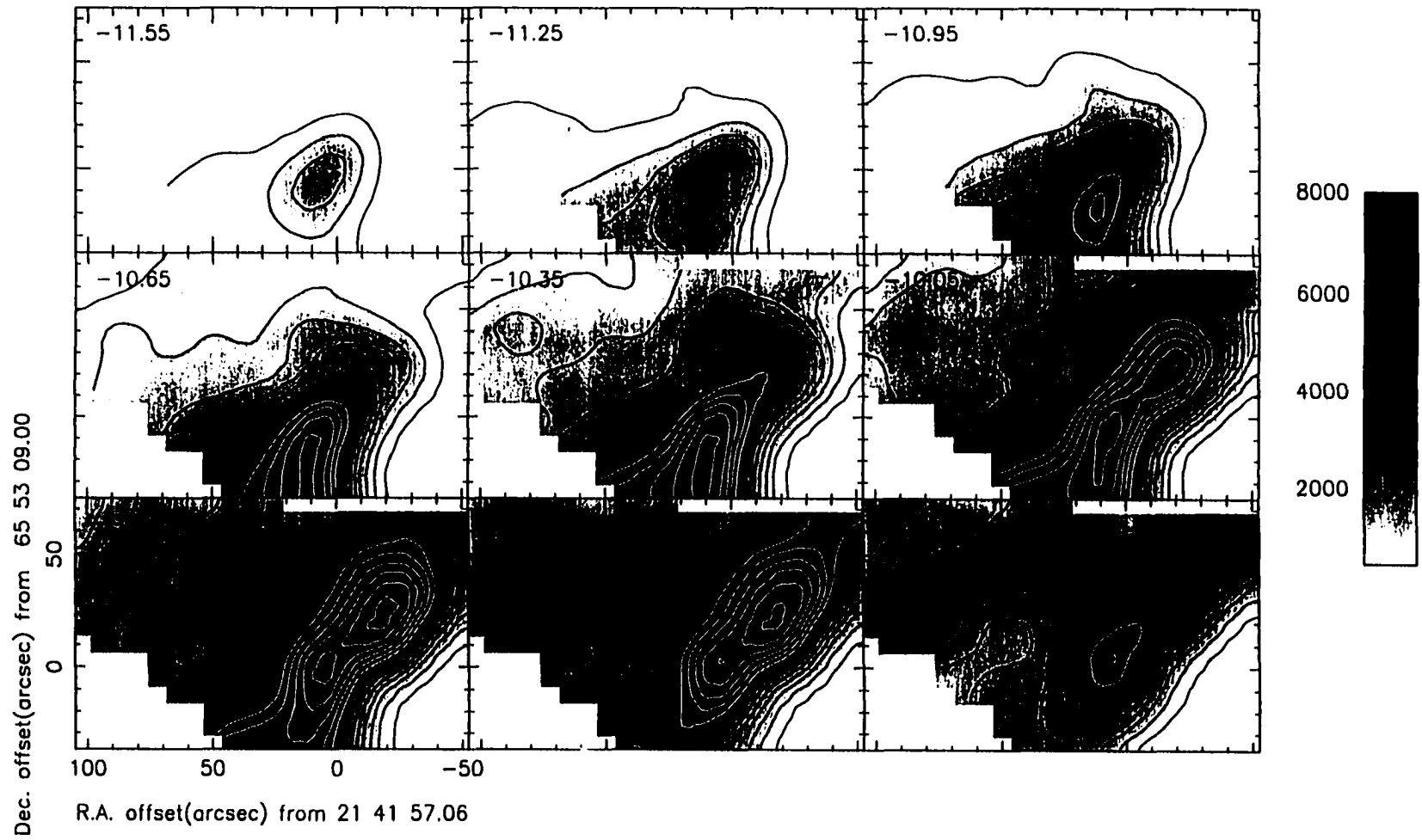
Figure 42 (continued). b) The velocity range is -11.7 to -8.9 km s⁻¹. The contour base level and intervals are 500 K km s⁻¹.
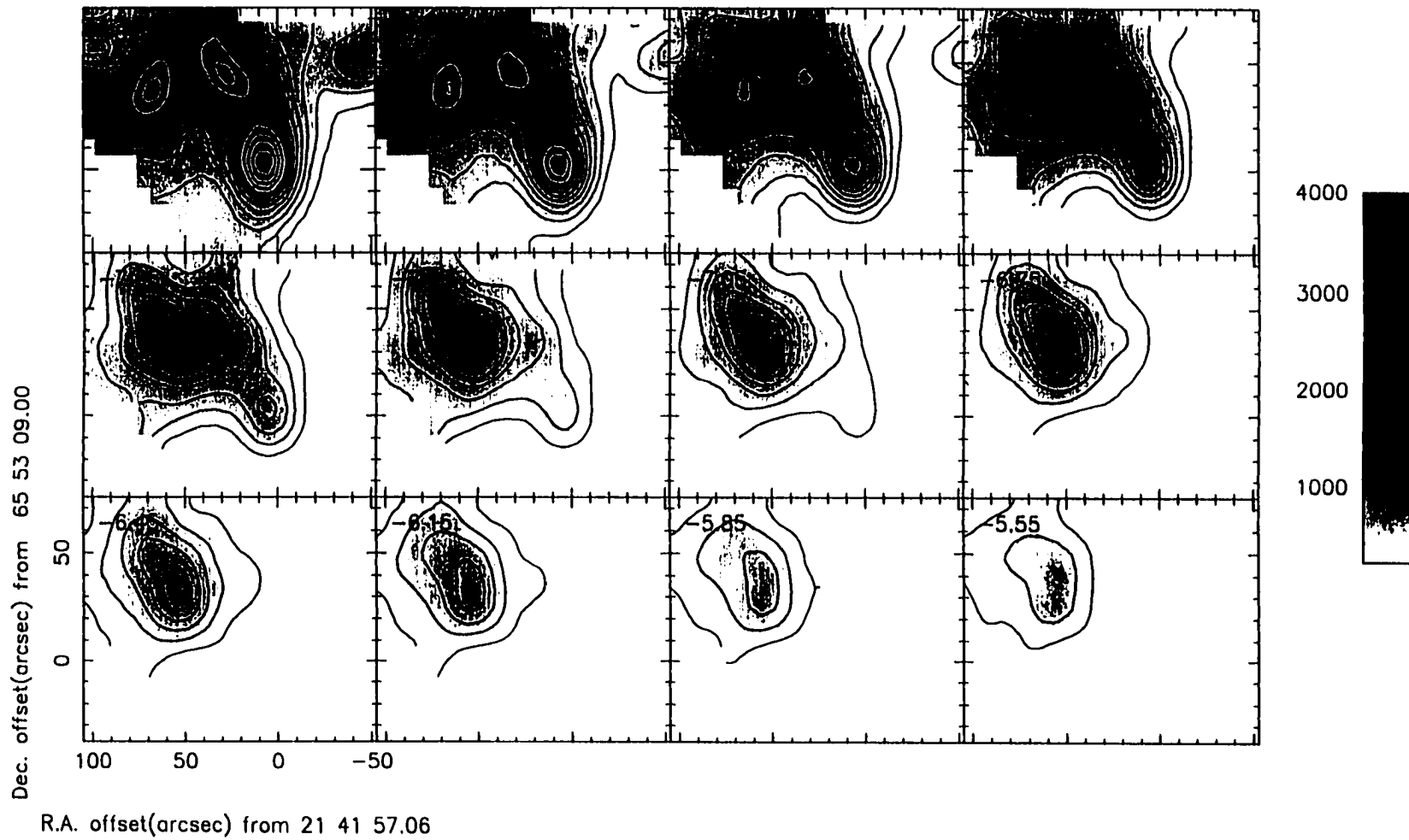
Figure 42 (continued). c) The velocity range is -9.0 to -5.3 km s⁻¹. The contour base level and intervals are 250 K km s⁻¹.
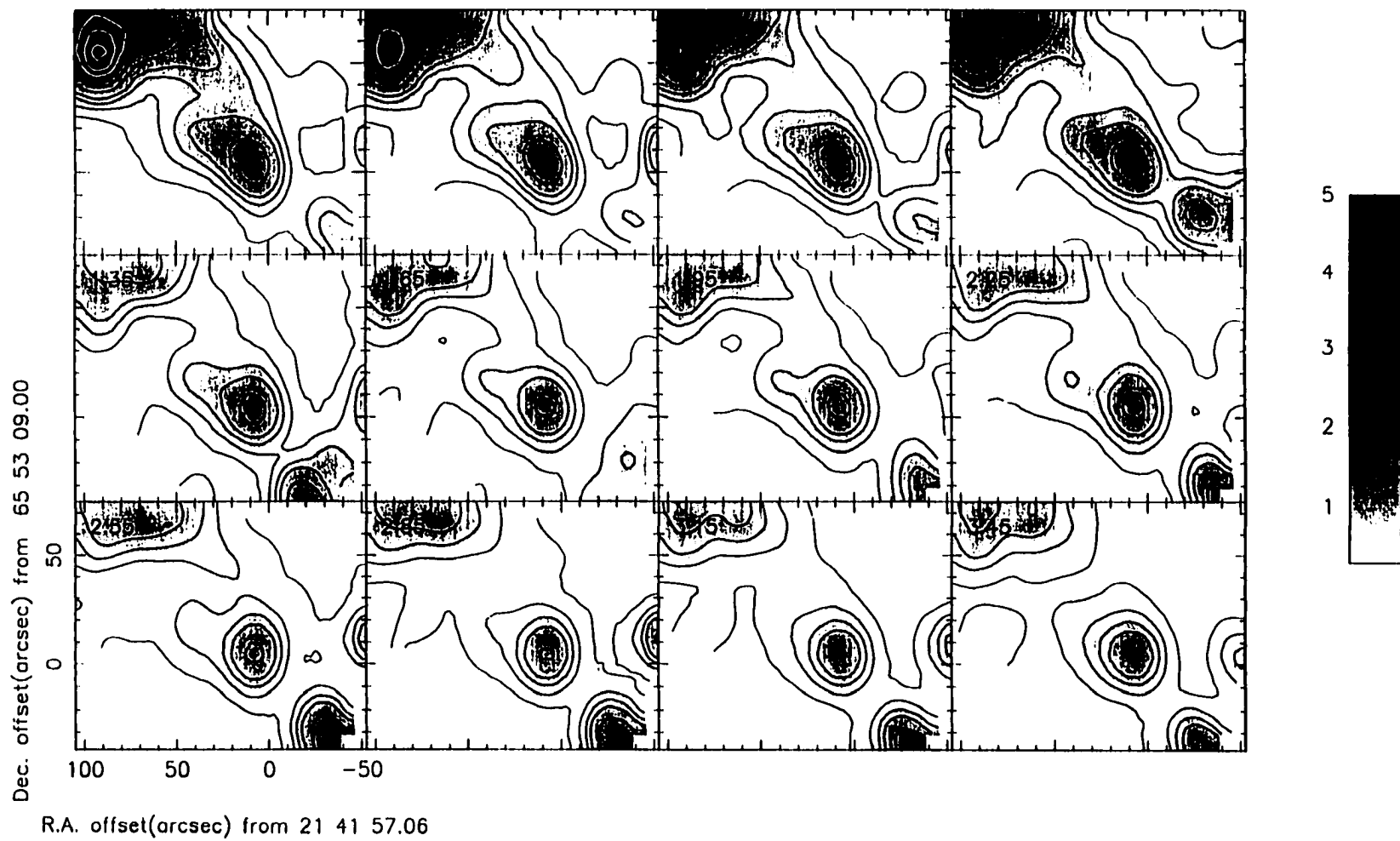
Figure 42 (continued). d) The velocity range is 0.0 to 3.7 km s^{-1}. The contours increase in steps of 0.25 K km s^{-1} from 0.25 to 1.0, then increase in steps of 0.5 up to 5.0 K km s^{-1}.

Two different sets of equations were used to calculate the column densities, as outlined in §4. The transition to the optically thin method should be examined to see if the optically thin assumption was valid. Representative graphs of optical depth from LkHα 234, the outflow and the ridge are given in Figure 43. The maxima have been clipped in order to emphasize the extended wings. The arrows indicate the end channels for the particular observation point. Figures 43 (a), (b), (c), and (e) are from positions in the outflow. The graph from the position of LkHα 234 is shown in (d). The optical depths from a position within the molecular ridge is given in (f). In general, the optically thin blue wing optical depths are systematically lower than those obtained in the blue wing from the ^{12}CO to ^{13}CO line ratio. The analogous situation sometimes occurs in the red wing. Across end channels, when one considers standard deviations of neighbouring velocity channels, the transitions are usually smooth in the sense that adjacent error bars overlap. The exception is the graph from the ridge, (f), where the transition is not smooth in either wing. The optically thin assumption in the wings of the ^{12}CO spectra may be valid for all positions outside of the molecular ridge.

The validity of the input excitation temperatures for the ^{12}CO wings must be examined as well. The input excitation temperatures were compared to those derived from the optically thin method using the ^{12}CO J = 3 → 2 to J = 2 → 1 ratio. Since the J = 2 → 1 data is sparsely sampled the input J = 3 → 2 excitation temperatures used in the comparison were nine-point averages about the centres of the J = 2 → 1 beam. The optically thin excitation temperatures found for the blue and red wings were usually in statistical agreement with the input excitation temperatures calculated from the ^{12}CO to ^{13}CO ratio. For example, the input red and blue wing excitation temperatures for the position (60″, 30″) are (16 ± 3) K and (17 ± 2) K respectively. The optically thin method at -5 km s^{-1} and -12.5 km s^{-1} give red and blue wing excitation temperatures of (26 ± 10) and (15 ± 11) K. Both optically thin values are in agreement with their respective input excitation temperatures. In the few cases where the two temperatures did not agree the optically thin excitation temperature was the lower value. In the one position where ^{12}C^{18}O J = 3 → 2 was detected, (52.5″, 37.5″), an excitation temperature of (14.4 ± 0.8) K was calculated from the ^{13}CO to ^{12}C^{18}O ratio which is in agreement with the input red excitation temperature of (18.4 ± 6.0) K.

.
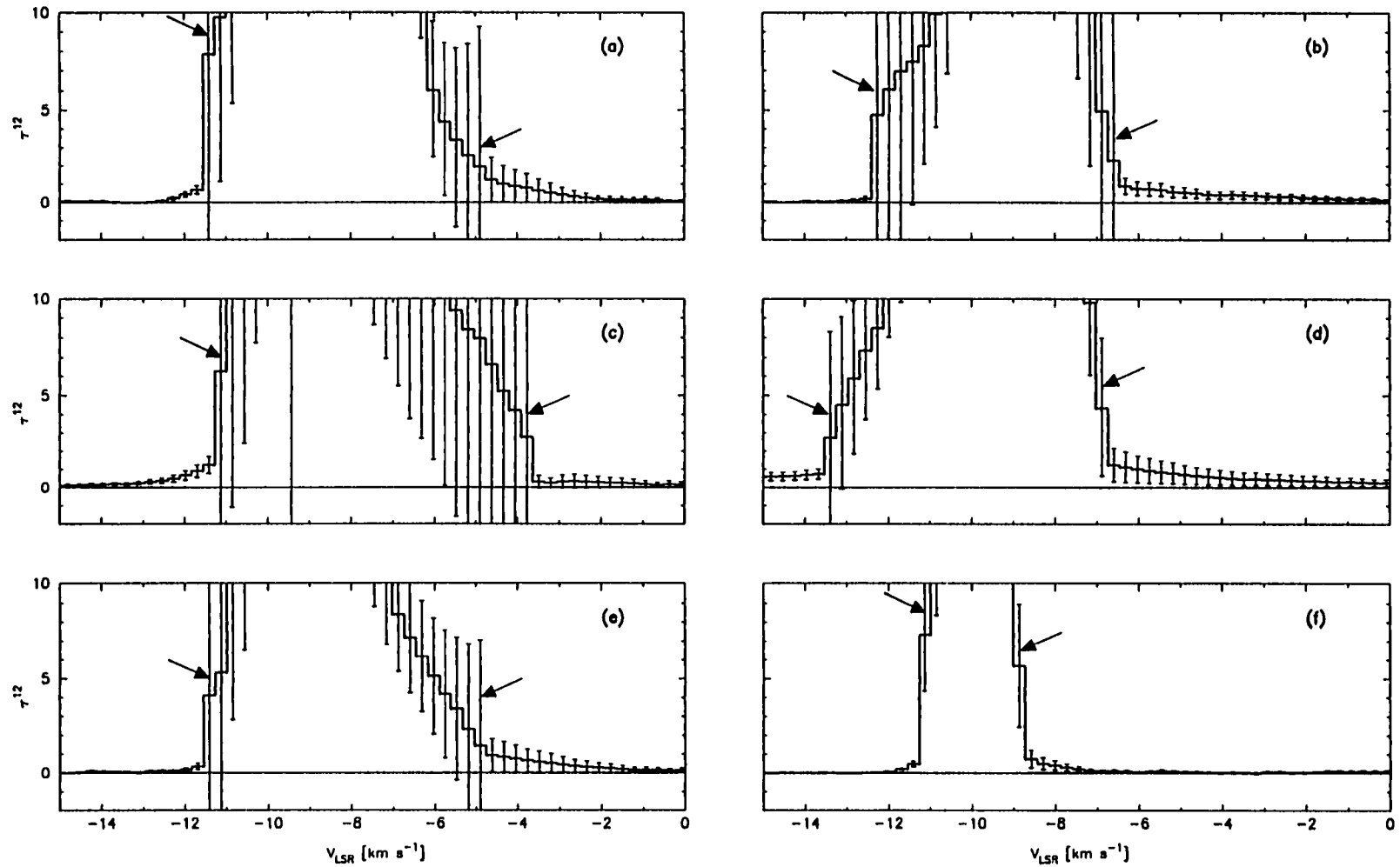
Figure 43. Sample Optical Depth Graphs. The maxima have been clipped in order to emphasize the wings. The graphs are from the offsets (a) (60″, 30″), (b) (30″, 45″), (c) (97.5″, 37.5″), (d) (0″, 0″), (e) (75″, 60″), and (f) (-22.5″, 22.5″). Standard deviations are shown, and arrows indicate end channels.

The mass, momentum, and kinetic energy of the blue, the inner red, and the outer red wings of the outflow, as defined in Figure 37, are shown in Table 7. There are two things that need to be kept in mind when considering these results. The optically thin method tends to underestimate the column density, so the blue wing and outer red wing values are most likely lower limits to the actual values (Lada 1985). Secondly, it is not known how much low velocity moving gas is masked by ambient gas, particularly in the inner red wing, which will lead to an underestimate of the wing values in the outflow as well (Lada 1985). The bulk of the mass is found in the inner red wing. The outer red wing has about half the mass of the inner red wing. Most of the momentum and kinetic energy, on the other hand, are in the outer red wing due to the high velocity gas. The momenta and kinetic energies of the blue and inner red wings are approximately equal. The kinetic energy in the entire red wing is ≈ 6 times that of the blue wing.

Table 7. The Mass, Momentum, and Kinetic Energy of the Redshifted Outflow Associated With LkHα 234. Errors are given in parentheses.

WING	MASS [$M_\odot$]	MOMENTUM [$M_\odot$ km s^{-1}]	KINETIC ENERGY [$\times 10^{44}$ ergs]
Blue Wing (blueward of -10.5 km s^{-1})	34 (3)	38 (9)	6 (3)
Inner Red Wing (-9.5 to -8.0 km s^{-1})	43 (1)	48 (1)	6 (0.1)
Outer Red Wing (redward of -8.0 km s^{-1})	26 (1)	84 (4)	31 (2)

The mass, momentum, and kinetic energies in 1 km s^{-1} intervals about the V_{LSR} are shown in

Table 8. It is seen that for the first interval (-1 to -2 km s^{-1}) the mass in both the red and the blue wings

is comparable. For all other intervals the mass in the blue wing is much less than that in the red wing.

The momentum and the kinetic energy for the first blue interval are respectively one half and one third that

of the red. Beyond the first velocity interval the momentum and kinetic energy in the blue is very much

less than the corresponding values in the red.

Table 8. A Comparison of Red and Blue Wing Gas in the Outflow Associated With LkHα 234. The total masses, m, (in $M_\odot$), momenta, p, (in $M_\odot$ km s^{-1}), and kinetic energies, E_k, (in ergs × 10^{44}) in 1 km s^{-1} intervals on either side of the V_{LSR} are given.

BLUESHIFTED		REDSHIFTED	
Velocity Interval (with respect to the V_{LSR}) [km s^{-1}]	Integrated Values	Integrated Values	Velocity Interval (with respect to the V_{LSR}) [km s^{-1}]
-1 to -2	m = 11 p = 15 E_k = 2.2	m = 19 p = 34 E_k = 6.1	1 to 2
-3 to -2	m = 2.9 p = 7.3 E_k = 1.8	m = 13 p = 36 E_k = 10	2 to 3
-4 to -3	m = 0.28 p = 0.98 E_k = 0.34	m = 4.4 p = 17 E_k = 6.7	3 to 4
-5 to -4	m = 0.02 p = 0.07 E_k = 0.03	m = 2.7 p = 13 E_k = 6.3	4 to 5
-6 to -5	m = 0.01 p = 0.04 E_k = 0.02	m = 0.71 p = 4.2 E_k = 2.5	5 to 6

As described above, the blueshifted feature seen in the ^{12}CO antenna temperature maps appears to be a column density enhancement. The total mass, momentum, and column density in the velocity range -16 to -12 km s^{-1} were found for this feature. The area covered by the feature can be seen over the velocity range -15 to -14 km s^{-1} in the column density channel maps (Figure 42). The totals for the mass, momentum, and kinetic energy are 1.2 M$_o$, 3.2 M$_o$ km s^{-1}, and 3.5x10^{43} ergs. In comparison, the values for the outer red wing in this region were calculated to be 9.8 M$_o$, 33.3 M$_o$ km s^{-1}, and 1.2x10^{45} ergs. The mass, momentum, and kinetic energy for the blue wing are lower than the outer red wing by factors of approximately 2, 10, and 35 respectively. Compared to the outer red wing the blueshifted feature is very weak, although a kinetic energy on the order of 10^{43} ergs is within the range of observed kinetic energies for other outflows (Fukui *et al.* 1993).

Following the analysis of Chernin & Masson (1995) the momentum distribution along the axis of the outflow has been determined. The axis was chosen as the line connecting LkHα 234 with the ^{12}CO antenna temperature peak at (90″, 52.5″) which lies along a position angle of ≈60°. The momentum was binned in slices 21″ wide, corresponding to the one beamwidth slices of Chernin & Masson (1995). The first slice is centred on LkHα 234. The momentum distribution is presented in Figure 44. The peak of the distribution occurs at a distance of 63″, or ≈0.3 pc, from LkHα 234. The momentum distribution, and its implications, will be further discussed in §7.2.

6.2 FIRS Bipolar Outflow and Region Near GGD 32/HH 103

The results of the analyses for the moving gas near GGD 32/HH 103 and for the red lobe of the FIRS are summarized in this section. For each region, the average excitation temperature will be presented. The general characteristics of the optical depths will be given, as well as a discussion of the appropriateness of the optically thin assumption. Estimates of the kinematical properties of the red lobe of the FIRS and of the high velocity blueshifted gas near GGD 32/HH 103 will be discussed.
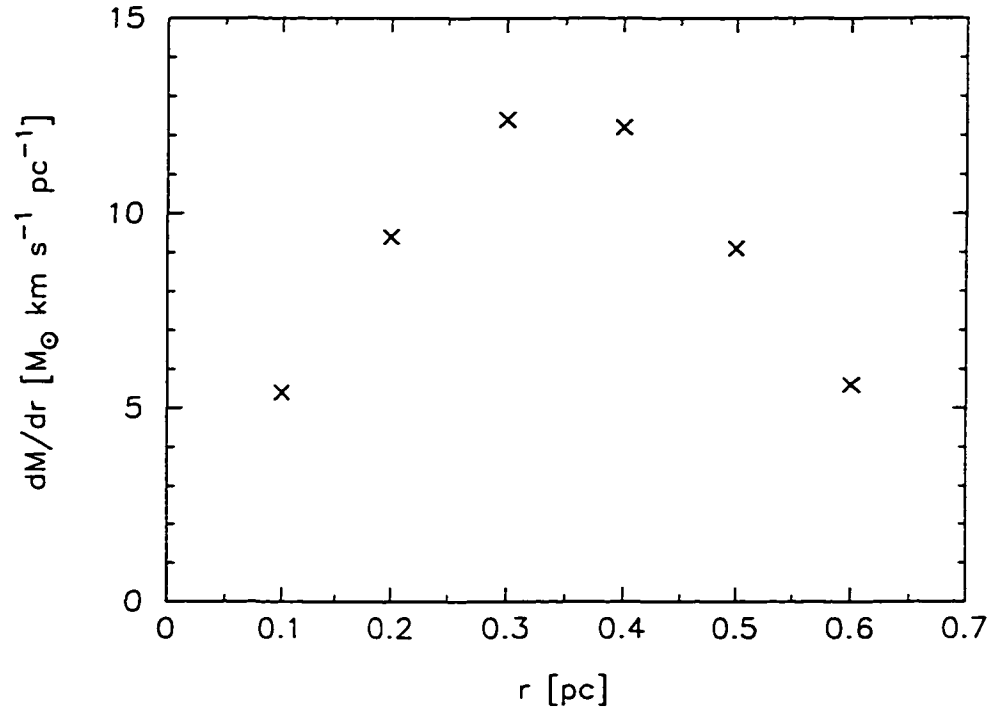
Figure 44. Axial Momentum Distribution for LkHα 234. The axis of the outflow was taken to be along the position angle of 60° to match that of Chernin & Masson (1995).

For the red lobe of the FIRS an average excitation temperature of (14 ± 1) K was found from the acceptable optically thin values (see §4.3). This value is in statistical agreement with the average excitation temperature calculated from the ^{12}CO to ^{13}CO line ratios. At velocities near the line centre, the gas was found to be optically thick, with $\tau^{12} \geq 10$. Near the outer limits of the wings (≈ 0 km s^{-1}) the gas is optically thin. The transition to the optically thin regime at every position is not smooth, a drop of one to two orders of magnitude being seen at the turnover to the optically thin method. It is most likely that the optically thin approximation is not valid for this region. The source is not visible in the optical ($A_v = 45$ mag (Eiroa *et al.* 1998)) implying high optical depths. As a result, the inner wings where ^{13}CO was detected dominate in their contribution to the sums of mass, momentum, and kinetic energy. Optical depths of approximately (30 ± 1) and (19 ± 1) were found at the inner and outer ^{12}CO emission peaks. The mass, momentum, and kinetic energy for the red lobe of the FIRS is given in Table 9.

For the region near GGD 32/HH 103 the average excitation temperature which was used, (16 ± 1) K, was calculated from the acceptable optically thin values. The average excitation temperature calculated from the ^{12}CO to ^{13}CO line ratio does agree with the optically thin average. At positions where no ^{13}CO was detected the optical depths near the line centres are approximately equal to unity. Where ^{13}CO was detected, the optical depths at velocities near the line centres are in the range $2 < \tau^{12} < 15$. Blueward of ≈ -17 km s^{-1} the lines are optically thin. Again, the transition to the optically thin wing is not smooth, but it is also not as drastic as in the red lobe of the FIRS. Generally, at the transition to the optically thin assumption the value of the optical depth dropped by factors of 30 to 60. In this region this jump may be the result of a poor signal-to-noise ratio for the ^{13}CO spectra, as opposed to the FIRS where it is most likely an optical depth effect. As with the FIRS, the inner wings where ^{13}CO was detected make the greatest contribution to the sums of mass, momentum, and kinetic energy. The maximum optical depth of (15 ± 2) was found to correspond to one of the ^{12}CO emission peaks. The mass, momentum, and kinetic energy for the blueshifted gas are given in Table 9.

Table 9. Kinematical Quantities for Objects in NGC 7129 South. The mass, momentum, and kinetic energy of the red lobe of the FIRS and for the high velocity blueshifted gas near GGD 32/HH 103. Errors are given in parentheses.

OBJECT	MASS $[M_\odot]$	MOMENTUM $[M_\odot$ km s$^{-1}]$	KINETIC ENERGY $[\times 10^{44}$ ergs]
Molecular Fragment (blueward of -12 km s^{-1})	1.72 (0.01)	5.87 (0.04)	2.20 (0.01)
FIRS (red lobe) (redward of -9.5 km s^{-1})	6.8 (0.1)	8.76 (0.01)	1.68 (0.01)

7 DISCUSSION

7.1 Quiescent Gas in NGC 7129

The idea that triggered star formation has occurred in NGC 7129 was first suggested by Bechis *et al.* (1978). On the basis of their CO observations, and the presence of a reddening gradient in the region which decreases from the east to the west, they argued for the existence of a low-density bubble on the near side of the molecular cloud. The analysis by Bechis *et al.* (1978) determined that BD +65 1638, the oldest and most westerly bright star, may have been responsible for the evacuation of the cavity. Of the two bright stars whose spectral types have been determined, the older star (BD +65 1637) is closer to BD +65 1638 than the younger (LkHα 234). The stellar winds of BD +65 1638, interacting with ambient material to the east of the star, may have triggered the formation of the stars BD +65 1637, LkHα 234, and SVS 13. In this way NGC 7129 is similar to the BD +40° 4124 region which is considered to be an example of small scale triggered star formation (Hillenbrand *et al.* 1995). Bechis *et al.* (1978) also proposed that the FIRS was a result of triggered star formation. New observations, such as the detection of a deeply embedded cluster of stars within 20″ of LkHα 234 (Cabrit *et al.* 1997), the determination that emission in the IR filament is due to fluorescence (Noriega-Crespo *et al.* 1997), and the data presented in this thesis, provide further evidence for the triggered star formation scenario.

The new ^{12}CO and ^{13}CO maps of NGC 7129 provide greater insight into the structure of the molecular cavity in the region, and the gas surrounding it. The eastern section of the molecular ridge, at velocities slightly blue of the quiescent velocity, is located to the southeast of its ambient position, whereas the western section is stationary. This indicates that the cavity is more open on the eastern side than the western, which may be due to the influence of the eastern stars. Both the FIRS and the exciting source for the reflection nebula RNO 138, RNO 138S, may be embedded within the extended ridge. Another pre-main sequence star in the region, SVS 6, lies to the northeast of RNO 138. The correlation between the positions

of the pre-main sequence stars and of the ridge provides further evidence that triggered star formation has occurred in NGC 7129.

Information about structure within the molecular ridge is now available due to the high resolution of the new observations. At least nine intensity peaks, distributed around the cavity, are present in the ridge as shown in Figure 9. The ^{12}CO intensity peaks on the western edge of the molecular cavity are located within elongated, filamentary structures in the ridge. At least one of these peaks is an actual density enhancement, as shown by the ^{13}CO line strengths. The ^{13}CO observation points (see Figure 7) are plotted on a greyscale image of the western region of the ridge in Figure 45. As indicated in the figure, the positions where ^{13}CO was detected is correlated with the position of the intensity peak to the north of GGD 32, and with the western segment of the ridge. The western intensity peaks, then, are likely to be actual clumps.

Additionally, the detailed analysis performed on the data from the region surrounding LkHα 234 included three of the intensity peaks in the ridge: one at the position of LkHα 234, and two to the northeast of the star. This analysis proved that those intensity peaks are in fact column density enhancements. Thus, the ^{13}CO intensity peaks observed in the molecular ridge on the eastern edge of the cavity are most likely clumps as well.

There is evidence that the process of triggered star formation may be an ongoing process in NGC 7129. Both SVS 13 and BD +65 1637 may currently be influencing the eastern section of the molecular ridge. As was shown in Figure 10, SVS 13 is ≈10″ west of one of the clumps (Peak 1). The apex of an H_2 emission arc (Cabrit et al. 1997), which may be centred on SVS 13, is coincident with an indentation of the ^{13}CO contours in the ridge. This suggests that SVS 13 may be compressing Peak 1. Further evidence is that the extended ^{13}CO clump at (-45″, -90″) is approximately 40″ due south of the star BD +65 1637. The flux calculated by Bechis et al. (1978) showed that BD +65 1637 was capable of producing such compressive effects on the environment. In summary, the presence of clumps distributed throughout the ridge, together with the compressive effects of SVS 13 and BD +65 1637, suggest that triggered star formation will continue in NGC 7129.
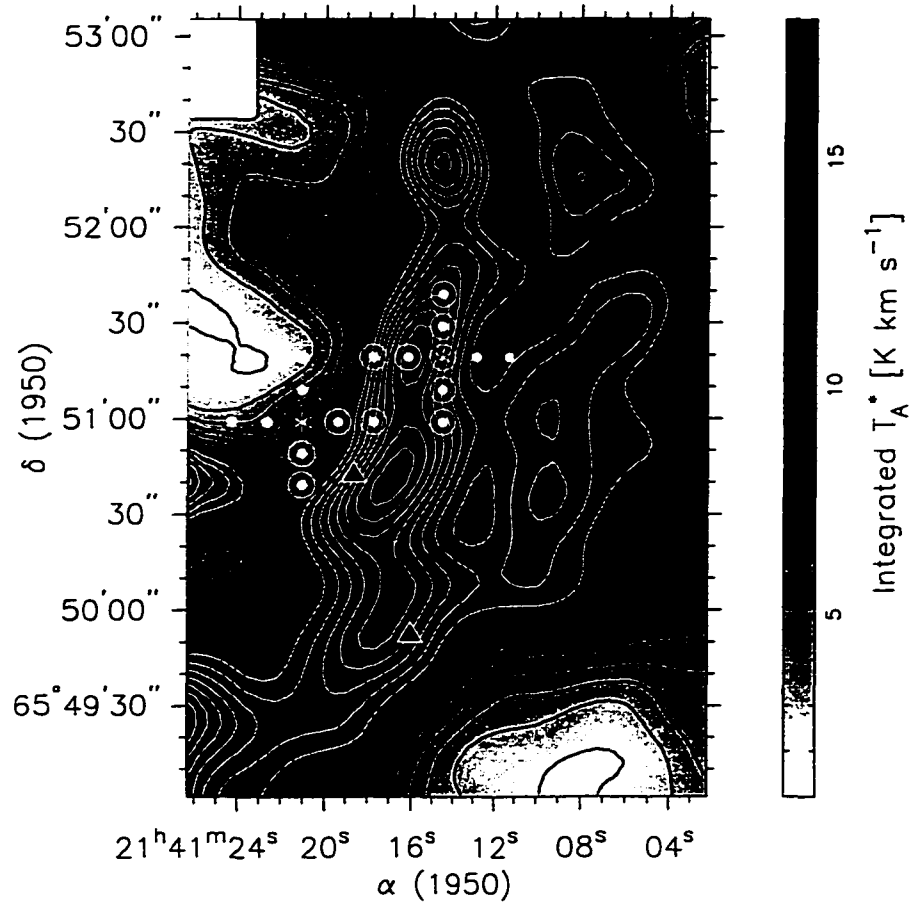
Figure 45. ^{13}CO J = 3 → 2 in the Western Molecular Ridge. The ^{13}CO points of observation are superimposed on a greyscale map of ^{12}CO J = 3 → 2 integrated intensity. The greyscale and contours are the same as for Figure 7.

7.2 LkHα 234 and the Redshifted Outflow

In §6.1 the total masses, momenta, and kinetic energies for the blue wing, and the inner and outer red wings were given. Considering the total masses alone, the inner red wing is dominant. The momenta and kinetic energies of the blue wing and the inner red wing are approximately equal. The outer red wing has almost twice the momentum of the inner red wing, and approximately five times the kinetic energy.

The results of the kinematical analysis performed in this paper are given in Table 10 along with previously published values. The values determined here are all approximately equal to those of Edwards & Snell (1983). However, the calculations by Edwards & Snell (1983) were based on data that had a large beamwidth (HPBW = 50″) and that was sparsely sampled. The only transition available to these authors was ^{12}CO J = 1 → 0 so they were required to assume that all of the gas was optically thin. While the optically thin assumption is valid for part of the ^{12}CO wings (redward of ≈-4 km s^{-1}), it would underestimate the column density at velocities close to -8 km s^{-1}. Their values were calculated over the velocity interval -8 to 0 km s^{-1}, rather than the farthest extent of the ^{12}CO wing. The momentum and kinetic energy quoted by Edwards & Snell (1983) are for the sum of the red and blue wings. Summing the totals for the blue and outer red wings found by the analysis given in this thesis, the total momentum and kinetic energy are (122 ± 10) M$_\odot$ km s^{-1} and (3.7 ± 0.4) x 10^{45} ergs respectively. In comparison, the momentum calculated by Edwards & Snell (1983) would be about two thirds the value found here, but the kinetic energy would be approximately equal. It should be noted that Edwards & Snell (1983) did not take into account a projection effect in their calculations. If a projection effect of 20° was applied to their values it would increase them by ≈14%. This would have a minimal effect on the agreement with the results determined in this paper.

All three quantities derived by the method outlined in §5 are about one third of those calculated by Mitchell & Matthews (1994). This discrepancy is most likely due to the different methods of calculation. Mitchell & Matthews (1994) extrapolated the values of optical depth from the position (37.5″, 30″) to the entire outflow. With this assumption, it is evident that all optical depths redward of -7 km s^{-1} were

overestimated in comparison to the values calculated in this work. This would lead to an overestimate of all kinematical values. An excitation temperature of 10 K had been assumed which, in light of the analysis in this paper, is probably ≈5 to 10 K too low. In this paper complete overlapping fully-sampled ^{12}CO and ^{13}CO J = 3 → 2 data sets were used. The calculations were done channel-by-channel over the region defined in Figure 37, employing the optically thin assumption for channels where no ^{13}CO was detected. No extrapolation to the total area observed was made unlike in Mitchell & Matthews (1994).

Table 10. Results From This and Former Analyses for the Redshifted Outflow Associated With LkHα 234. The mass, momentum, and kinetic energy obtained in this thesis, as well as previously published values, for the redshifted outflow associated with LkHα 234. Sources: 1) this paper; 2) Mitchell & Matthews (1994); 3) Edwards & Snell (1983). The errors are given in parentheses.

Source	Velocity Interval [km s^{-1}]	Mass [M$_\odot$]	Momentum [M$_\odot$ km s^{-1}]	Kinetic Energy [x10^{45} ergs]
1	-8.0 km s^{-1} to the end of the ^{12}CO spectrum	26 (1)	84 (4)	3.1 (0.2)
2	-8.0 to +8.0 km s^{-1}	68	220	9.4
3	-8.0 to 0.0 km s^{-1}	18.4*	84	3

*mass is for the red wing only

One purpose of the detailed method of analysis performed here was to determine structure within the molecular outflow. An investigation of the ^{12}CO column density channel maps presented in §5 shows that the outflow is sinuous and complex. The channel maps also prove that the outflow is clumpy; actual column density enhancements are present within the outflow. There are two prominent clumps at (60″, 30″) and (30″, 40″) in the redshifted outflow at velocities between -8 and -7 km s^{-1}, along with a clump at (90″, 52.5″) which is visible at velocities redward of -5 km s^{-1}. The outflow, at high velocities, has a well-defined opening angle of ≈25°. There may be a partial shell structure visible at the most highly redshifted

velocities (velocities > + 1 km s⁻¹). The outflow seems to break up into two regions with emission along

the position angle of the inner jet, and along a position angle of ≈50°. The two features define the "walls"

of the outflow, with a region of lower column density between them. A review of the channel maps,

however, does not provide evidence for any large-scale symmetries, such as an empty cone.

A position-velocity (p-v) plot of the redshifted molecular outflow associated with LkHα 234, as

seen in ¹²CO J = 3 → 2, is presented in Figure 46. The axis of the outflow lies along a position angle of

60°, and the integration is over the entire width of the outflow. The peak at an offset of -15″ along the axis

is related to LkHα 234. The band of emission at a V_{LSR} of -10 km s⁻¹ seen through the entire axis of the

outflow is emission at the ambient velocity. The highest velocity blueshifted emission is associated with

LkHα 234. The outflow contours fan out to redshifted velocities quickly. Beyond ≈20″ the velocity width

is essentially constant, and remains so to an offset of ≈90″ along the axis where the contours then flare

again to higher redshifted velocities. Peak redshifted velocities occur at the farthest positions from

LkHα 234. A bright feature can be seen at an offset of 90″ which corresponds to the extended ¹²CO

column density peak which has a maximum at (50″, 30″).

Theoretical p-v diagrams for an accelerated outflow model have been presented by Cabrit

& Bertout (1986). Their model assumes that the outflow is bipolar, and that both lobes are filled. For

comparison with Figure 46, a p-v plot of ¹²CO J = 2 → 1 emission produced by Cabrit & Bertout (1986)

for an outflow is given in Figure 47. The model has an inclination angle of 30°, an opening angle of 30°,

and an exponent on the radius ratio of -1 in their power-law velocity field. Although the model p-v diagram

does show some similarities to the observed p-v diagram, a number of features in the observed diagram are

absent in the theoretical one due to limitations of the model. The most noticeable difference between the

two p-v diagrams is that only the red lobe is present in the outflow associated with LkHα 234, while both

lobes are shown for the model. The emission band at the ambient velocity is absent in the model. The

modeled outflow contours do fan out in a way that is similar to that observed, but lack a region of constant

velocity width. As the model of Cabrit & Bertout (1986) did not include interactions with ambient material,

or entrainment by shocks, the bright peak in the outflow was not reproduced.

12t_map Sun Mar 22 11:27:01 1998

Velocity (km/s)

Y   offset(arcsec) from 65 53 09.00
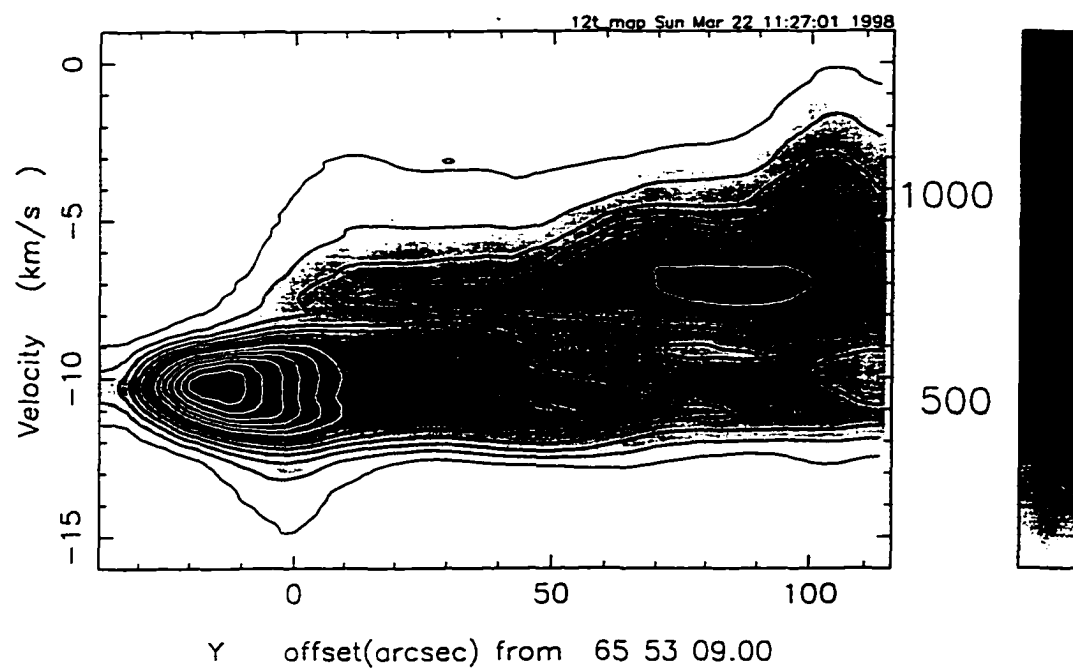
Figure 46.   [12]CO J = 3 → 2
Position-Velocity Plot for the
Redshifted Outflow Associated with
LkHα 234.

Normalized Velocity
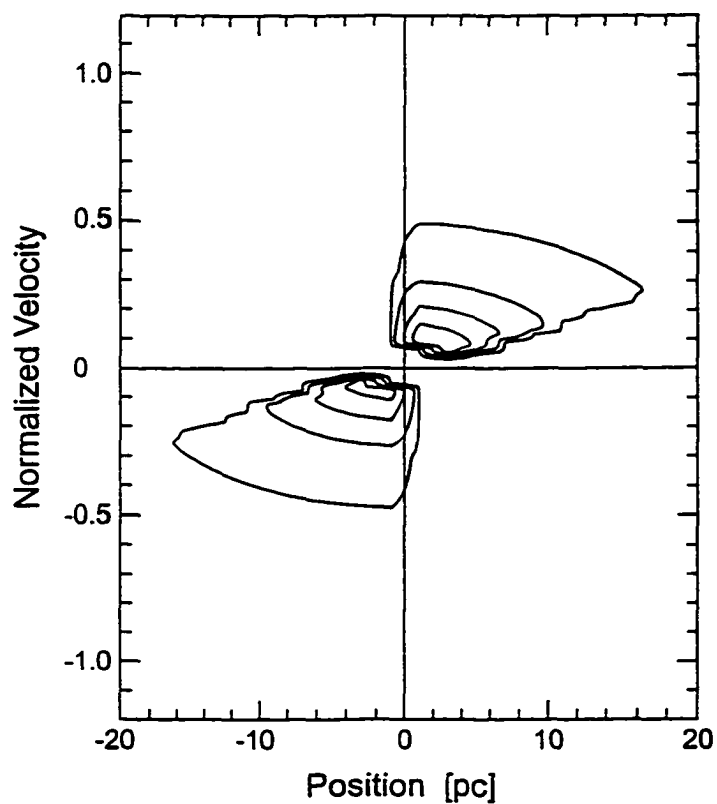
Position [pc]

Figure 47. A Theoretical Position-
Velocity Plot (Adapted from Cabrit
& Bertout 1986).

Through both theoretical models (Shu *et al.* 1991; Masson & Chernin 1992) and observations (Levreault 1988; Moriarty-Schieven & Snell 1988) it has been determined that molecular outflows are momentum driven. Chernin & Masson (1995) proposed that the axial momentum distribution may be a way to distinguish between the different outflow models (see references within Chernin & Masson (1995)): 1) the wide-angle wind, 2) the steady-state jet, and 3) the jet/bow-shock, or prompt entrainment, models. Chernin & Masson (1995) determined, in six outflows including LkHα 234, that the peak in the axial distribution of momentum occurs in the middle of the outflow lobes, which they claimed is not explained by any of the standard models. They suggested that either a variable jet velocity or jet wandering was required to explain the momentum distributions they calculated. Recent observations, such as those of NGC 2264G (Fich & Lada, 1997), may provide evidence for the wandering jet hypothesis. Davis *et al.* (1997) observed a correlation between the positions of H_2 knots, ^{12}CO clumps, and peaks in the momentum distribution for the bipolar outflow RNO 15-FIRS. They argue that the correlations indicate that prompt entrainment of ambient material due to shocks is occurring at the positions of the peaks in the momentum distribution.

The detailed analysis carried out in this thesis has allowed a recalculation of the axial momentum distribution for LkHα 234. The momentum per unit length (Figure 44) increases with distance from LkHα 234, reaches a maximum at the approximate mid-point of the length ($\approx$0.3 pc), and then declines. The maximum occurs approximately at an offset of (50", 30"). This result is in agreement with that found by Chernin & Masson (1995). The peak in the distribution is close to the ^{13}CO J = 3 → 2 antenna temperature peak in the outflow, is near the triple-peaked region seen in the ^{12}CO antenna temperature spectra, and is close to the HCO^+ J = 3 → 2 peak in the outflow. This evidence indicates that a complex process is occurring at that position. Whether the peak in the momentum distribution is due to a collision of outflowing material with ambient material, or to prompt entrainment of ambient gas will require further study. It should be noted that there is no evidence for the presence of shocked gas between HH 105 and LkHα 234.

It was previously mentioned that there is blueshifted gas to the northeast of LkHα 234 that appears to overlap the redshifted outflow. This gas is seen in the ^{12}CO column density maps in the velocity range -15 to -14 km s^{-1} (Figure 42). The position angle of the ^{12}CO emission bridge ($\approx 40°$) does not agree with that of the ^{12}CO inner jet, or the position angles of the outflow in the velocity range -9 to -8 km s^{-1}. The position angle is, however, close to that for the blueshifted infrared jet given by Cabrit et al. (1997). Since this blueshifted gas is to the northeast of LkHα 234, rather than to the southwest in the direction of the infrared jet, the connection between the two is not clear. The bridge of emission is energetic, as shown in the previous section, but the fact that it is blueshifted makes it difficult to associate it with the redshifted outflow. It is possible that this feature is only superimposed on the redshifted outflow along the line of sight and is unrelated to any of the known objects in the region near LkHα 234.

7.3 Blueshifted Gas Near GGD 32/HH 103

As was noted in the Introduction, the nature and the exciting source of GGD 32 and HH 103 has not been explicitly determined. Sandell & Liseau (1985) were the first to suggest that GGD 32 may be the blueshifted counterpart of the redshifted molecular outflow, but no conclusive evidence was available at that time. The high resolution (15″) maps of the region surrounding GGD 32 and HH 103 presented in this thesis show that the high velocity blueshifted gas has a distinct swept-back shape (see Figure 17). An interesting feature of the blueshifted gas is that its eastern boundary lies closer to the molecular cavity than that of the western portion of the molecular ridge (see Figure 6). The high velocity gas is partly coincident with a bright, and presumably dense, elongated structure in the molecular ridge (Figure 7). The northern components of HH 103, and most of the constituents of GGD 32 are coincident with this blueshifted clump. This may indicate that the HH objects GGD 32 and HH 103, which have been shown to be shocked gas, are embedded within the high velocity blueshifted gas.

Geometrical evidence suggests that there is a causal link between LkHα 234 and the two groups of HH objects to the northeast and southwest of the star. From Figure 17 in §3.2 it can be seen that the optical and infrared jet axes essentially bound the high velocity blueshifted gas near GGD 32. It is also interesting to note that LkHα 234 lies along a line drawn from HH 105 to GGD 32, further supporting a physical relationship between the southwestern and northeastern groups of HH objects. The shape of the high velocity blueshifted gas could be explained by material moving away from the approximate position of LkHα 234, and encountering a clump of ambient material to the west of the molecular cavity.

The high velocity blueshifted gas to the southwest of the molecular cavity has an estimated kinetic energy of 1.7×10^{44} ergs (see §6.2). The total kinetic energy contained within the outer red wing of the redshifted outflow associated with LkHα 234 is 3.1×10^{45} ergs, which is a factor of 20 greater than that of the moving gas near GGD 32/HH 103. In order for the high velocity blueshifted gas to be the corresponding blue lobe of the outflow, the flow must have undergone an energy depleting process (assuming initial symmetry). The analysis presented in this thesis provides evidence that the pressure within the molecular cavity is lower than that of the ambient molecular material. In particular, the excitation temperatures and column densities (see Figures 40 and 41) indicate, at least along the eastern edge of the cavity, that the gas in the cavity has a similar temperature but lower density than the gas in the ridge. The resulting lower ambient pressure within the cavity would cause the flow to suffer expansion and dissipation due to the reduction in ambient pressure (Leahy, 1991 and references therein). The expansion of the jet may lead to a collimated wind which could produce the swept-back shape of the blueshifted gas. The high velocity blueshifted gas near GGD 32/HH 103, then, is most likely the blue lobe of the outflow associated with LkHα 234.

7.4 FIRS Bipolar Outflow

The new ^{12}CO J = 3 → 2 maps of the bipolar outflow from the FIRS show that the two lobes of this flow are very similar in size and structure. Each lobe contains two ^{12}CO J = 3 → 2 emission peaks. Although they are similar in structure, they are not aligned. The position angles of the blue and red lobes are approximately 26° and 142° respectively. The resulting apparent orthogonal geometry is striking. If the blue lobe was reflected about the bisector of the two position angles it would place it approximately over the red lobe. The two peaks in the blue lobe would also be approximately coincident with the two peaks in the red lobe, although the blue peak of greater intensity would overlap the red peak of lower intensity and vice versa.

The total mass, momentum, and kinetic energy, calculated by the methods described in this thesis, for the red lobe of the FIRS outflow are: (6.8 ± 0.1) M$_\odot$, (8.76 ± 0.01) M$_\odot$ km s^{-1}, and (1.68 ± 0.01) x 10^{44} ergs. These quantities were previously calculated for the FIRS by Edwards & Snell (1983) to be 6.2 M$_\odot$, 49 M$_\odot$ km s^{-1}, and 20 x 10^{44} ergs. Their quoted mass is for the red lobe of the outflow, while the momentum and kinetic energy include both the red and blue lobes. All three values derived in this paper are lower than those of Edwards and Snell (1983). The mass calculated in their paper is comparable, but the momentum and kinetic energy are greater than the values found here by factors of ≈7 and ≈10 respectively. There are several possible reasons for the discrepancy in the latter two results. Edwards & Snell (1983) had to assume that the gas was optically thin since only one CO transition was available to them. The FIRS outflow was shown here to be very optically thick, so their values determined using the optically thin method are definitely underestimated. Edwards & Snell (1983) quote results for the momentum and kinetic energy which are the sums of both the blue and red lobes. From Figure 7 of Edwards & Snell (1983), it can be seen that they have overestimated the extent of the blueshifted gas associated with the FIRS. This is probably due to the larger beam size (50″) of their observations, and the fact that their map is undersampled, since the same extended blueshifted feature is not present in the data described in this paper. The range of kinetic energies which have been calculated for molecular outflows

is 10^{42}-10^{47} ergs (Fukui *et al.* 1993). Assuming that the blue lobe of the outflow is approximately equal to that of the red, the total kinetic energy of the FIRS bipolar outflow is $\approx 3 \times 10^{44}$ ergs, which is well within the range of values for other bipolar outflows.

8 CONCLUSIONS

An investigation of the distribution and kinematics of the molecular gas in NGC 7129, using new high resolution CO observations, was presented in this thesis. These data included a ^{13}CO J = 3 → 2 map of the redshifted molecular outflow associated with LkHα 234, and of the molecular ridge to the south of the Be star. The ^{13}CO J = 3 → 2 observations of the region surrounding LkHα 234, combined with previously published ^{12}CO J = 3 → 2 data, were used in a detailed, channel-by-channel LTE analysis of the physical properties of the region, producing a column density "data cube". The analysis permitted a determination of the mass, momentum, and kinetic energy of the redshifted molecular outflow. The details of the first fully sampled, high resolution ^{12}CO J = 3 → 2 mapping effort of the portion of the molecular cloud to the south of LkHα 234 has been given here. This map, together with new ^{13}CO J = 3 → 2 observations at a number of positions and a new ^{12}CO J = 2 → 1 map, allowed an estimation of the kinematical parameters of the high velocity blueshifted gas to the southwest of the molecular cavity. Similarly, estimates of the mass, momentum, and kinetic energy of the red lobe of the FIRS were calculated. The conclusions are summarized below.

1.   The molecular cavity, as indicated by the ^{13}CO and ^{12}CO J = 3 → 2 maps, is surrounded on the eastern, southern, and western edges by a molecular ridge. The narrower eastern and southern sections, at velocities slightly blue of the ambient velocity, are located to the southeast of their quiescent positions, whereas the broad western segment remains stationary. The pre-main sequence stars SVS 6 and RNO 138S as well as the FIRS may be embedded within the molecular ridge, further supporting the idea that triggered star formation has already occurred in NGC 7129.

2. The detailed analysis has provided an insight into the properties of the gas within the molecular cavity. It was found that the gas in the eastern portion of the cavity has an excitation temperature comparable to that of the gas within the molecular ridge. There is, however, a steep drop off in column density to the west of the ridge and into the cavity. Thus the molecular cavity has a lower ambient pressure than the molecular cloud.

3. A greater understanding of the internal structure of the molecular ridge has been obtained. The ^{12}CO and ^{13}CO J = 3 → 2 observations show that there are at least nine emission peaks distributed around the molecular cavity. The majority of the peaks lie on the eastern and western sections of the ridge. The analysis performed on the region surrounding LkHα 234 proved that the emission peaks on the eastern border of the cavity are actual clumps. The correlation of ^{13}CO line strengths with the positions of the emission peaks near GGD 32/HH 103 indicate that those peaks are clumps as well.

4. There is evidence that triggered star formation is an ongoing process in NGC 7129. The coincidence of the apex of an H_2 emission feature apparently centred on SVS 13 with a kink in the ^{13}CO contours implies that SVS 13 may be compressing the CO clump (Peak 1) located to the east of the star. It is known that the pre-main sequence star BD +65 1637 has a flux that is capable of compressing the ambient material on the eastern border of the molecular cavity. As shown in the ^{13}CO maps, there is a extended clump ≈40″ south of the star, which is most likely being compressed by BD +65 1637.

5. The molecular ridge to the south of LkHα 234 and BD +65 1637, as seen in ^{13}CO J = 3 → 2, is coincident with the optical and infrared emission filament previously observed.

6. The column density channel maps have shown that the redshifted outflow associated with LkHα 234 is sinuous and clumpy. There are three prominent column density enhancements. One of the two clumps observed at redshifted velocities is nearly coincident with an HCO$^+$ J = 3 → 2 peak in the outflow. The third peak is predominantly present at highly redshifted velocities and is coincident with the position of the HH object HH 105.

7. There is blueshifted gas which spatially overlaps the redshifted outflow associated with LkHα 234. It is present in the column density channel maps in the velocity interval -15 to -12.5 km s^{-1}. The position angle of the bridge of emission is approximately 180° from the position angle of the infrared jet. The gas has been found to be energetic ($\approx 10^{43}$ ergs), which is on the order of observed outflow energies. There is no current explanation for this gas.

8. The mass, momentum, and kinetic energy of the red wing of the redshifted outflow associated with LkHα 234 were found to be (26 ± 1) M$_\odot$, (84 ± 4) M$_\odot$ km s^{-1}, and (3.1 ± 0.2) x 10^{45} ergs. The bulk of the mass in the red wing of the outflow was found to be in the inner red wing. It was determined that the mass, momentum, and kinetic energy of the blue wing of the outflow were very much lower than the entire red wing.

9. The momentum distribution along the axis of the redshifted outflow associated with LkHα 234 has been confirmed to peak at a distance of ≈ 0.3 pc from LkHα 234. The position of the peak is roughly coincident with the peak of the redshifted HCO$^+$ J = 3 → 2 gas, the region of triple-peaked ^{12}CO spectra, and a column density clump. These correlations indicate that prompt entrainment may be occurring at this position.

10. The high velocity blueshifted gas to the southwest of LkHα 234 and the molecular cavity has a swept-back shape as might be produced by the interaction of an open wind with a clump of ambient gas. Both complexes of HH objects in the region. GGD 32 and HH 103. appear to be embedded within the extended clump. It is interesting to note that the eastern edge of the clump lies closer to the cavity than that of the molecular ridge, indicating that the process producing the clump may be occurring at the edge of the molecular ridge. The kinematic analysis of the high velocity gas found that the mass, momentum, and kinetic energy of the clump were approximately 1.7 $M_\odot$, 5.9 $M_\odot$ km s^{-1}. and 2.2 x 10^{44} ergs.

11. Based on geometrical arguments, the high velocity blueshifted gas to the southwest of the cavity may be the blue lobe of the outflow associated with LkHα 234. A line drawn from the position of HH 105 to that of GGD 32 passes through the position of LkHα 234 in the submillimetre. Although the kinematical analyses have shown that the blue lobe is less energetic than the red, this does not preclude the possibility that the outflow from LkHα 234 is bipolar. The disagreement in energetics may be explained by the expansion and dissipation of the blue flow during its passage through the molecular cavity.

12. The new, high resolution ^{13}CO map to the south of LkHα 234 showed no intensity peak at the position of the FIRS. The lobes of the bipolar outflow from the FIRS were found to be similar in structure and size. Each lobe has two intensity peaks contained within them. The position angles of the blue and red lobes are approximately 26° and 142° respectively. The two lobes are, in projection on the sky, almost orthogonal to each other. The mass, momentum, and kinetic energy of the red lobe of the bipolar outflow were found to be approximately 6.8 $M_\odot$, 8.8 $M_\odot$ km s^{-1}, and 1.7 x 10^{44} ergs.

BIBLIOGRAPHY

Bachiller, R. 1996, *Ann. Rev. Astron. Ap.*, **34**, 111.

Barsony, M. 1995, in *Clouds, Cores, and Low Mass Stars*, ed. D. P. Clemens and R. Barvainis, Astronomical Society of the Pacific, pg. 197.

Bechis, K. P., Harvey, P. M., Campbell, M. F., and Hoffmann, W. F. 1978, *Ap. J.*, **226**, 439.

Bertout, C. 1987, in *Circumstellar Matter*, IAU Symposium No. 122, ed. I. Appenzeller and C. Jordan, D. Reidel Publishing Company, pg. 23.

Bevington, P. R., and Robinson, D. K. 1992, *Data Reduction and Error Analysis for the Physical Sciences*, Toronto: McGraw-Hill Inc.

Cabrit, S., and Bertout, C. 1986, *Ap. J.*, **307**, 313.

Cabrit, S., Lagage, P.-O., McCaughrean, M. J., and Olofsson, G. 1997, *Astron. Ap.*, **321**, 523.

Cesarsky, C. J., Cesarsky, D. A., Churchwell, E., and Lequeux, J 1978, *Astron. Ap.*, **68**, 33.

Chernin, L. M., Masson, C. R., and Fuller, G. A. 1994, *Ap. J.*, **436**, 741.

Chernin, L. M., and Masson, C. R. 1995, *Ap. J.*, **455**, 182.

Clark, F. 1991, *Ap. J. Suppl.*, **75**, 611.

Cohen, M., and Fuller, G. A., 1985, *Ap. J.*, **296**, 620.

Cohen, M., and Schwartz, R. D. 1983, *Ap. J.*, **265**, 877.

Cohen, M. 1980, *Astron. J.*, **85**, 29.

Damiani, F., Micela, G., Sciortino, S., and Harnden, Jr., F. R. 1994, *Ap. J.*, **436**, 807.

Davis, C. J., Eislöffel, J., Ray, T. P., and Jenness, T. 1997, *Astron. Ap.*, **324**, 1013.

Edwards, S., and Snell, R. L. 1983, *Ap. J.*, **270**, 605.

Eiroa, C., Gómez de Castro, A. I., and Miranda, L. F. 1992, *Astron. Ap. Suppl.*, **92**, 721.

Eiroa, C., Palacios, J., and Casali, M. M. 1998, *Astron. Ap.*, in press.

Elmegreen, B. G. 1992, in *Star Formation in Stellar Systems*, ed. G. Tenorio-Tagle, M. Prieto, and

    F. Sánchez, Cambridge University Press, pg. 381.

Elmegreen, B. G. 1998, in *Origins of Galaxies, Stars, Planets and Life*, ed. C. E. Woodward,

H. A. Thronson, and M. Shull, Astronomical Society of the Pacific Conference Series, in press.

Felli, M., Palagi, F., and Tofani, G. 1992, *Astron. Ap.*, **255**, 293.

Fich, M., and Lada, C. J. 1997, *Ap. J. (Letters)*, **484**, L63.

Fukui Y., Iwata, T., Mizuno, A., Bally, J., and Lane, A. P. 1993, in *Protostars and Planets III*,

    ed. E. H. Levy and J. I. Lunine, University of Arizona Press, pg. 603.

Genzel, R. 1991, in *The Physics of Star Formation and Early Stellar Evolution*, NATO ASI Services,

    ed. C. J. Lada and N. D. Kylafis, pg. 155.

Giannakopoulou, J. 1994, M. Sc. Thesis, Saint Mary's University.

Gómez de Castro, A. I., Miranda, L. F., and Eiroa, C. 1993, *Astron. Ap.*, **267**, 559.

Güsten, R., and Marcaide, J. M. 1986, *Astron. Ap.*, **164**, 342.

Gyulbudaghian, A. L., Glushkov, Y. I., and Denisyuk, I. K. 1978, *Ap. J. (Letters)*, **224**, L237.

Hartigan, P., and Lada, C. 1985, *Ap. J. Suppl.*, **59**, 383.

Herbig, G. H. 1960, *Ap. J. Suppl.*, **4**, 337.

Hodapp, K. 1994, *Ap. J. Suppl.*, **94**, 615.

Hubble, E. 1922, *Ap. J.*, **56**, 162.

Lada, C. J. 1985, *Ann. Rev. Astron. Ap.*, **23**, 267.

Lada, C. J. 1991, in *The Physics of Star Formation and Early Evolution*, ed. C. J. Lada and N. D. Kylafis,

    Dordrecht, pg. 329.

Langer, W. D., and Penzias, A. A. 1990, *Ap. J.*, **357**, 477.

Leahy, J. P. 1991, in *Beams and Jets in Astrophysics*, ed. P. A. Hughes, Cambridge University

    Press, pg. 100.

Lee, S. W. 1992, M. Sc. Thesis, Saint Mary's University.

Levreault, R. 1988, *Ap. J.*, **330**, 897.

Loren, R. B., Vanden Bout, P. A., and Davis, J. H. 1973, *Ap. J. (Letters)*, **185**, L67.

Loren, R. 1977, *Ap. J.*, **218**, 716.

Masson, C. R., and Chernin, L. M. 1992, *Ap. J. (Letters)*, **387**, L47.

Magakian, T. Yu., Boulesteix, J., Marcelin, M., and Le Coarer, E. 1994, *Astron. Ap.*, **291**, 928.

Magakian, T. Yu., and Movsesian, T. A. 1997, *Astron. Rep.*, **41**, 483.

Matthews, H. E. 1994, in *The James Clerk Maxwell Telescope: a Guide for the Prospective User* (Hilo, Hawai'i; Joint Astronomy Centre).

Miranda, L. F., Eiroa, C., Fernández, M., and Gómez de Castro, A. I. 1994a, *Astron. Ap.*, **281**, 864.

Miranda, L. F., Eiroa, C., and Birkle, K. 1994b, *Astron. Ap.*, **289**, L7.

Miranda, L. F., Eiroa, C., and Gómez de Castro, A. I. 1993, *Astron. Ap.*, **271**, 564.

Mitchell, G. F., Hasegawa, T. I., and Schella, J. 1992, *Ap. J.*, **386**, 604.

Mitchell, G. H. 1993, in *Graduate Workshop on Star Formation*, ed. Arcoragi *et al.*, University of McGill Press, pg. 81.

Mitchell, G. F., and Matthews, H. E. 1994, *Ap. J. (Letters)*, **423**, L55.

Mitchell, G. F., 1998, private communication.

Moriarty-Schieven, G. H., and Snell, R. L. 1988, *Ap. J.*, **332**, 364.

Noriega-Crespo, A., Garnavich, P. M., King, N., Böhm, K.-H., and Raga, A. C. 1997, *BAAS*, **28**, 1340.

Padman, R. 1992, *SPECX V6.3 User's Manual* (Cambridge: Cavendish Laboratory).

Palla, F., and Prusti, T. 1993, *Astron. Ap.*, **272**, 249.

Pease, Francis G. 1917, *Ap. J.*, **46**, 24.

Penzias, A. A. 1981, *Ap. J.*, **249**, 518.

Racine, R. 1968, *Astron. J.*, **73**, 233.

Ray, T. 1987, *Astron. Ap.*, **171**, 145.

Ray, T. P., Poetzel, R., Solf, J., and Mundt, R. 1990, *Ap. J. (Letters)*, **357**, L45.

Rodríguez, L. F., Moran, J. M., Ho, P. T. P., and Gottlieb, E. W. 1980, *Ap. J.*, **235**, 845.

Sage, L. J. 1990, *Astron. Ap.*, **239**, 125.

Sandell, G., and Olofsson, H. 1981, *Astron. Ap.*, **99**, 80.

Sandell, G., and Liseau, R. 1985, in *Nearby Molecular Clouds*, ed. G. Serra, Springer-Verlag, pg. 227.

Sandell, G. 1996, private communication.

Schultz, A. S. B., Rank, D., Temi, P., and Harker, D. 1995, *Astrophys. Sp. Sc.*, **233**, 71.

Schwartz, P. R., and Buhl, D. 1975, *Ap. J. (Letters)*, **201**, L27.

Shevchenko, V. S., and Yakubov, S. D. 1989, *Astron. Zu.*, **66**, 718.

Shu F. H., Adams, F. C., and Lizano, S. 1987, *Ann. Rev. Astron. Ap.*, **25**, 23.

Shu, F. H., Ruden, S. P., Lada, C. J., and Lizano, S. 1991, *Ap. J. (Letters)*, **370**, L31.

Spitzer, L. 1978, *Physical Processes in the Interstellar Medium*, Toronto: John Wiley & Sons.

Skinner, S. L., Brown, A., and Stewart, R. T. 1993, *Ap. J. Suppl.*, **87**, 217.

Strom, S. E., Strom, K. M., Yost, J., Carrasco, L., and Grasdalen, G. 1972, *Ap. J.*, **173**, 353.

Strom, S. E., Grasdalen, G. L., and Strom, K. M. 1974, *Ap. J.*, **191**, 111.

Strom, S. E., Strom, K. M., and Grasdalen, G. L. 1975, *Ann. Rev. Astron. Ap.*, **13**, 187.

Tofani, G., Felli, M., Taylor, G. B., and Hunter, T. R. 1995, *Astron. Ap. Suppl.*, **112**, 299.

Torrelles, J. M., Rodríguez, L. F., Cantó, P., Marcaide, J., Moran, J. M., and Ho, P. T 1983, *Ap. J.*, **274**, 214.

Weintraub, D. A., Kastner, J. H., and Mahesh, A. 1994, *Ap. J. (Letters)*, **420**, L87.

Weintraub, D. A., Kastner, J. H., Gatley, I., and Merrill, K. M. 1996, *Ap. J. (Letters)*, **468**, L45.

Wilking, B. A., Mundy, L. G., and Schwartz, R. D. 1986, *Ap. J. (Letters)*, **303**, L61.

Wouterloot, J., Brand, J., and Henkel, C. 1988, *Astron. Ap.*, **191**, 323.

Zinnecker, H., and Preibisch, Th. 1994, *Astron. Ap.*, **292**, 152.

APPENDIX A. DERIVATION OF COLUMN DENSITY EQUATION

For the following discussion, the reader is referred to Mitchell (1992), Lee (1992), and Spitzer (1978) for details. The solution to the radiative transfer equation for a plane parallel cloud is

$$\frac{dI_v}{dz} = \epsilon_v - \kappa_v I_v$$

where z is the path length through the cloud, I_v is the total intensity incident on the back of the cloud, ϵ_v represents the intensity emitted by spontaneous processes within the cloud, and κ_v is a weighting term representing the effects of both stimulated absorption and emission. Assuming that any photons in the cloud are emitted isotropically, the emission term, ϵ_v, may be written as

$$\epsilon_v = \frac{h v}{4 \pi} n_v A_{ul} \phi_v$$

where h is the Planck constant, v is the frequency of the emitted photon, n_u is the density of particles in the higher state of the transition $u \rightarrow l$. A_{ul} is the Einstein constant for spontaneous emission, and ϕ_v is a line profile function which describes the probability of a photon being emitted with a line centre frequency v. The term describing stimulated processes, κ_v, has a similar form, assuming that there is no overall coherence for the bulk gas:

$$\kappa_v = \frac{hv}{4 \pi} (n_u B_{ul} - n_l B_{ul}) \phi_v$$

where n_l is the density of particles in the lower state of the transition, and B_{ul} and B_{lu} are the Einstein coefficients for stimulated absorption and stimulated emission. The Einstein coefficients are defined as follows:

$$A_{ul} = \frac{2h\nu^3}{c^2} B_{ul} = \frac{64 f\pi^4\nu^3}{3hc^3} \mu^2 \frac{u}{g_u}$$

$$B_{ul} = \frac{g_l}{g_u} B_{lu} \quad .$$

Here, c is the speed of light, g_u and g_l are the respective multiplicities of the upper and lower states of the transition, and μ is the dipole constant for the particle in question.

The optical depth, τ_ν is defined as

$$\tau_\nu = -\int_0^z \kappa_\nu dz \quad .$$

Substituting for κ_ν, and using the equation relating B_{ul} to B_{lu}, the optical depth may be expressed as

$$\tau_\nu = -\frac{h\nu}{4\pi} \int_0^z B_{ul} n_u (1 - \frac{n_l}{n_u} \frac{g_u}{g_l}) dz \quad .$$

If local thermodynamic equilibrium (LTE) applies, then the Boltzmann equation may be invoked:

$$\frac{n_l}{n_u} = \frac{g_l}{g_u} e^{\frac{h\nu_{ul}}{kT_{ex}}}$$

where $h\nu_{ul} = E_u - E_l$ is the difference in the energies of the respective levels of the transition. Assuming the gas is in LTE, and substituting for B_{ul}, the optical depth becomes

$$\tau_\nu = \frac{c^2}{8\pi\nu^2} A_{ul} \left(e^{\frac{h\nu_{ul}}{kT_{ex}}} - 1\right) \int_0^z n_u dz \quad .$$

The definition of column density is

$$N_x = \int_0^z n_x dz$$

where x refers to a particular species in the state x, and the integration is over the path length z along the line of sight. The optical depth can now be expressed as

$$\tau_\nu = \frac{c^2}{8\pi\nu^2} A_{ul} \left(e^{\frac{h\nu_{ul}}{kT_{ex}}} - 1\right) N_u \quad .$$

As such, the optical depth is in terms of the column density for the upper state of the transition $u \rightarrow l$. In order to get τ_ν in terms of the column density of the more highly populated lower state, the Boltzmann equation is applied after both sides of the equation have been integrated over the path length. As a function of the column density in the lower state, N_l,

$$\tau_\nu = \frac{c^2}{8\pi\nu^2} \frac{g_u}{g_l} \left(1 - e^{\frac{h\nu_{ul}}{kT_{ex}}}\right) A_{ul} N_l \quad .$$

Substituting for A_{ul} in the above equation and simplifying,

$$\tau_v = \frac{8\pi^3 v_{ul}}{3hc} \frac{u}{g_l} \mu^2 \left(1 - e^{-\frac{hv_{ul}}{kT_{ex}}}\right) N_l$$

Rearranging, and taking the partial derivative with respect to frequency,

$$dN_l = \frac{3hc}{8\pi^3 v} \frac{g_l}{u} \frac{1}{\mu^2} \left(1 - e^{-\frac{hv_{ul}}{kT_{ex}}}\right)^{-1} \tau_v dv \quad .$$

Using the Doppler shift formula, a frequency differential is related to an differential in velocity space via

$$\frac{dv}{v} = \frac{dv}{v} .$$

The column density differential becomes

$$dN_l = \frac{3h}{8\pi^3} \frac{g_l}{u} \frac{1}{\mu^2} \left(1 - e^{-\frac{hv_{ul}}{kT_{ex}}}\right)^{-1} \tau_v dv$$

$$N_l = \frac{3h}{8\pi^3} \frac{g_l}{u} \frac{1}{\mu^2} \left(1 - e^{-\frac{hv_{ul}}{kT_{ex}}}\right)^{-1} \int \tau_v dv$$

where the integral is evaluated over a specified velocity interval.

Consider rotational transitions of linear diatomic molecules. The states are described by the rotational quantum number, J, so for the case considered in this thesis

$$u = J + 1 \quad , \quad \text{and}$$

$$l = J \quad .$$

The rotational energy of a state is given by

$$E_J = hBJ(J+1)$$

where B is the rotational constant for the molecule in question. From the last expression for N_l,

$$N_J = \frac{3h}{8\pi^3} \frac{g_J}{J+1} \frac{1}{\mu^2} \left(1 - e^{-\frac{h\nu_{ul}}{kT_{ex}}}\right)^{-1} \int \tau_\nu dv .$$

To convert the column density of the lower state to the "total" column density (i.e. over all states), the Boltzmann equation is applied in the form

$$\frac{N_J}{N_{TOT}} = \frac{g_J}{U} e^{-\frac{E_J}{kT_{ex}}}$$

where E_J is the energy of the level J, and U is the partition function for the rotational states of a linear molecule:

$$U = \sum_{J=0}^{n} (2J+1) e^{-\frac{E_J}{kT_{ex}}}$$

The partition function may be approximated (Mitchell, 1992) by

$$U \approx \frac{k}{hB} \left(T_{ex} + \frac{hB}{3k}\right) .$$

Solving for N_{TOT} in the Boltzmann equation, and substituting for the rotational energy of the state and the partition function,

$$N_{TOT} = \frac{1}{g_J} \frac{k}{hB} \left(T_{ex} + \frac{hB}{3K} \right) e^{\frac{hBJ(J+1)}{kT_{ex}}} N_J \quad .$$

Therefore, the column density for a linear diatomic molecule is

$$N_{TOT} = \frac{3k}{8\pi^3 B} \frac{1}{\mu^2} \frac{T_{ex} + \frac{hB}{3k}}{J+1} \frac{e^{\frac{hBJ(J+1)}{kT_{ex}}}}{1 - e^{-\frac{h\nu_{ul}}{kT_{ex}}}} \int \tau_\nu \, d\nu \quad .$$

APPENDIX B: DERIVATION OF OPTICALLY THIN EQUATIONS

The constants and variables in this section are the same as those defined in Appendix A. The reader is referred to the same references for details.

Column Density:

The optically thin regime is defined by the condition that the optical depth is very much less than one. The definition of radiation temperature becomes (Mitchell, 1993)

$$T_R \approx \tau_v \frac{h\nu_{ul}}{k} \frac{1}{e^{\frac{h\nu_{ul}}{kT_{ex}}} - 1} \quad .$$

The optical depth can relate the radiation temperature directly to the column density with the equation

$$\tau_v = \frac{8\pi^3\nu_{ul}}{3hc} \frac{u}{g_l} \mu^2 \left(1 - e^{-\frac{h\nu_{ul}}{kT_{ex}}}\right) N_l \quad .$$

Eliminating τ_v from the first equation gives.

$$T_R \approx \frac{8\pi^3\nu^2}{3kc} \frac{u}{g_l} \mu^2 e^{-\frac{h\nu_{ul}}{kT_{ex}}} N_l$$

Isolating N_l, taking the partial derivative with respect to frequency, applying the doppler shift equation to switch to velocity space, and converting the column density in the lower state to the total column density with the use of the Boltzmann equation yields

$$N_{TOT} \approx \frac{3k^2}{8\pi^3 hB\nu_{ul}\mu^2} \frac{\left(T_{ex} + \frac{hB}{3k}\right)}{J + 1} \frac{e^{\frac{hBJ(J+1)}{kT_{ex}}}}{e^{\frac{h\nu_{ul}}{kT_{ex}}}} \int T_R d\nu \quad .$$

This is the equation for the optically thin column density.

Excitation Temperature:

If one has emission from two transitions, $J_1 \rightarrow (J_1 - 1)$ and $J_2 \rightarrow (J_2 - 1)$, for a single molecule, then one may find the excitation temperature in the following manner. Using the second form of radiation temperature expressed in terms of column density, the ratio of the radiation temperatures is

$$\frac{T_R (J_1 - (J_1 - 1))}{T_R (J_2 - (J_2 - 1))} = \frac{v_{J_1 - (J_1 - 1)}}{v_{J_2 - (J_2 - 1)}} \frac{J_1}{J_2} \frac{2 J_2 - 1}{2 J_1 - 1} \frac{N_{(J_1 - 1)}}{N_{(J_2 - 1)}}$$

$$\exp\left[-\frac{h}{kT_{ex}}(v_{J_1 - (J_1 - 1)} - v_{J_2 - (J_2 - 1)}) \right]$$

Applying the Boltzmann equation once, and the definition of the energy of a rotational level repeatedly, this simplifies to

$$\frac{T_R (J_1 - (J_1 - 1))}{T_R (J_2 - (J_2 - 1))} = \left(\frac{J_1}{J_2} \right)^2 \exp\left\{ -\frac{hB}{kT_{ex}}[J_1 (J_1 + 1) - J_2 (J_2 + 1)] \right\} .$$

From this equation, one may calculate an excitation temperature if the line ratio is known.

APPENDIX C. ERROR EQUATIONS

All error equations used in the analysis described in §5 are presented in this appendix. With the exception of the equation for the error on the antenna temperature of a single channel, which was adopted from Sage (1990), all error equations were derived using standard techniques (see Bevington & Robinson, 1992). Only the final results are stated here for the sake of brevity.

Error Equation for an Integrated Intensity:

The error on the integrated intensity, I, for a velocity interval, is given by

$$\sigma_I = \sqrt{(\sigma_{noise})^2 + (\sigma_{base})^2}$$

where noise refers to the noise in the spectrum, or the root-mean-square (rms) temperature, and base refers to the error in calculating the baseline. The individual terms have the form

$$\sigma_{noise} = T_{rms} \cdot \Delta v_i \cdot \left[\frac{\Delta v_c}{\Delta v_i} \right]^{\frac{1}{2}}$$

$$\sigma_{base} = T_{rms} \cdot \Delta v_i \cdot \left[\frac{\Delta v_c}{\Delta v_b} \right]^{\frac{1}{2}}$$

where T_{rms} is the rms (antenna) temperature, Δv_i is the width of the velocity interval considered, Δv_c is the velocity resolution or channel width, and Δv_b is the total width of the velocity interval, or intervals, used to calculate the baseline. If the width of the velocity interval is equal to the channel width ($\Delta v_i = \Delta v_c$), and the definition of integrated intensity is applied, then the equation for the error on the antenna temperature

for a channel of a spectrum is given by

$$\sigma_{T_A^*} = T_{rms} \cdot \sqrt{1 + \left(\frac{1}{\Delta v_b}\right)}$$

Error Equations for Optical Depth, Excitation Temperature, and Column Density:

For simplicity, the following abbreviations are used in this section.

$$\tau = \tau^{13}$$

$$(T_A^*)^{13} = T$$

$$(T_A^*)^{12} = t$$

$$\eta_{MB} = \eta$$

^{13}CO Optical Depth:

$$\sigma_\tau = \frac{\partial \tau}{\partial t} \sqrt{(\sigma_t)^2 + \frac{t^2}{T^2}(\sigma_T)^2}$$

where

$$\frac{\partial \tau}{\partial t} = \frac{\dfrac{\eta^{13}}{\eta^{12}}(1 - e^{-\tau})}{60 T e^{-60\tau} - \dfrac{\eta^{13}}{\eta^{12}} t e^{-\tau}}$$

$$\frac{\partial \tau}{\partial T} = -\frac{t}{T}\frac{\partial \tau}{\partial t}$$

^{12}CO Optical Depth:

$$\sigma_{\tau^{12}} = 60\,\sigma_\tau$$

Excitation Temperature:

$$\sigma_{T_{ex}} = \sqrt{\left(\frac{\partial T_{ex}}{\partial t}\right)^2 (\sigma_t)^2 + \left(\frac{\partial T_{ex}}{\partial T}\right)^2 (\sigma_T)^2}$$

where

$$\frac{\partial T_{ex}}{\partial t} = \frac{T_{ex}^2 \eta^{12} f}{t}\, e^{-\frac{16.595}{T_{ex}}} \left[\frac{A}{t} - B\frac{\partial \tau}{\partial t}\right]$$

$$\frac{\partial T_{ex}}{\partial T} = \frac{T_{ex}^2 \eta^{12} f}{T}\, e^{-\frac{16.595}{T_{ex}}}\, B\frac{\partial \tau}{\partial t}$$

$$A = (1 - e^{-60\tau})$$

$$B = 60\,e^{-60\tau}$$

Column Density:

$$\sigma_{N^{12}} = \sqrt{\left(\frac{\partial N^{12}}{\partial t}\right)^2 (\sigma_t)^2 + \left(\frac{\partial N^{12}}{\partial T}\right)^2 (\sigma_T)^2}$$

where

$$\frac{\partial N^{12}}{\partial t} = N^{12} \frac{\partial T_{ex}}{\partial t} \left\{ \frac{1}{T_{ex} + 0.922} + \frac{1}{\tau} \frac{\partial \tau}{\partial t} \left(\frac{\partial T_{ex}}{\partial t} \right)^{-1} \right.$$

$$\left. - \frac{16.597}{T_{ex}^2} + \frac{16.595}{T_{ex}^2} \frac{1}{e^{\frac{16.595}{T_{ex}}} - 1} \right\}$$

$$\frac{\partial N^{12}}{\partial T} = N^{12} \frac{\partial T_{ex}}{\partial T} \left\{ \frac{1}{T_{ex} + 0.922} + \frac{1}{\tau} \frac{\partial \tau}{\partial T} \left(\frac{\partial T_{ex}}{\partial T} \right)^{-1} \right.$$

$$\left. - \frac{16.597}{T_{ex}^2} + \frac{16.595}{T_{ex}^2} \frac{1}{e^{\frac{16.595}{T_{ex}}} - 1} \right\}$$

Error Equations for the Optically Thin Method:

For this section the following abbreviations to the original notation will apply:

$$T_A^* (J = 2 \rightarrow 1) = T21$$

$$T_A^* (J = 3 \rightarrow 2) = T32$$

$$\eta_{MB} = \eta$$

Case A: Excitation Temperature as a Constant

In this case, the excitation temperature is treated as a constant with an associated error. No functional relationship between the antenna temperatures and the excitation temperature is assumed.

Optical Depth:

$$\sigma_{\tau^{12}} = \tau^{32} \sqrt{(\sigma_{T_{ex}})^2 \left[\frac{-16.595}{T_{ex}^2} \frac{1}{1 - e^{-\frac{16.595}{T_{ex}}}} \right]^2 + \left(\frac{\sigma_{T32}}{T32} \right)^2}$$

Column Density:

$$\sigma_{N^{12}} = N^{32} \sqrt{\left(\frac{\sigma_{T_{ex}}}{T_{ex}} \right)^2 \left[\frac{T_{ex}}{T_{ex} + 0.922} - 16.597 + 16.595 \right]^2 + \left(\frac{\sigma_{T32}}{T32} \right)^2}$$

Case B: Excitation Temperature as a Variable

In this case, the excitation temperature is treated as a function of ^{12}CO antenna temperature and optical depth. In this situation, the partial derivatives are nonzero.

Excitation Temperature:

$$\sigma_{T_{ex}} = \frac{T_{ex}^2}{16.597} \sqrt{\left(\frac{\sigma_{T32}}{T32} \right)^2 + \left(\frac{\sigma_{T21}}{T21} \right)^2}$$

Optical Depth:

$$\sigma_{\tau^{32}} = \tau^{32} \sqrt{\left(\frac{\sigma_{T32}}{T32}\right)^2 \left[1 - \frac{1}{1 - e^{\frac{-16.595}{T_{ex}}}}\right]^2 + \left(\frac{\sigma_{T21}}{T21}\right)^2 \left[\frac{1}{1 - e^{\frac{-16.595}{T_{ex}}}}\right]^2}$$

Column Density:

$$\sigma_{N^{32}} = \frac{N^{32} T_{ex}^2}{16.595} \left[\left(\frac{\sigma_{T32}}{T32}\right)^2 \left\{ 2 \cdot \frac{16.595}{T_{ex}^2} + \frac{1}{T_{ex} + 0.922} - \frac{16.597}{T_{ex}^2} \right\}^2 \right.$$

$$\left. + \left(\frac{\sigma_{T21}}{T21}\right)^2 \left\{ \frac{16.595}{T_{ex}^2} + \frac{1}{T_{ex} + 0.922} - \frac{16.597}{T_{ex}^2} \right\}^2 \right]^{\frac{1}{2}}$$

General Error Equations:

In this section, error equations for quantities such as kinetic energy, whose functional forms are independent of the method used to calculate the column density, are presented.

H_2 Column Density:

$$\sigma_{N_{H_2}} = 10^4 \sigma_{N^{32}}$$

Surface Density:

$$\sigma_{\sigma_j} = 1.4 \cdot 2 \cdot m_H \sigma_{N_{32}}$$

Mass (in grams):

$$\sigma_m = A \sigma_{\sigma_j}$$

Mass (in $M_\odot$):

$$\sigma_{m_s} = \frac{\sigma_m}{M_\odot}$$

Momentum:

$$\sigma_p = \frac{v_j - V_{LSR}}{\cos\theta} \sigma_{m_s}$$

Kinetic energy:

$$\sigma_{E_k} = \frac{1}{2} \frac{[(v_j - V_{LSR})10^5]^2}{\cos^2\theta} \sigma_m$$

APPENDIX D: PARAM.C

thesis.h:

```
#define NUM13 179            /* 13CO file size                              */
#define BINS 180             /* total # of bins allowed                     */
#define NUM12 237            /* 12CO file size                              */
#define FINAL 178            /* # of channels for FITS file                 */
#define MAXCEN 66            /* maximum # of channels in array centre       */
#define MAXWING 173          /* maximum # of channels in arrays red & blue  */
#define WIDTH12 0.215220     /* 12CO velocity resolution in km s-1          */
#define WIDTH13 2.83370E4    /* 13CO velocity resolution in cm s-1          */
#define BINRATIO 0.759502    /* ratio of 13CO to 12CO channel widths (km s-1) */
#define MB12 0.53            /* 12CO main beam efficiencies                 */
#define MB13 0.58            /* 13CO main beam efficiencies                 */
#define ABUND60 60.0         /* abundance ratio - 12CO/13CO                 */
#define ABUNDH2 1.0E4        /* abundance ratio - H2/12CO                   */
#define ABUNDHE 1.4          /* factor to account for helium abundance      */
#define TAULIMIT 1.0000061442501049  /* TR ratio which gives a tau of 12.0  */
#define THICK1 7.698E8       /*                                             */
#define COEFF3 0.922         /*          for calculating                    */
#define COEFF1 16.597        /*          column densities                   */
#define COEFF2 16.595        /*                                             */
#define THIN1 4.6394E7       /*                                             */
#define AREA 3.955E34        /* area of 15" beam at 1 kpc                   */
#define THETA 0.349066       /* opening angle of outflow (20°)              */
#define MSUN_INV 5.028E-34   /* inverse of the mass of the sun (grams)      */
#define MH 1.674E-24         /* mass of hydrogen atom (grams)               */
#define CONVERT 1.0E5        /* to convert velocities to from mks to cgs    */
#define VLSR -10.0           /* VLSR of LKHA23 in km s-1                     */
#define COUNTER 45           /* counter to create interpolation table in tau */
#define ADJUST 67            /* constant used to adjust bin #'s             */
#define ERROR12 1.002150     /* to produce sigma's for 12CO T*A's           */
#define ERROR13 1.004040     /* to produce sigma's for 13CO T*A             */
#define RL 111               /* RL, BL, and CL are for test loops in total  */
#define BL 115
#define CL 106
```

```
#include <stdio.h>
#include <math.h>
#include "thesis.h"


/****************************************************/
/*                                                */
/*          procedure declarations               */
/*                                                */
/****************************************************/


double roundoff(float);
void initialize(double[][8],double[][8]);
void douze();
void boundary13();
void input_tex();
void input_errors();
void rebin();
void assign();
void tau();
void thick();
void sigma_thick();
void temperature();
void into(double[][10],double[][10],double *,double *,int *,int *);
void thin(double[][10], double *, int *);
void outof(double[][10],double[][10],int *,int *);
void sigma_thin(double[][10],double[][8],double *,double *,int *);
void outof_sigma(double[][8],double[][8],int *,int *);
void output();
void total();
void intervals();




/****************************************************/
/*                                                */
/*                                                */
/*          declaration of global variables       */
/*                                                */
/*                                                */
/****************************************************/
```

int redlim,bluelim; /* limits of ^{13}CO spectra */
int range; /* number of channels where there is ^{12}CO & ^{13}CO*/
int upper12,lower12; /* limits of ^{12}CO spectra */
double texred, texblue; /* ^{12}CO red & blue wing T_{ex} */
double sigmared,sigmablue; /* errors on ^{12}CO red & blue wing T_{ex}'s */
double sigma12,sigma13; /* errors on ^{12}CO and ^{13}CO spectra */

double twelve[NUM12][2];
  /* twelve[i][0] = channel upper boundary */
  /* twelve[i][1] = temperature */

```
double thirteen[NUM13][2];
        /* thirteen[i][0] = channel centre velocity              */
        /* thirteen[i][1] = channel upper boundary               */


double new12[BINS][2];
        /* new12[i][0] = channel centre velocity                 */
        /* new12[i][1] = rebinned temperature                    */


double new_12[FINAL][2];
        /* column definitions same as for new12                  */


double centre[MAXCEN][14];
        /* centre[i][0]  = channel centre velocity               */
        /* centre[i][1]  = rebinned antenna temperature          */
        /* centre[i][2]  = temperature ratio                     */
        /* centre[i][3]  = 13CO optical depth                    */
        /* centre[i][4]  = 12CO optical depth                    */
        /* centre[i][5]  = # of iterations required   to return optical depth */
        /* centre[i][6]  = 12CO excitation temperature           */
        /* centre[i][7]  = 12CO column density                   */
        /* centre[i][8]  = H2 column density                     */
        /* centre[i][9]  = surface density of cell               */
        /* centre[i][10] = mass of cell                          */
        /* centre[i][11] = mass of cell in Mo                    */
        /* centre[i][12] = momentum of cell                      */
        /* centre[i][13] = kinetic energy of cell                */


double sigcentre[MAXCEN][10];
        /* sigcentre[i][0] = 13CO optical depth error for centre values */
        /* sigcentre[i][1] = 12CO optical depth error           */
        /* sigcentre[i][2] = 12CO excitation temp error         */
        /* sigcentre[i][3] = 12CO column density error          */
        /* sigcentre[i][4] = H2 column density error            */
        /* sigcentre[i][5] = surface density error              */
        /* sigcentre[i][6] = mass error                         */
        /* sigcentre[i][7] = mass error in Mo                   */
        /* sigcentre[i][8] = momentum error                     */
        /* sigcentre[i][9] = kinetic energy error               */


double red[MAXWING][10];
        /* red[i][0] = channel centre velocity                  */
        /* red[i][1] = rebinned temperature                     */
        /* red[i][2] = 12CO optical depth                       */
        /* red[i][3] = 12CO column density                      */
        /* red[i][4] = H2 column density                        */
        /* red[i][5] = surface density of cell                  */
        /* red[i][6] = mass of cell                             */
        /* red[i][7] = mass of cell in Mo                       */
        /* red[i][8] = momentum of cell                         */
        /* red[i][9] = kinetic energy of cell                   */
```

```
double sigred[MAXWING][8];
        /* sigred[i][0] = 12CO optical depth error              */
        /* sigred[i][1] = 12CO column density error             */
        /* sigred[i][2] = H2 column density error               */
        /* sigred[i][3] = surface density error                 */
        /* sigred[i][4] = mass error                            */
        /* sigred[i][5] = mass error in M☉                      */
        /* sigred[i][6] = momentum error                        */
        /* sigred[i][7] = kinetic energy error                  */


double blue[MAXWING][10];
        /* column definitions the same as for red              */


double sigblue[MAXWING][8];
        /* column definitions the same as for sigred           */


double col3[MAXCEN];
        /* col3[i] = bin temperature                           */


double sumred[3][2];
        /* sumred[0][0] = total mass of outer red wing         */
        /* sumred[0][1] = error on total mass                  */
        /* sumred[1][0] = total momentum                       */
        /* sumred[1][1] = error on total momentum              */
        /* sumred[2][0] = total kinetic energy                 */
        /* sumred[2][1] = error on total kinetic energy        */


double sumcen[3][2];
        /* sumcen[0][0] = total mass of inner red wing         */
        /* sumcen[0][1] = error on total mass                  */
        /* sumcen[1][0] = total momentum                       */
        /* sumcen[1][1] = error on total momentum              */
        /* sumcen[2][0] = total kinetic energy                 */
        /* sumcen[2][1] = error on total kinetic energy        */


double sumblue[3][2];
        /* sumblue[0][0] = total mass of blue wing             */
        /* sumblue[0][1] = error on total mass                 */
        /* sumblue[1][0] = total momentum                      */
        /* sumblue[1][1] = error on total momentum             */
        /* sumblue[2][0] = total kinetic energy                */
        /* sumblue[2][1] = error on total kinetic energy       */
```

<<<<<<<<<<<<<<<< PROCEDURE: main >>>>>>>>>>>>>>>

```c
void main(void)
{
        double   dummy1[MAXWING][10],   dummy2[MAXWING][10],   dummy4[MAXWING][8];
        double dummy5[MAXWING][8];
        double texr,texb, str,stb;
        int countr,countb;

        initialize(dummy4,dummy5);
        douze();
        boundary13();
        input_tex();
        input_errors();
        rebin();
        assign();
        tau();
        thick();
        sigma_thick();
        texr=0.0; texb=0.0; countr=0; countb=0;
        into(dummy1,dummy2,&texr,&texb,&countr,&countb);
        thin(dummy1,&texr,&countr);
        thin(dummy2,&texb,&countb);
        outof(dummy1,dummy2,&countr,&countb);
        str=sigmared;
        stb=sigmablue;
        sigma_thin(dummy1,dummy4,&texr,&str,&countr);
        sigma_thin(dummy2,dummy5,&texb,&stb,&countb);
        outof_sigma(dummy4,dummy5,&countr,&countb);
        output();
        total();
        intervals();

} /* end main */
```

<<<<<<<<<<<<<<<< PROCEDURE: roundoff >>>>>>>>>>>>>>>

```c
double roundoff(float temp)
{
        double number,result;
        double a,b;

        number=temp;
        a=(int)(number*(double)2000000);
        b=(int)(number*(double)1000000);
        result=(((double)(a-b))*0.000001)+0.0000000001;
        return result;

} /* end roundoff */
```

<<<<<<<<<<<<<<<<< PROCEDURE: initialize >>>>>>>>>>>>>>>>

```
void initialize(double array1[][8], double array2[][8])
{
        int i,j,k,b,a,c,p,m,n,w,x,y,z,r,s,t;

        redlim=0; bluelim=0; upper12=0; lower12=0;
        range=0.0; sigmared=0.0; sigmablue=0.0; texred=0.0; texblue=0.0; sigma12=0.0; sigma13=0.0;

        for(i=0;i<NUM12;i++)
        {
                for(w=0;w<2;w++)
                        {twelve[i][w]=0.0;}
        }
        for(j=0;j<NUM13;j++)
        {
                for(x=0;x<2;x++)
                        {thirteen[j][x]=0.0;}
        }
        for(k=0;k<BINS;k++)
        {
                for(y=0;y<2;y++)
                        {new12[k][y]=0.0;}
        }
        for(a=0;a<MAXCEN;a++)
        {
                col3[a]=0.0;
                for(c=0;c<14;c++)
                        {centre[a][c]=0.0;}
                for(z=0;z<10;z++)
                        {sigcentre[a][z]=0.0;}
        }
        for(b=0;b<MAXWING;b++)
        {
                for(r=0;r<10;r++)
                        {red[b][r]=0.0; blue[b][r]=0.0;}
                for(s=0;s<8;s++)
                        {sigred[b][s]=0.0; sigblue[b][s]=0.0; array1[b][s]=0.0; array2[b][s]=0.0;}
        }
        for(p=0;p<3;p++)
        {
                for(t=0;t<2;t++)
                        {sumred[p][t]=0.0; sumblue[p][t]=0.0;}
        }
        for(m=0;m<FINAL;m++)
        {
                for(n=0;n<2;n++)
                        {new_12[m][n]=0.0;}
        }
} /* end initialize */
```

```
void douze()
{
        FILE *bound12;
        FILE *col2dat;
        FILE *limit;
        float a,b;
        int i,m,one,two;
        float three,four;

        /*              to read in channel upper bounds              */

        bound12=fopen("12bound.dat","r");
        for (m=0;m<NUM12;m++)
        {
                a=0;
                b=0;
                fscanf(bound12,"%f %f",&a,&b);
                twelve[NUM12-1-m][0]=roundoff(b);
        } /* end for */
        fclose(bound12);

        /*              to read in channel temperatures              */

        col2dat=fopen("12co.dat", "r");
        for(i=0;i<NUM12;i++)
        {
                one=0;
                two=0;
                three=0.0;
                four=0.0;
                fscanf(col2dat,"%i %i %f %f",&one,&two,&three,&four);
                twelve[i][1]=roundoff(four);
        }       /* end for */
        fclose(col2dat);

        /*              to read in end channels of 12CO spectrum      */

        limit=fopen("lim12.dat","r");
        fscanf(limit,"%i %i",&upper12,&lower12);
        fclose(limit);

} /* end douze */
```

```
<<<<<<<<<<<<<<<<   PROCEDURE:  boundary13    >>>>>>>>>>>>>>>


void boundary13()
{
        FILE *bound13;
        float a,b;
        int w;

        /*      to read in channel centres and upper bounds              */

        bound13=fopen("13bound.dat","r");
        for(w=0;w<NUM13;w++)
        {
                a=0;
                b=0;
                fscanf(bound13,"%f %f",&a,&b);
                thirteen[NUM13-1-w][0]=roundoff(a);
                new12[BINS-1-w][0]=thirteen[NUM13-1-w][0]; /* for centre vel */
                thirteen[NUM13-1-w][1]=roundoff(b);
        } /* end for */
        fclose(bound13);

} /* end boundary13*/




                <<<<<<<<<<<<<<<   PROCEDURE:  input_tex    >>>>>>>>>>>>>>>


void input_tex()
{
        FILE *wing;
        float xred,xblue;
        float xrerr,xberr;

        xred=0.0;
        xrerr=0.0;
        xblue=0.0;
        xberr=0.0;
        wing=fopen("tex_wing.dat","r");
        fscanf(wing,"%f %f %f %f",&xred,&xrerr,&xblue,&xberr);
        fclose(wing);

        texred=(double)xred;
        sigmared=(double)xrerr;
        texblue=(double)xblue;
        sigmablue=(double)xberr;

} /* end input_tex */
```

<<<<<<<<<<<<<<<< PROCEDURE: input_errors >>>>>>>>>>>>>>>>

```c
void input_errors()
{
        FILE *sigma;
        float s12,s13;

        /* to read in errors for 12CO and 13CO spectra            */

        sigma=fopen("sigma.dat","r");
        fscanf(sigma,"%f %f",&s12,&s13);
        sigma12=(double)(s12*ERROR12);
        sigma13=(double)(s13*ERROR13);
        fclose(sigma);

} /* end input_errors */
```

<<<<<<<<<<<<<<<<< PROCEDURE: rebin >>>>>>>>>>>>>>>>

```
void rebin()
{
        int p,q,c,z,check;
        float diff;
        double weight;

        p=0; q=0; c=1; check=1; diff=0.0;
        while (check==1)        /* NOTE:  The p coming out of this loop is the 12CO bin want     */
        {                       /*              to begin the rebinning procedure at.             */
                diff=twelve[p][0]-thirteen[q][1];
                if (diff<0.0)
                        {q++;}
                else if (diff>=WIDTH12)
                        {p++;}
                else
                        {check=2;}      /* corresponds to diff<WIDTH12 and diff>=0 */
        } /* end while */
        p--;
        while(c<BINS)
        {
                p++; weight=0.0;
                weight=(twelve[p][0]-thirteen[q][1])/WIDTH12;
                if (weight==0.0)
                        {new12[c][1]+=twelve[p][1]*BINRATIO;}
                else if(weight>0.0)
                {
                        new12[c][1]+=(1.0-weight)*twelve[p][1]*BINRATIO;
                        new12[c-1][1]+=weight*twelve[p][1]*BINRATIO;
                }
                else if( (weight<0.0) && (twelve[p+1][0]>thirteen[q+1][1]) )
                        {new12[c][1]+=twelve[p][1]*BINRATIO;}
                else
                {
                        q++; c++; p--;
                }
        } /* end while */

        /* to assign new12 to a new array minus the buffer bins     */
        for(z=0;z<FINAL;z++)
        {
                new_12[z][0]=new12[z+1][0]; new_12[z][1]=new12[z+1][1];
        }
} /* end rebin */
```

```
<<<<<<<<<<<<<<<<    PROCEDURE: assign    >>>>>>>>>>>>>>>>

void assign()
{
        FILE *endpoints, *col3dat;
        int rlim,blim,one,two,x,y,z,r,b,c;
        float three,four;
        double temp[MAXCEN];

        /* to read in the limits of the 13CO spectrum          */
        /* rlim and blim are for array treize                  */
        endpoints=fopen("limits.dat","r");
        fscanf(endpoints,"%i %i",&rlim,&blim);
        fclose(endpoints);
        range=(blim+1)-rlim;
        /* to adjust the bin #'s to those of the large range          */
        /* redlim and bluelim are for arrays thirteen, new12, and centre     */
        redlim = rlim + ADJUST; bluelim = blim + ADJUST;

        for (x=0;x<MAXCEN;x++)        /* to initialize temp */
                {temp[x]=0.0;}

        col3dat=fopen("13co.dat","r");    /* to fill array temp with ¹³CO values */
        for (y=0;y<MAXCEN;y++)
        {
                one=0; two=0; three=0; four=0;
                fscanf(col3dat,"%i %i %f %f",&one,&two,&three,&four);
                temp[y]=roundoff(four);
        }
        fclose(col3dat);

        for(z=rlim;z<(blim+1);z++)        /* to fill array col3 */
                {col3[z-rlim]=temp[z];}
        for(c=redlim;c<(bluelim+1);c++)    /* to fill array centre */
                {centre[c-redlim][0]=new_12[c][0]; centre[c-redlim][1]=new_12[c][1];}
        for(r=0;r<redlim;r++)        /* to fill arrays red and blue */
                {red[r][0]=new_12[r][0]; red[r][1]=new_12[r][1];}
        for(b=(bluelim+1);b<FINAL;b++)
                {blue[b-bluelim-1][0]=new_12[b][0]; blue[b-bluelim-1][1]=new_12[b][1];}
} /* end assign */
```

```c
void tau()
{
        double tau13[COUNTER]={0.000000001, 0.000001, 0.000005, 0.000010, 0.000050, 0.001000,
                             0.002500, 0.005000, 0.007500, 0.010000, 0.015000, 0.020000,
                             0.025000, 0.030000, 0.040000, 0.050000, 0.060000, 0.070000,
                             0.080000, 0.090000, 0.100000, 0.150000, 0.200000, 0.250000,
                             0.300000, 0.350000, 0.400000, 0.450000, 0.500000, 0.750000,
                             1.000000, 2.000000, 3.500000, 4.000000, 5.000000, 5.500000,
                             6.000000, 7.000000, 8.500000, 9.000000, 10.000000, 10.500000,
                             11.000000,11.500000,12.000000};
        int j,i,iterations,y,t,m;
        double ratio,table[COUNTER][2],hightemp,lowtemp,hightau,lowtau,tau,newratio,tausum,test;

        for(m=0;m<COUNTER;m++)          /* to initialize array table */
                {table[m][0]=tau13[m]; table[m][1]=0.0;}
        for(t=0;t<COUNTER;t++)                  /* to create interpolation table */
                {table[t][1]=(1-exp(-60*tau13[t]))/(1-exp(-tau13[t]));}
        for(i=0;i<range;i++)
        {
           ratio=(centre[i][1]*MB13)/(col3[i]*MB12);
           if ((ratio>TAULIMIT) && (ratio<60.0))
           {
              centre[i][2]=ratio; j=1;
              while (j!=500)
              {
                    if (table[j][1]<ratio)
                    {
                        hightemp=table[j][1]; lowtemp=table[j-1][1]; hightau=table[j][0]; lowtau=table[j-1][0];
                        tau=((ratio-lowtemp)/(hightemp-lowtemp))*(hightau-lowtau)+lowtau;
                        newratio=(1-exp(-ABUND60*tau))/(1-exp(-tau)); iterations=1;
                        test=pow(((ratio-newratio)/ratio),2);
                        while (test>1.0e-23)
                        {
                          if ((ratio-newratio)<0)
                          {
                              lowtemp=newratio; lowtau=tau;
                              tau=((ratio-lowtemp)/(hightemp-lowtemp))*(hightau-lowtau)+lowtau;
                          }
                          else
                          {
                              hightemp=newratio; hightau=tau;
                              tau=((hightemp-ratio)/(hightemp-lowtemp))*(hightau-lowtau)+lowtau;
                          }
                          newratio=(1-exp(-ABUND60*tau))/(1-exp(-tau)); iterations++;
                          test=pow(((ratio-newratio)/ratio),2); tausum=0;
```

```
                        if(iterations>2000)
                        {
                             for(y=0;y<100;y++)
                             {
                              if ((ratio-newratio)<0.0)
                              {
                               lowtemp=newratio; lowtau=tau;
                               tau=((ratio-lowtemp)/(hightemp-lowtemp))*(hightau-lowtau)+lowtau;
                              }
                              else
                              {
                               hightemp=newratio; hightau=tau;
                               tau=((hightemp-ratio)/(hightemp-lowtemp))*(hightau-lowtau)+lowtau;
                              }
                              tausum += tau; newratio=(1-exp(-ABUND60*tau))/(1-exp(-tau));
                             }
                             tau=tausum*0.01; test=1.0e-24;
                            }
                        }
                        centre[i][3]=tau; centre[i][4]=tau*ABUND60; centre[i][5]=(double)iterations;
                        j=499;
                       }
                     j++;
                 }
            }
        else if (ratio>60.0)
                {centre[i][2]=-2.0; centre[i][3]=-2.0; centre[i][4]=-2.0;}
        else if (ratio==60.0)
                {centre[i][2]=60.0; centre[i][3]=0.0; centre[i][4]=0.0;}
        else if ((ratio>=1.0) && (ratio<=TAULIMIT))
                {centre[i][2]=ratio; centre[i][3]=12.00; centre[i][4]=centre[i][3]*ABUND60;}
        else if (ratio<0.0)
                {centre[i][2]=ratio; centre[i][3]=-1.0; centre[i][4]=-1.0;}
        else                                            /* this is if 0 <= ratio < 1.0 */
                {centre[i][2]=ratio; centre[i][3]=-3.0; centre[i][4]=-3.0;}
        }
}  /* end tau */
```

<<<<<<<<<<<<<<<<   PROCEDURE: thick   >>>>>>>>>>>>>>>

```c
void thick()
{
        int x,p,q;
        double test;

        for(x=0;x<range;x++)
        {
                test=( (double)COEFF2*(double)MB12*(1/centre[x][1])*(1-exp(-centre[x][4])) )+1.0;
                if(centre[x][4]<0.0)
                {
                        for(p=1;p<9;p++)
                                {centre[x][p]=0.0;}
                }
                else if(test<=0.0)
                {
                        for(q=1;q<9;q++)
                                {centre[x][q]=0.0;}
                }
                else
                {
                        centre[x][6]=COEFF2/log(test); /* for 12CO Tcx */

                        /* for 12CO column density           */
                        centre[x][7]=(centre[x][6]+COEFF3)*centre[x][4]*WIDTH13*(exp(COEFF1/
                                        centre[x][6])/(1-exp(-COEFF2/centre[x][6])))*THICK1;

                        centre[x][8]=ABUNDH2*centre[x][7]; /* for H2 column density */

                        centre[x][9]=2.0*ABUNDHE*centre[x][8]*MH; /* for surface density */

                        centre[x][10]=centre[x][9]*AREA; /* for mass in g */

                        centre[x][11]=centre[x][10]*MSUN_INV; /* for mass in Mo */

                        /* to calculate momentum in Mo*km/s       */
                        centre[x][12]=centre[x][11]*(centre[x][0]-VLSR)*(1/cos(THETA));
                        if(centre[x][12]<0.0)
                                {centre[x][12]=-centre[x][12];}

                        /* to calculate kinetic energy in ergs       */
                        centre[x][13]=(0.5/pow( cos(THETA), 2) )*pow( (centre[x][0]-VLSR), 2)*
                                        centre[x][10]*CONVERT*CONVERT;

                }
        }
} /* end thick */
```

```
<<<<<<<<<<<<<<<<    PROCEDURE:  sigma_thick    >>>>>>>>>>>>>>>

void sigma_thick()
{
        double dtau,A,B,C,D,E,F,G,H,I,J,K,L,sigl2,sigl3;
        int z,x;

        for(z=0;z<range;z++)
        {
          if(centre[z][4]==0.0)
          { for(x=0;x<10;x++) {sigcentre[z][x]=0.0;} }
          else
          {
                dtau=0.0; A=0.0; B=0.0; C=0.0; D=0.0; E=0.0; F=0.0; G=0.0;
                H=0.0; I=0.0; J=0.0; K=0.0; L=0.0; sigl2=0.0; sigl3=0.0;

                dtau=(MB13/MB12)*(1-exp(-centre[z][3]))/( (col3[z]*ABUND60*exp(-centre[z][4])) -
                        (centre[z][1]*(MB13/MB12)*exp(-centre[z][3])) );
                A=ABUND60*exp(-centre[z][4])*dtau;
                B=(1/centre[z][1])*(1-exp(-centre[z][4])); D=COEFF1/COEFF2;
                E=(centre[z][6]*centre[z][6]/COEFF2)*(1/(centre[z][6]+COEFF3));
                F=1/(exp(COEFF2/centre[z][6])-1); C=D-E+F; G=centre[z][1]/col3[z];
                H=exp(-COEFF2/centre[z][6]); I=COEFF2*MB12/centre[z][1]; J=A-B;
                K=C+(1/(H*I*J*centre[z][3]))*dtau; L=C+(1/(H*I*A*centre[z][3]))*dtau;
                sigl2=sigmal2*sigmal2; sigl3=sigmal3*sigmal3;

                sigcentre[z][0]=dtau*pow((sigl2+(sigl3*G*G)),0.5); /* error for ¹³CO τ */
                if(sigcentre[z][0]<0.0) {sigcentre[z][0]=-sigcentre[z][0];}

                sigcentre[z][1]=ABUND60*sigcentre[z][0]; /* error for ¹²CO τ */
                if(sigcentre[z][1]<0.0) {sigcentre[z][1]=-sigcentre[z][1];}

                sigcentre[z][2]=(MB12*centre[z][6]*centre[z][6]/centre[z][1])*H* /* for ¹²CO T_x */
                        pow( ((sigl2*J*J)+(sigl3*G*G*A*A)),0.5);

                /* for ¹²CO column density                    */
                sigcentre[z][3]=centre[z][7]*H*I*pow( ( (sigl2*J*J*K*K)+(sigl3*G*G*A*A*L*L) ),0.5);

                sigcentre[z][4]=ABUNDH2*sigcentre[z][3]; /* for H2 column density */

                sigcentre[z][5]=ABUNDHE*2.0*MH*sigcentre[z][4]; /* for surface density */

                sigcentre[z][6]=AREA*sigcentre[z][5]; /* for mass */

                sigcentre[z][7]=sigcentre[z][6]*MSUN_INV; /* for mass in M_o */

                sigcentre[z][8]=(centre[z][0]-VLSR)*sigcentre[z][7]*(1/cos(THETA));

                sigcentre[z][9]=(centre[z][0]-VLSR)*CONVERT*CONVERT*(centre[z][0]-VLSR)*0.5*
                        sigcentre[z][6]*(1/(cos(THETA)*cos(THETA)));
          } /* end else */ } /* end for */
} /* end sigma_thick */
```

```
<<<<<<<<<<<<<<<    PROCEDURE: into    >>>>>>>>>>>>>>>

void into(double array1[][10],double array2[][10],double *temp1, double *temp2, int *count1, int *count2)
{
        int i,j,x,z;

        /* to fill array1 (dummy1) with array red, initializing          */
        /* to zero first                                        */

        *count1=redlim-1;
        for(i=0;i<*count1;i++)
        {
                for(j=0;j<10;j++)
                {
                        array1[i][j]=0.0;
                        array1[i][j]=red[i][j];
                }
        }

        /* to fill array2 (dummy2) with array blue initializing          */
        /* to zero first                                        */

        *count2=BINS-bluelim-2;
        for(x=0;x<*count2;x++)
        {
                for(z=0;z<10;z++)
                {
                        array2[x][z]=0.0;
                        array2[x][z]=blue[x][z];
                }
        }

        *temp1=texred;
        *temp2=texblue;

} /* end into */
```

```
<<<<<<<<<<<<<<<    PROCEDURE:  thin    >>>>>>>>>>>>>>

void thin(double dummy3[][10], double *tex, int *max)
{
        int i,x;

        for(i=0;i<(*max);i++)
        {
                if(dummy3[i][1]<0.0)
                {
                        for(x=0;x<8;x++)
                                {dummy3[i][x]=0.0;}
                }
                else
                {
                        /* to calculate 12CO optical depth          */
                        dummy3[i][2]=(dummy3[i][1]/MB12)*(1/COEFF2)*(exp(COEFF2/(*tex))-1);

                        /* to calculate 12CO column density          */
                        dummy3[i][3]=THIN1*((*tex)+COEFF3)*WIDTH13*(dummy3[i][1]/MB12)*
                                        exp(COEFF1/(*tex))*(1/exp(COEFF2/(*tex)));

                        dummy3[i][4]=ABUNDH2*dummy3[i][3]; /* for H2 column density */

                        dummy3[i][5]=2.0*ABUNDHE*dummy3[i][4]*MH; /* for surface density */

                        dummy3[i][6]=dummy3[i][5]*AREA;      /* to calculate mass      */

                        dummy3[i][7]=dummy3[i][6]*MSUN_INV;  /* to calculate mass in Mₒ */

                        /* to calculate momentum in Mₒ*km/s       */
                        dummy3[i][8]=(dummy3[i][7]/cos(THETA))*(dummy3[i][0]-VLSR);
                        if(dummy3[i][8]<0.0)
                                {dummy3[i][8]=-dummy3[i][8];}

                        /* to calculate kinetic energy in ergs       */
                        dummy3[i][9]=(0.5/pow( cos(THETA), 2) )*pow( (dummy3[i][0]-VLSR), 2)*
                                        dummy3[i][6]*CONVERT*CONVERT;

                }
        }
} /* end thin */
```

```
void outof(double array1[][10], double array2[][10], int *count1, int *count2)
{
        int p,q,r,t;

        /* to read values calculated in thin back into        */
        /* respective global arrays                           */

        for(p=0;p<*count1;p++)
        {
                for(q=2;q<10;q++)
                {
                        red[p][q]=array1[p][q];
                }
        }

        for(r=0;r<*count2;r++)
        {
                for(t=2;t<10;t++)
                {
                        blue[r][t]=array2[r][t];
                }
        }

} /* end outof */
```

```
void sigma_thin(double val[][10], double err[][8], double *temp, double *texerr, int *count)
{
        int z,g;
        double A,B,C,D,E,sigtex;

        for(z=0;z<*count;z++)
        {
                if(val[z][1]<=0.0)
                {
                        for(g=0;g<8;g++)
                                {err[z][g]=0.0;}
                }
                else
                {
                        /* to calculate initial values                    */
                        A=(sigma12/val[z][1])*(sigma12/val[z][1]);
                        B=COEFF1/(*temp);
                        C=COEFF2/(*temp);
                        sigtex=(*texerr)*(*texerr);
                        D=(1/(1-exp(-C)))*(-COEFF2/((*temp)*(*temp)));
                        E=1/((*temp)+COEFF3);

                        /* for 12CO optical depth error                    */
                        err[z][0]=pow( ( (sigtex*D*D) + A ),0.5)*val[z][2];

                        /* for 12CO column density                         */
                        err[z][1]=pow( ( (sigtex*(C-B+E)*(C-B+E)) + A),0.5)*val[z][3];

                        err[z][2]=ABUNDH2*err[z][1];       /* for H2 column density */

                        err[z][3]=2*ABUNDHE*MH*err[z][2];     /* for surface density */

                        err[z][4]=AREA*err[z][3];          /* for mass */

                        err[z][5]=err[z][4]*MSUN_INV;      /* for mass (solar masses) */

                        err[z][6]=err[z][5]*(val[z][0]-VLSR)/cos(THETA);   /* for momentum */
                        if(err[z][6]<0.0)
                                {err[z][6]=-err[z][6];}

                        /* for kinetic energy                             */
                        err[z][7]=(val[z][0]-VLSR)*CONVERT*CONVERT*0.5*(val[z][0]-VLSR)
                                *err[z][4]*(1/(cos(THETA)*cos(THETA)));
                }
        }
} /* end sigma_thin */
```

```
void outof_sigma(double array1[][8], double array2[][8], int *count1, int *count2)
{
        int a,b,c,d;

        for(a=0;a<*count1;a++)
        {
                for(b=0;b<8;b++)
                {
                        sigred[a][b]=array1[a][b];
                }
        }

        for(c=0;c<*count2;c++)
        {
                for(d=0;d<8;d++)
                {
                        sigblue[c][d]=array2[c][d];
                }
        }

} /* end outof_sigma */
```

<<<<<<<<<<<<<<<<   PROCEDURE: output   >>>>>>>>>>>>>>>

```
void output()
{
        FILE *coord, *one, *two;
        float ra,dec,blank;
        int a,b,c,d,e,f,g,h,i,j,k,l,m,n,o,p,q,r,s,t,u,v,w,x,y;

        /* to input coordinates required for input files to ToSpecx    */
        coord=fopen("coord.dat","r");
        fscanf(coord,"%f %f",&ra,&dec);
        fclose(coord);

        /* to output data to individual files with errors, and ToSpecx files without errors    */

        /* for tau                                                    */
        one=fopen("tau.out","a"); /* for data file    */
        two=fopen("tau.dat","a"); /* for fits file    */
        fprintf(two,"%f %f\n",ra,dec);
        for(a=0;a<(redlim-1);a++)
                {fprintf(one,"%f %f\n", red[a][2], sigred[a][0]); fprintf(two,"%f\n", red[a][2]);}
        for(b=0;b<range;b++)
                {fprintf(one,"%f %f\n", centre[b][4], sigcentre[b][1]); fprintf(two,"%f\n", centre[b][4]);}
        for(c=0;c<(BINS-bluelim-2);c++)
                {fprintf(one,"%f %f\n", blue[c][2], sigblue[c][0]); fprintf(two,"%f\n", blue[c][2]);}
        fclose(one); fclose(two);

        /* for 12CO column density                                    */
        one=fopen("column12.out","a");    /* for data file    */
        two=fopen("column12.dat","a");    /* for fits file    */
        fprintf(two,"%f %f\n",ra,dec);
        for(d=0;d<(redlim-1);d++)
                {fprintf(one,"%e %e\n", (red[d][3]), (sigred[d][1]));
                fprintf(two,"%e\n", (red[d][3]/1.0E13));}
        for(e=0;e<range;e++)
                {fprintf(one,"%e %e\n", (centre[e][7]), (sigcentre[e][3]));
                fprintf(two,"%e\n", (centre[e][7]/1.0E13));}
        for(f=0;f<(BINS-bluelim-2);f++)
                {fprintf(one,"%e %e\n", (blue[f][3]), (sigblue[f][1]));
                fprintf(two,"%e\n", (blue[f][3]/1.0E13));}
        fclose(one); fclose(two);

        /* for H2 column density                                     */
        one=fopen("columnh2.out","a");    /* for data file    */
        for(g=0;g<(redlim-1);g++)
                {fprintf(one,"%e %e\n", (red[g][4]), (sigred[g][2]));}
        for(h=0;h<range;h++)
                {fprintf(one,"%e %e\n", (centre[h][8]), (sigcentre[h][4]));}
        for(i=0;i<(BINS-bluelim-2);i++)
                {fprintf(one,"%e %e\n", (blue[i][4]), (sigblue[i][2]));}
        fclose(one);
```

```c
one=fopen("sur.out","a"); /* for surface density data file    */
for(j=0;j<(redlim-1);j++)
        {fprintf(one,"%e %e\n", (red[j][5]), (sigred[j][3]));}
for(k=0;k<range;k++)
        {fprintf(one,"%e %e\n", (centre[k][9]), (sigcentre[k][5]));}
for(l=0;l<(BINS-bluelim-2);l++)
        f{printf(one,"%e %e\n", (blue[l][5]), (sigblue[l][3]));}
fclose(one);


one=fopen("mass.out","a");        /* for mass data file (in solar masses)     */
for(m=0;m<(redlim-1);m++)
        {fprintf(one,"%e %e\n", (red[m][7]), (sigred[m][5]));}
for(n=0;n<range;n++)
        {fprintf(one,"%e %e\n", (centre[n][11]), (sigcentre[n][7]));}
for(o=0;o<(BINS-bluelim-2);o++)
        {fprintf(one,"%e %e\n", (blue[o][7]), (sigblue[o][5]));}
fclose(one);


one=fopen("mom.out","a");        /* for momentum data file     */
for(p=0;p<(redlim-1);p++)
        {fprintf(one,"%e %e\n",(red[p][8]),(sigred[p][6]));}
for(q=0;q<range;q++)
        {fprintf(one,"%e %e\n", (centre[q][12]), (sigcentre[q][8]));}
for(r=0;r<(BINS-bluelim-2);r++)
        {fprintf(one,"%e %e\n", (blue[r][8]), (sigblue[r][6]));}
fclose(one);


one=fopen("kin.out","a"); /* for kinetic energy data file     */
for(s=0;s<(redlim-1);s++)
        {fprintf(one,"%e %e\n",(red[s][9]),(sigred[s][7]));}
for(t=0;t<range;t++)
        {fprintf(one,"%e %e\n", (centre[t][13]), (sigcentre[t][9]));}
for(u=0;u<(BINS-bluelim-2);u++)
        {fprintf(one,"%e %e\n", (blue[u][9]), (sigblue[u][7]));}
fclose(one);


/* for 12CO excitation temperature                      */
one=fopen("tex.out","a"); /* for data file    */
two=fopen("tex.dat","a"); /* for FITS file    */
fprintf(two,"%f %f\n",ra,dec);
blank=0.0;
for(v=0;v<(redlim-1);v++)
        {fprintf(one,"%f\n",blank); fprintf(two,"%f\n",blank);}
for(w=0;w<range;w++)
        {fprintf(one,"%f %f\n",centre[w][6],sigcentre[w][2]);
        fprintf(two,"%f\n",centre[w][6]);}
for(x=0;x<(BINS-bluelim-2);x++)
        {fprintf(one,"%f\n",blank); fprintf(two,"%f\n",blank);}
fclose(one); fclose(two);
} /* end output */
```

```
void total()
{
        FILE *first, *second, *third;
        int i,j,k,z,two,four,five,w,x,y,f,g,m;
        double int1,int2,int3,int4,int5,int6,int7,int8,int9;

        int1=0.0;int2=0.0;int3=0.0;int4=0.0;int5=0.0;int6=0.0;int7=0.0;int8=0.0;int9=0.0;

        /* to calculate the sums for the red wing    */
        two=(RL+1)-redlim;
        five=(CL+1)-redlim;
        if (redlim<CL)
        {
                for(i=upper12;i<redlim;i++)
                {
                        sumred[0][0] += red[i][7];sumred[1][0] += red[i][8];sumred[2][0] += red[i][9];
                        int1 += sigred[i][5]*sigred[i][5];
                        int2 += sigred[i][6]*sigred[i][6];
                        int3 += sigred[i][7]*sigred[i][7];
                }
                for(w=0;w<five;w++)
                {
                        sumred[0][0]+=centre[w][11];
                        sumred[1][0]+=centre[w][12];
                        sumred[2][0]+=centre[w][13];
                        int1+=sigcentre[w][7]*sigcentre[w][7];
                        int2+=sigcentre[w][8]*sigcentre[w][8];
                        int3+=sigcentre[w][9]*sigcentre[w][9];
                }
                for(x=five;x<two;x++)
                {
                        sumcen[0][0]+=centre[x][11];
                        sumcen[1][0]+=centre[x][12];
                        sumcen[2][0]+=centre[x][13];
                        int7+=sigcentre[x][7]*sigcentre[x][7];
                        int8+=sigcentre[x][8]*sigcentre[x][8];
                        int9+=sigcentre[x][9]*sigcentre[x][9];
                }
        }
```

```
if (redlim == CL)
{
        for(f=upper12;f<redlim;f++)
        {
                sumred[0][0] += red[f][7];sumred[1][0] += red[f][8];sumred[2][0] += red[f][9];
                int1 += sigred[f][5]*sigred[f][5];
                int2 += sigred[f][6]*sigred[f][6];
                int3 += sigred[f][7]*sigred[f][7];
        }
        sumred[0][0]+=centre[0][11];sumred[1][0]+=centre[0][12];sumred[2][0]+=centre[0][13];
        int1+=sigcentre[0][7]*sigcentre[0][7];
        int2+=sigcentre[0][8]*sigcentre[0][8];
        int3+=sigcentre[0][9]*sigcentre[0][9];
        for(g=1;g<two;g++)
        {
                sumcen[0][0]+=centre[g][11];
                sumcen[1][0]+=centre[g][12];
                sumcen[2][0]+=centre[g][13];
                int7+=sigcentre[g][7]*sigcentre[g][7];
                int8+=sigcentre[g][8]*sigcentre[g][8];
                int9+=sigcentre[g][9]*sigcentre[g][9];
        }
}
if(redlim>CL)
{
        for(m=upper12;m<(CL+1);m++)
        {
                sumred[0][0] += red[m][7];sumred[1][0] += red[m][8];sumred[2][0] += red[m][9];
                int1 += sigred[m][5]*sigred[m][5];
                int2 += sigred[m][6]*sigred[m][6];
                int3 += sigred[m][7]*sigred[m][7];
        }
        for(y=(CL+1);y<redlim;y++)
        {
                sumcen[0][0] += red[y][7]; sumcen[0][1] += red[y][8]; sumcen[0][2] += red[y][9];
                int7 += sigred[y][5]*sigred[y][5];
                int8 += sigred[y][6]*sigred[y][6];
                int9 += sigred[y][7]*sigred[y][7];
        }
        for(j=0;j<two;j++)
        {
                sumcen[0][0]+=centre[j][11];
                sumcen[1][0]+=centre[j][12];
                sumcen[2][0]+=centre[j][13];
                int7+=sigcentre[j][7]*sigcentre[j][7];
                int8+=sigcentre[j][8]*sigcentre[j][8];
                int9+=sigcentre[j][9]*sigcentre[j][9];
        }
}
```

```
sumred[0][1]=sqrt(int1); sumred[1][1]=sqrt(int2); sumred[2][1]=sqrt(int3);
sumcen[0][1]=sqrt(int7); sumcen[1][1]=sqrt(int8); sumcen[2][1]=sqrt(int9);
first=fopen("red_sum.dat","w");
fprintf(first,"%e  %e\n", sumred[0][0], sumred[0][1]);
fprintf(first,"%e  %e\n", sumred[1][0], sumred[1][1]);
fprintf(first,"%e  %e\n", (sumred[2][0]/1.0E38), (sumred[2][1]/1.0E38));
fclose(first);
third=fopen("cen_sum.dat","w");
fprintf(third,"%e  %e\n", sumcen[0][0], sumcen[0][1]);
fprintf(third,"%e  %e\n", sumcen[1][0], sumcen[1][1]);
fprintf(third,"%e  %e\n", (sumcen[2][0]/1.0E38), (sumcen[2][1]/1.0E38));
fclose(third);


/* to calculate the sums for the blue wing  */
four=(lower12+1)-(bluelim+1);
for(k=(BL-redlim);k<range;k++)
{
        sumblue[0][0]+=centre[k][11];sumblue[1][0]+=centre[k][12];sumblue[2][0]+=centre[k][13];
        int4+=sigcentre[k][7]*sigcentre[k][7];
        int5+=sigcentre[k][8]*sigcentre[k][8];
        int6+=sigcentre[k][9]*sigcentre[k][9];
}
for(z=0;z<four;z++)
{
        sumblue[0][0]+=blue[z][7];sumblue[1][0]+=blue[z][8];sumblue[2][0]+=blue[z][9];
        int4+=sigblue[z][5]*sigblue[z][5];
        int5+=sigblue[z][6]*sigblue[z][6];
        int6+=sigblue[z][7]*sigblue[z][7];
}
sumblue[0][1]=sqrt(int4); sumblue[1][1]=sqrt(int5); sumblue[2][1]=sqrt(int6);
second=fopen("blue_sum.dat","w");
fprintf(second,"%e       %e\n", sumblue[0][0], sumblue[0][1]);
fprintf(second,"%e       %e\n", sumblue[1][0], sumblue[1][1]);
fprintf(second,"%e       %e\n", (sumblue[2][0]/1.0E38), (sumblue[2][1]/1.0E38));
fclose(second);
} /* end total */
```

```
void intervals()
{
        FILE *tofile;
        int a,b,c,d,e,f,g,h,i,j,k,s,t,u,v,p,q,r,x,y,z,m,w,one,two,three,counter;
        double array[18][3],complete[FINAL][3];

        /* initializations                      */
        counter=0;
        for(x=0;x<18;x++)
                {for(y=0;y<3;y++) {array[x][y]=0.0;} }

        for(z=0;z<178;z++)
                {for(m=0;m<3;m++) {complete[z][m]=0.0;} }

        for(one=upper12;one<redlim;one++)
                {complete[one][0]=red[one][7];
                complete[one][1]=red[one][8];
                complete[one][2]=red[one][9];}

        for(two=0;two<range;two++)
                {complete[two+redlim][0]=centre[two][11];
                complete[two+redlim][1]=centre[two][12];
                complete[two+redlim][2]=centre[two][13];}

        counter=(lower12+1)-(bluelim+1);
        for(three=0;three<counter;three++)
                {complete[three+bluelim+1][0]=blue[three][7];
                complete[three+bluelim+1][1]=blue[three][8];
                complete[three+bluelim+1][2]=blue[three][9];}

        /* to calculate sums in intervals of 1 km/s */
        for(a=78;a<81;a++)      /*      -1 to 0 km s⁻¹            */
                {array[0][0]+=complete[a][0]; array[0][1]+=complete[a][1]; array[0][2]+=complete[a][2];}

        for(b=81;b<85;b++)      /*      -2 to -1 km s⁻¹           */
                {array[1][0]+=complete[b][0];array[1][1]+=complete[b][1];array[1][2]+=complete[b][2];}

        for(c=85;c<88;c++)      /*      -3 to -2 km s⁻¹           */
                {array[2][0]+=complete[c][0]; array[2][1]+=complete[c][1]; array[2][2]+=complete[c][2];}

        for(d=88;d<92;d++)      /*      -4 to -3 km s⁻¹           */
                {array[3][0]+=complete[d][0];array[3][1]+=complete[d][1];array[3][2]+=complete[d][2];}

        for(e=92;e<95;e++)      /*      -5 to -4 km s⁻¹           */
                {array[4][0]+=complete[e][0]; array[4][1]+=complete[e][1]; array[4][2]+=complete[e][2];}

        for(f=95;f<99;f++)      /*      -6 to -5 km s⁻¹           */
                {array[5][0]+=complete[f][0];array[5][1]+=complete[f][1];array[5][2]+=complete[f][2];}
```

```
for(g=99;g<102;g++)        /*      -7 to -6 km s⁻¹          */
        {array[6][0]+=complete[g][0];array[6][1]+=complete[g][1];array[6][2]+=complete[g][2];}

for(h=102;h<106;h++)       /*      -8 to -7 km s⁻¹          */
        {array[7][0]+=complete[h][0];array[7][1]+=complete[h][1];array[7][2]+=complete[h][2];}

for(i=106;i<109;i++)       /*      -9 to -8 km s⁻¹          */
        {array[8][0]+=complete[i][0]; array[8][1]+=complete[i][1]; array[8][2]+=complete[i][2];}

for(j=117;j<120;j++)       /*      -11 to -12 km s⁻¹        */
        {array[9][0]+=complete[j][0]; array[9][1]+=complete[j][1];array[9][2]+=complete[j][2];}

for(k=120;k<124;k++)       /*      -12 to -13 km s⁻¹        */
{
        array[10][0]+=complete[k][0];array[10][1]+=complete[k][1];array[10][2]+=complete[k][2];
}
for(s=124;s<127;s++)       /*      -13 to -14 km s⁻¹        */
{
        array[11][0]+=complete[s][0];array[11][1]+=complete[s][1];array[11][2]+=complete[s][2];
}
for(t=127;t<131;t++)       /*      -14 to -15 km s⁻¹        */
{
        array[12][0]+=complete[t][0]; array[12][1]+=complete[t][1]; array[12][2]+=complete[t][2];
}
for(u=131;u<134;u++)       /*      -15 to -16 km s⁻¹        */
{
        array[13][0]+=complete[u][0]; array[13][1]+=complete[u][1]; array[13][2]+=complete[u][2];
}
for(v=134;v<138;v++)       /*      -16 to -17 km s⁻¹        */
{
        array[14][0]+=complete[v][0]; array[14][1]+=complete[v][1]; array[14][2]+=complete[v][2];
}
for(p=138;p<141;p++)       /*      -17 to -18 km s⁻¹        */
{
        array[15][0]+=complete[p][0]; array[15][1]+=complete[p][1]; array[15][2]+=complete[p][2];
}
for(q=141;q<145;q++)       /*      -18 to -19 km s⁻¹        */
{
        array[16][0]+=complete[q][0]; array[16][1]+=complete[q][1]; array[16][2]+=complete[q][2];
}
for(r=145;r<148;r++)       /*      -19 to -20 km s⁻¹        */
{
        array[17][0]+=complete[r][0]; array[17][1]+=complete[r][1]; array[17][2]+=complete[r][2];
}

tofile=fopen("interval.dat","w");
for(w=0;w<18;w++)
        {fprintf(tofile,"%e     %e     %e\n", array[w][0], array[w][1], array[w][2]/(1.0E40));}
} /* end intervals */
```

APPENDIX E. LIST OF OBJECTS

Table 11. A Partial List of Astronomical Objects in NGC 7129. This list has been compiled from the references in the Bibliography.

Object	Other Names	Coordinates (1950)		Object Type
		α (21^h)	δ (65°)	
NGC 7129	DG 176, vdB 146, RK 112, Ber 40			reflection nebula
LkHα 234	V373 Cep, HRC 309, CSIRS 2, SVS 12	41^m 57.09^s	53′ 09.2″	Herbig Be star
BD +65 1638	SVS 8	41 49.11	52 24.6	B3 star
BD +65 1637	SVS 7	41 40.89	52 50.5	Herbig Be star
SVS 13		41 52.5	53 22	
optical jet from LkHα 234	HH 167			HH jet
RNO 138	GM 1-57, NS 20	41 48.49	50 35.5	reflection nebula
GGD 33a	HH 233a	41 54.46	57 27.6	T Tau star

GGD 33b	HH 233b	41^m 55.74^s	57' 22.1"	reflection nebula/outflow
GGD 35	HH 235	42 33.48	54 38.2	HH object
GGD 34	HH 234	42 20.76	54 50.3	outflow
HH 105		42 12.92	53 59.6	HH object
HH 103A		41 15.0	50 1	"
HH 103B		41 15.9	49 54	"
HH 103C		41 15.1	49 40	"
GGD 32A	HH 232A	41 17.9	50 42	"
GGD 32B	HH 232B	41 18.5	50 43	"
GGD 32C	HH 232C	41 18.7	50 48	"
GGD 32/1	HH 232/1	41 20.0	50 53	"
GGD 32/2A	HH 232/2A	41 20.5	50 41	"
GGD 32/2B	HH 232/2B	41 20.8	50 33	"
GGD 32/2C	HH 232/2C	41 19.9	50 36	"
GGD 32/3A	HH 232/3A	41 20.2	51 11	"
GGD 32/3B	HH 232/3B	41 20.5	51 6	"
GGD 32/4	HH 232/4	41 14.1	50 32	"
GGD 32/5	HH 232/5	41 25.8	50 55	"

GGD 32/6	HH 232/6	41^m 22.8^s	50′ 59″	HH object
GGD 32/7	HH 232/7	41 22.5	50 48	″
GGD 32/8	HH 232/8	41 22.5	50 43	″
HL 14		41 29.9	52 50	HH object/outflow
NGC 7129/HH 1		41 50.2	53 52	″
NGC 7129/HH 2		41 33.3	51 37	″
NGC 7129/HH 3		41 31.4	51 55	″
NGC 7129/HH 4		41 35.2	52 51	″
NGC 7129[1]	Bs40[3], C1, BFS 11A	41 57.22	53 08.85	H_2O maser
NGC 7129[2]	Bs40[1], BFS 11B	41 58.3	53 10	H_2O maser
NGC 7129[3]	Bs40[2], C2	41 52.28	53 01.39	H_2O maser
C3		41 57.37	53 08.24	H_2O maser
PS 1	3.6 cm radio source	41 57.383	53 08.15	deeply embedded companion of LkHα 234

APPENDIX F. SAMPLE WIP MACROS

The WIP macros for three of the figures in this thesis are presented here as an aid to those just beginning to learn the program. For the sake of brevity, the last two macros have been edited in order to minimize the number of times repeated commands are given. Moving the cursor around when the image scales are in right ascension and declination can be tricky. The first example macro, provided by Göeran Sandell, is a quick way of doing this with a minimum of frustration. If this macro is listed in the .wipmacros (or .wipinit) file, it is loaded every time WIP runs, and one does not have to worry about doing it oneself. The second example is that of drawing a spectrum, as well as multiple spectra, on a single figure. In the third example, two greyscale images and the contours of a third image are overlapped. Drawing lines when your image scales are in right ascension and declination is also demonstrated. The last example illustrates the use of error bars, and includes multiple spectra on a page but on separate axes.

Example 1: The Macro radec in the .wipinit or .wipmacros file

```
define radec                                    # creates macro radec in define mode
set \10 $3 + ($2 * 60.0) + ($1 * 3600.0)        # sets \10 equal to the RA given
set \11 abs($6) + (abs($5) * 60.0) + (abs($4) * 3600.0)   # sets \11 equal to the DEC given
if $4 < 0 set \11 -\11                          # if the hour < 0, \11=-\11
if $5 < 0 set \11 -\11                          # if the minute < 0, \11=-\11
move \10 \11                                    # move the cursor to (\10, \11)
end                                             # ends define mode
```

Example 2: Figure 16 (page 36)

```
vsize 1.0 4.0 1.0 7.0                    # set location and size of image on screen/paper
lwidth 1                                 # set line width
lstyle 1                                 # set line style
font 1                                   # set font
expand 1.0                               # set character size
#
limits -20 10 -25 30                     # set limits of x and y scales
ticksize 0 4 10 5                        # set tickmarks
box bctsn bctsnv                         # draw box, with tickmarks
xlabel V\dLSR\u [km s\u-1\d]             # label x-axis
ylabel T\dA\u\u*\d [K]                   # label y-axis
color 1                                  # set color
move -10 -25                             # move cursor to (-10, -25)
draw -10 30                              # draw line (y-axis) to position (-10, 30)
#
data lk_co32_9052                        # opens data file for 12CO J = 3 → 2 spectrum
xcol 3                                   # reads x data from 3rd column
ycol 4                                   # reads y data from 4th column
lwidth 2                                 # sets new line width
bin 1                                    # draws histogram
lwidth 1
move -20 0
draw 10 0                                # draws x-axis
#
data 13co_9052                           # opens data file for 13CO J = 3 → 2 spectrum
xcol 3
ycol 4
limits -20 10 -45 10                     # sets new scale limits (shifts spectrum up)
lwidth 2
bin 1
lwidth 1
move -20 0
draw 10 0                                # draws new x-axis
#
data lk_co21_9052                        # opens data file for 12CO J = 2 → 1 spectrum
xcol 3
ycol 4
limits -20 10 -5 50                      # sets new scale limits (shifts spectrum down)
lwidth 2
bin 1
lwidth 1
move -20 0
draw 10 0                                # draws new x-axis
#
limits -20 10 -25 30                     # resets scale limits to original limits
expand 0.8                               # sets new character size
lwidth 1
move 8 26                                # moves cursor to (8, 26)
putlabel 1.0 \u13\dCO J = 3 \(2261) 2    # draws label centred on cursor position
```

Example 3: Figure 17 (page 38)

```
vsize 1.5 6.5 5.0 9.0                          # set location and size of image on screen/paper
#
image ngc7129.fit                              # read in image ngc7129.fit
winadj 0 700 0 500                             # set aspect ratio (700 x 500 pixels)
header rd                                       # load fits header
#
# now to define and save x and y scales for entire image
#
set \1 38.0 + (60.0 * 42.0) + (3600.0 * 21.0)   # NOTE: RA must be in seconds of arc
set \2 4.00 + (60.0 * 41.0) + (3600.0 * 21.0)
set \4 0.06 + (60.0 * 55.0) + (3600.0 * 65.0)   # NOTE: DEC must be in arcseconds
set \3 11.07 + (60.0 * 48.0) + (3600.0 * 65.0)
#
limits \1 \2 \3 \4                              # set scale limits
lstyle 1                                        # set line style
expand 0.8                                      # set character size
box bcinstz bcinstvyz                           # draw box, with tickmarks
xlabel \ga (1950)                               # label x-axis
mtext L 3.5 0.5 0.5 \gd (1950)                   # label y-axis
#
halftone 60 200                                 # draw greyscale image of ngc7129.fit
#
image lkha234.fit                              # read in image lkha234.fit
winadj 0 700 0 500
header rd
limits \1 \2 \3 \4                              # reset scale limits
#
halftone 40 200                                 # draw greyscale image of lkha234.fit
#
image firs_blue.fit                            # read in image of blue lobe of the FIRS
header rd
limits \1 \2 \3 \4                              # reset scale limits
lstyle 1
lwidth 4                                        # set new line width
color 1                                         # set color
levels 1.0 2.0 3.0 4.0 5.0                       # set contour levels
contour t                                        # draw contours
#
# to mark position of FIRS
#
color 0                                         # set new color
expand 1.6                                      # set new character size
radec 21 41 53.86 +65 49 33                      # execute macro using specified RA and DEC
symbol 18                                        # set symbol style
dot                                             # draw symbol at cursor position
#
```

```
color 1
expand 1.2
radec 21 41 53.86 +65 49 33
symbol 18
dot
expand 0.8                                    # set new character size
move 78108.828125, 236963.671875             # move cursor to given coordinates (RA, DEC)
putlabel 0.001 FIRS                          # draw label FIRS, left-justified on cursor position
#
# to draw infrared jet axes (from Cabrit et al. (1990))
#
set \7 6.26 + (41.0 * 60.0) + (21.0 * 3600.0)    # set \7 to RA of one end of axis
set \8 19.8 + (48.0 * 60.0) + (65.0 * 3600.0)    # set \8 to corresponding DEC
#
color 1
lstyle 2                                      # set new line style
lwidth 2
radec 21 42 15.0 +65 55 00                    # execute macro using specified RA and DEC
draw \7 \8                                    # draw line to other end of axis
```

Example 4: Figure 43 (page 93)

```
vsize 1.5 9.0 2.0 6.3                         # set location and size of image on screen/paper
color 1                                       # set color
font 1                                        # set font
expand 1.0                                    # set character size
lwidth 1                                      # set line width
lstyle 1                                      # set line style
limits -15 0 -2 10                            # set scale limits
ticksize 0 4 0 4                              # set ticksize
#
# the lower left graph
#
panel 2 3 1                                   # sets current panel
box bctsn bctsnv                              # draw box, with tickmarks
mtext B 2.0 0.5 0.5 V\dLSR\u [km s\u-1\d]     # label x-axis
ylabel \gt\u12\d                              # label y-axis
move -15 0                                    # move cursor to (-15, 0)
draw 0 0                                      # draw line to (0, 0)
lwidth 2                                      # set new line width
data tau_7560                                 # open data file
xcol 1                                        # reads x data from 1rd column
ycol 2                                        # reads y data from 2th column
ecol 3                                        # reads size of error bar from 3rd column
bin 1                                         # draw histogram
lwidth 1
expand 2.5                                    # sets new character size
errorbar 2                                    # draw errorbar in +y direction
errorbar 4                                    # draw errorbar in -y direction
```

```
#
expand 0.5                                    # set new character size
move -3.9 5.0                                 # move cursor position
arrow -4.9 4.0 45 0.0                         # draw arrow from -4.9 to -4.0 at 45°
move -12.4 6.0
arrow -11.4 5.0 45 0.0
move -2 8
label (e)                                     # writes string at current cursor position
expand 1.0
#
# the lower right graph
#
panel 2 3 2                                   # sets current panel
box bctsn bctsnv
mtext B 2.0 0.5 0.5 V\dLSR\u [km s\u-1\d]      # label x-axis
move -15 0
draw 0 0                                       # draw new x-axis
lwidth 2
data tau_m2323
xcol 1
ycol 2
ecol 3
bin 1
lwidth 1
expand 2.5
errorbar 2
errorbar 4
expand 1.0
#
# the middle left graph
#
panel 2 3 3                          .         # set current panel
box bctsn bctsnv
ylabel \gt\u12\d                               # label y-axis
move -15 0
draw 0 0                                       # draw new x-axis
lwidth 2
data tau_9838
xcol 1
ycol 2
ecol 3
bin 1
lwidth 1
expand 2.5
errorbar 2
errorbar 4
expand 1.0
#
# the middle right graph
#
panel 2 3 4                                   # sets current panel
box bctsn bctsnv
```

```
move -15 0
draw 0 0                          # draws new x-axis
lwidth 2
data tau_00
xcol 1
ycol 2
ecol 3
bin 1
lwidth 1
expand 2.5
errorbar 2
errorbar 4
expand 1.0
#
# the upper left graph
#
panel 2 3 5                       # sets current panel
box bctsn bctsnv
ylabel \gt\u12\d                  # label y-axis
move -15 0
draw 0 0                          # draw new x-axis
lwidth 2
data tau_6030
xcol 1
ycol 2
ecol 3
bin 1
lwidth 1
expand 2.5
errorbar 2
errorbar 4
expand 1.0
#
# the upper right graph
#
panel 2 3 6                       # sets current panel
box bctsn bctsnv
move -15 0
draw 0 0
lwidth 2
data tau_3045
xcol 1
ycol 2
ecol 3
bin 1
lwidth 1
expand 2.5
errorbar 2
errorbar 4
```

Curriculum Vitae

Beverly Miskolczi
May, 1998

Address:

Department of Astronomy and Physics
Saint Mary's University
Halifax, NS
B3H 3C3

Personal:

Date of Birth: January 16, 1971
Place of Birth: Ottawa, ON
Citizenship: Canadian

Education:

M. Sc. 1998   Saint Mary's University
                Astronomy
                Advisor: Dr. George Mitchell

B. Sc. 1994   Carleton University
                Physics, Honours
                Advisor: Dr. Dan Kessler

Awards:

1989   Canada Scholar

1990   Canada Scholar

1994   J. D. DeBlois Scholarship, Saint Mary's University

1995   Saint Mary's Graduate Student Scholarship

Professional Development:

1992-94	teaching assistant for introductory astrophysics course; duties included marking, conducting tutorial sessions and labs, and observatory duties Carleton University
1994-97	teaching assistant for first year physics course; duties included marking and conducting tutorial sessions lectures introductory astronomy classes on an incidental basis Saint Mary's University
1995	co-discoverer, along with D. Lane and P. Grey, of SN1995f
1995	observing run at the James Clerk Maxwell Telescope
1995	visiting researcher, Joint Astronomy Centre, Hilo, Hawai'i

Publications:

"A Multitransition CO Study of the NGC 7129 Cloud Core", B. Miskolczi, G. Mitchell, G. Sandell, and H. Matthews 1996, BAAS, 28, 1414.

"The Distribution and Kinematics of Gas in the Star-Forming Core of NGC 7129", G. Mitchell, B. Miskolczi, G. Sandell, and H. Matthews, 1998, in preparation.

"General Index to the Journal of the Royal Astronomical Society of Canada, 1967-1996", B. Miskolczi, D. Turner, 1998, in preparation.
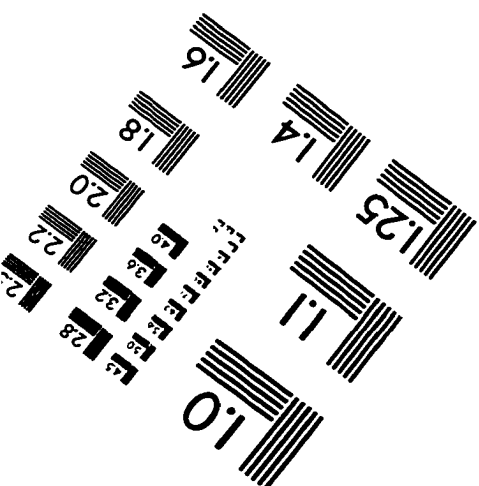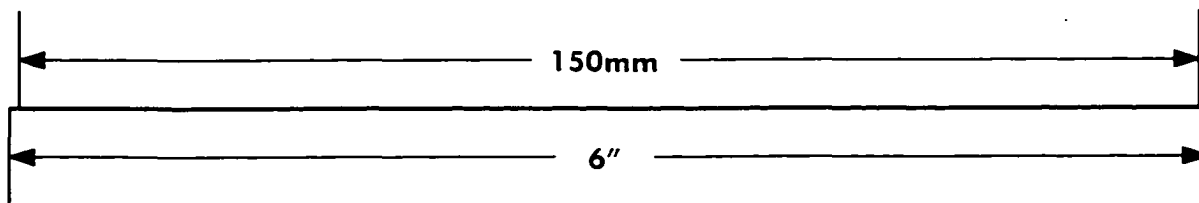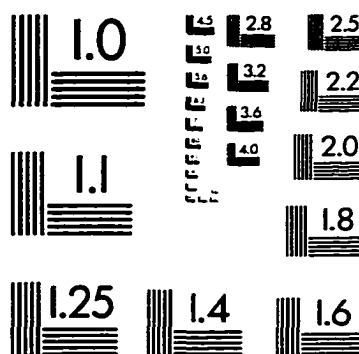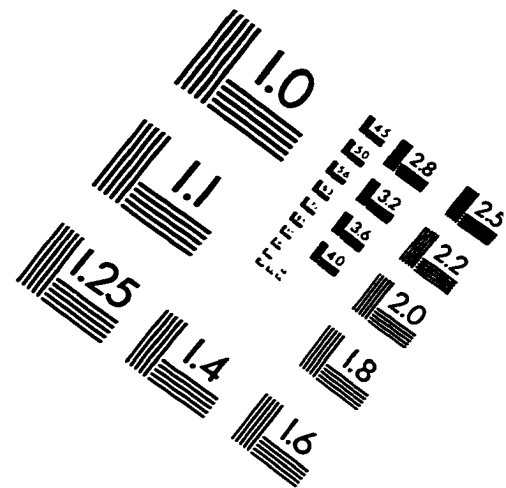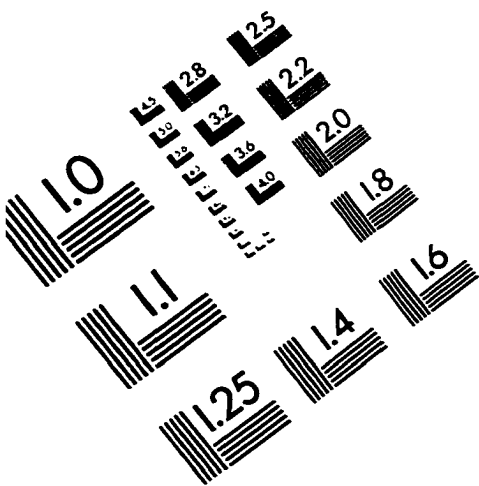
Professional References:

Dr. George Mitchell
Saint Mary's University
Halifax, NS
B3H 3C3
gmitchell@ap.stmarys.ca

Dr. Malcolm Butler
Saint Mary's University
Halifax, NS
B3H 3C3
mbutler@ap.stmarys.ca

Dr. Gary Welch
Saint Mary's University
Halifax, NS
B3H 3C3
gwelch@ap.stmarys.ca

IMAGE EVALUATION
TEST TARGET (QA-3)

150mm

6"